

Snow dynamics in the Himalaya

Sneeuwdynamieken in de Himalaya

(met een samenvatting in het Nederlands)

P R O E F S C H R I F T

ter verkrijging van de graad van doctor aan de Universiteit Utrecht
op gezag van de rector magnificus, prof.dr. H.R.B.M. Kummeling,
ingevolge het besluit van het college voor promoties in het openbaar te verdedigen
op maandag 13 maart 2023 des middags te 2.15 uur

door

Emmy Elise Stigter

geboren op 25 augustus 1993 te Vlaardingse

Promotoren:

Prof. dr. W.W. Immerzeel

Prof. dr. ir. M.F.P. Bierkens

Beoordelingscommissie:

Prof. dr. M.R. van den Broeke

Prof. dr. J.D. Lundquist

Prof. dr. L.M. Tallaksen

Dr. F. Pellicciotti

Dr. R. Mott

Snow dynamics in the Himalaya

Promotoren:

Prof. dr. W.W. Immerzeel

Prof. dr. ir. M.F.P. Bierkens

Examination committee:

Prof. dr. M.R. van den Broeke, *Utrecht University*

Prof. dr. J.D. Lundquist, *University of Washington*

Prof. dr. L.M. Tallaksen, *University of Oslo*

Dr. F. Pellicciotti, *Swiss Federal Institute for Forest, Snow and Landscape Research*

Dr. R. Mott, *Swiss Federal Institute for Forest, Snow and Landscape Research*

ISBN 978-90-6266-641-6

Published by Faculty of Geosciences, Utrecht University, The Netherlands, in:
Utrecht Studies in Earth Sciences (USES), ISSN 2211-4335

Typeset using Xe_{La}T_EX

Cover: Picture of the peak Gangchempo in the Langtang catchment © Inka Koch

Cover layout assistance: Margot Stoete

Printed by Ipskamp Drukkers B.V., Enschede, The Netherlands

Correspondence to: Emmy E. Stigter, e.e.stigter@uu.nl

This work is licensed under the Creative Commons Attribution-NonCommercial-ShareAlike 4.0 International Licence, <https://creativecommons.org/licenses/by-nc-sa/4.0/>.

© 2023 by Emmy E. Stigter.

Chapters 2 to 4 and Appendix A are based on final author versions of published articles,

© by Emmy E. Stigter and co-authors. More information and citation suggestions are provided at the beginning of these chapters.

Utrecht Studies in Earth Sciences 271

Snow dynamics in the Himalaya

Emmy Elise Stigter

Utrecht 2023

Faculty of Geosciences, Utrecht University

Loneliness

No sky at all;
no earth at all – and still
the snowflakes fall

Hashin

Contents

List of Figures	xi
List of Tables	xv
1 Introduction	5
1.1 Snow dynamics in alpine catchments	5
1.2 Monitoring and modelling snow dynamics in alpine catchments	6
1.3 Snow research in the Himalaya	9
1.4 Research questions and thesis outline	15
2 Assimilation of snow cover and snow depth into a snow model to estimate snow water equivalent and snowmelt runoff in a Himalayan catchment	17
2.1 Introduction	18
2.2 Methods and data	19
2.3 Results and discussion	27
2.4 Conclusions	38
2.5 Acknowledgements	38
3 The importance of snow sublimation on a Himalayan glacier	39
3.1 Introduction	40
3.2 Study area	41
3.3 Data and methods	42
3.4 Results	47
3.5 Discussion	53
3.6 Conclusions	57
3.7 Acknowledgements	58
4 Energy and mass balance dynamics of the seasonal snowpack at two high-altitude sites in the Himalaya	59
4.1 Introduction	60
4.2 Study area	61
4.3 Data and methodology	61
4.4 Results	66
4.5 Discussion	73
4.6 Conclusions	78
4.7 Acknowledgements	79

5 Synthesis	81
5.1 Main results in this thesis	81
5.2 Future research and recommendations	82
Appendix A WRF	85
References	89
Acknowledgements	101
List of publications	103
Teaching and supervision	105
About the author	107

List of Figures

2.1	Study area with the locations of the in situ observations. Langtang and Langshisha refer to the two main glaciers in the upper Langtang valley.	19
2.2	Comparison of maximum temperature (T_{max}) and cumulative monthly precipitation (P) for the study period (January 2013–September 2014) and the 1988–2009 time series (based on measurements in Kyangjin). The average yearly cumulative precipitation is 853 and 663 mm for the study period and the 1988–2009 time series respectively.	27
2.3	Observed surface temperature with 10-min interval at two locations (Table 2.1). The blue vertical lines indicate the start and end of the snow cover.	28
2.4	Modelled 8-day maximum snow extent before and after calibration (ensemble mean); Landsat 8 snow extent and MOD10A2 snow extent per elevation zone. The RMSE (km^2) is given per zone for the fit between modelled (before and after calibration) and MOD10A2 snow extent.	31
2.5	Observed snow depth and modelled snow depth (i) before calibration, (ii) after calibration of snow extent (SE), and (iii) after calibration of both snow extent and snow depth (SD+SE; ensemble mean) at three locations. The RMSE (mm) is given for the fit between modelled (before and after calibration) and observed snow depth.	33
2.6	Spatial distribution of ensemble mean annual average snow water equivalent (SWE).	34
2.7	Boxplots of SWE per elevation zone averaged over the simulation period and all ensemble members for the study period (reference) and the four climate sensitivity tests (Table 2.3).	34
2.8	Change in SWE averaged over the simulation period and all members for each climate sensitivity test (Table 2.3).	35
2.9	Modelled runoff at catchment outlet for the study period (January 2013–September 2014) and change in runoff compared to the study period for the climate sensitivity tests.	36
3.1	Study area, including the outline of Yala glacier (light blue), elevation contour lines (dark blue) and the locations of the three micro-met stations (MM), AWS Yala Glacier and AWS Yala Base Camp (stars). The inset shows the location of Yala Glacier in the central Himalaya, Nepal.	42
3.2	Pictures of (A) AWS Yala Base Camp, (B) micro-met station Yala Ridge, and (C) AWS Yala Glacier, including eddy covariance system (Photos: W. Immerzeel).	43
3.3	Time series of observed turbulent fluxes and radiation components at AWS Yala Glacier. The turbulent fluxes are positive for fluxes pointing from the atmosphere to the snow surface and negative for fluxes pointing from the surface to the atmosphere.	48

3.4	Observed and simulated sublimation rate (black), wind speed (blue), and actual vapour pressure (red) at AWS Yala Glacier for 21 October and 12 November 2016 with relatively low ($<1.0 \text{ mm day}^{-1}$) and high sublimation rates ($>1.0 \text{ mm day}^{-1}$). EC refers to the eddy covariance measurements. Bulk, PM and KG refer to the simulated sublimation with the bulk-aerodynamic method, Penman-Monteith equation and Kuchment and Gelfan (1996) empirical relation, respectively.	49
3.5	Monthly values of air temperature, relative humidity and wind speed observed at AWS Yala Glacier for the 2016–2017 winter season. The bars indicate the monthly cumulative sublimation simulated with the bulk-aerodynamic for 15 October 2016–20 April 2017.	49
3.6	Scatter plots of meteorological variables against sublimation rate, observed at AWS Yala Glacier. The colour of the data points refers to the observed wind speed.	50
3.7	Scatter plots of observed and simulated sublimation for different parameterizations. R, NSE, BIAS, and RMSE refer to the correlation coefficient, Nash-Sutcliffe efficiency, bias and root mean square error, respectively.	52
3.8	Sublimation residuals (observed-modelled) for the bulk-aerodynamic method against observed wind speed, vapour pressure deficit, air temperature and time of day.	53
3.9	Daily cumulative sublimation, simulated with the bulk-aerodynamic method, and daily average WRF fields of (10 m) wind speed, (2 m) actual vapour pressure and surface temperature for a humid day (1 January 2017) and a non-humid day (12 November 2016) at Yala Glacier. The black lines represent the elevation contour lines.	54
4.1	Panel A gives an overview of the location of the Langtang Valley and the locations of the two sites (Yala and Ganja La). The white outlines indicate the extent of the glaciers located within the valley. Panel B shows the measurement set-up of the vertical snow temperature profile at Yala (Section 3.2). Panels C and D show the automatic weather stations with the CS725 SWE sensors and the surrounding terrain at Ganja La and Yala, respectively.	62
4.2	Time series of the observed SWE from the CS725 SWE sensor at both Ganja La and Yala from January 2017 until June 2019. Note that the snow accumulation in January 2019 is not captured at Ganja La due to station failure. At Yala, SWE observations are only available from October 2017 until April 2019. Note that observed SWE at Yala exceeds the maximum reliable measurement range of 600 mm in April 2019. The inset shows the evolution of SWE in more detail for the 2018 snow season.	67
4.3	Monthly averaged observed wind speed, air temperature, surface temperature and relative humidity at both Yala and Ganja La from February to May 2018 when sufficient snow is present ($\text{SWE} > 15 \text{ mm}$). Snow is not sufficiently present to show the monthly averaged variables at Ganja La in February. The blue horizontal line indicates the zero-degrees line.	68

4.4	Hourly energy balance, including the net shortwave (S_{net}) and net long wave (L_{net}) radiation, latent heat flux (LE) and the sensible heat flux (H). S_{net} and L_{net} are observed values and LE and H are calculated using the bulk-aerodynamic method. The net energy (E_{net}) is the sum of S_{net} , L_{net} , LE and H . Fluxes pointing towards the surface are assumed positive whereas fluxes pointed towards the atmosphere are negative. In addition, the figure illustrates the partitioning of E_{net} over the changes in cold content (ΔCC) of the snowpack (note that a positive ΔCC reduces the CC), melt or refreezing (<i>refr</i>). The partitioning of the net energy is based on Exp. 4 (explained in detail in Section 4.3.5). If $E_{net} > 0 \text{ W m}^{-2}$, then E_{net} is partitioned over melt and decrease of the cold content, whereas E_{net} is partitioned over refreezing and increase of the cold content if $E_{net} < 0 \text{ W m}^{-2}$. The monthly averaged values of all energy balance components is given in the text of each panel. Snow is not sufficiently present to show the monthly averaged variables at Ganja La in February.	69
4.5	Adjusted Budyko curves for Yala and Ganja La for the time period February–May 2018 when sufficient snow is present (SWE > 15 mm). The blue shaded area indicates the liquid water limit, whereas the red shaded area indicates the energy limit. The refreezing and melt estimates were aggregated to weekly values. The markers are coloured to the according week number of the year. The potential refreezing is based on the results of Exp. 3, whereas the actual refreezing is based on the results of Exp. 4. Weeks without melt are excluded (weeks 6–8, 10 and 11 for Yala).	71
4.6	Hourly vertical temperature profiles of the snowpack measured with the TidbiTs at Yala, averaged over three different time periods.	73
4.7	The development of the observed cold content of the snowpack throughout the snow season 2018 at Yala.	73
4.8	Pictures of three snow pits at Ganja La on April 30 th 2018 and Yala on April 25 th 2018. The snow pits at Ganja La have a depth of 41–42 cm and contain four or five ice layers. The snow pits at Yala have a depth of 38–44 cm and contain five ice layers.	77
A.1	Validation of wind speed, specific humidity and surface temperature simulated by WRF (dashed lines) with observations from three meteorological stations positioned on the glacier (solid lines) for a humid (1 January 2017) and non-humid day (12 November 2016). Each colour refers to observations/simulations at one of the locations of the on-glacier meteorological stations.	87

List of Tables

2.1	Definition of measurement periods and seasons in this study	21
2.2	Parameters in the snow model. Initial value indicates the uncalibrated parameter value and the value range indicates the range which is used for the sensitivity analysis. Sensitivity of snow depth (<i>SD</i>) and snow extent (<i>SE</i>) represents the difference between the 90 th and 10 th percentile of mean snow depth and snow extent resulting from the sensitivity analysis.	22
2.3	Changes in temperature (ΔT) and precipitation (ΔP) for the climate sensitivity tests (same as Immerzeel et al. (2013)).	27
2.4	Confusion matrices for comparison of Landsat 8 snow maps and MOD10A2 snow maps with in situ snow observations.	29
2.5	Confusion matrices for comparison of in situ snow observations provided by snow depth and surface temperature observations with remotely sensed snow maps (MOD10A2 and Landsat 8 combined).	29
2.6	Parameter value range prior to calibration and after calibration. The standard deviation of posterior parameter values is based on the standard deviation of all members.	30
2.7	Classification accuracy of modelled snow extent based on pixel comparison with Landsat 8 snow maps. Calibrated accuracies are averaged over all members and the standard deviation represents the standard deviation in individual member accuracies (after calibration).	32
3.1	Description of the meteorological stations.	43
3.2	Results of the various linear regressions and multiple linear regressions through the meteorological data and sublimation rate observed at AWS Yala Glacier (on-glacier) and AWS Yala Base Camp (off-glacier).	51
4.1	Description and specifications of the sensors at the locations Ganja La and Yala.	63
4.2	Results of the different snowpack energy and mass balance experiments at Yala and Ganja La for the 2018 winter season. The experiment numbers refer to the experiments described in Section 3.5. Please note that a positive Δ cold content reduces the cold content of the snowpack. The mass balance is defined as the sum of melt, refreezing, evaporation, sublimation and deposition in which negative values indicate mass losses and positive values indicate mass gains. The evaporation, sublimation and deposition are given in Table 4.4 since these values are constant across the experiments. The results of Exp. 4 are also given for the snow seasons 2017 and 2019 at Ganja La. However, note that the snow accumulation in January 2019 is not captured due to station failure.	70

4.3	Estimated melt and refreezing based on Exp. 4 with differing albedo at Ganja La and Yala for the 2018 snow season. 'Station' refers to the observed albedo at the AWSs, whereas 'Albedo 0.9', 'Albedo 0.7' and 'Albedo 0.5' refer to an assumed seasonal constant albedo of 0.9, 0.7 and 0.5, respectively.	71
4.4	Seasonal evaporation, sublimation, deposition as calculated with the bulk-aerodynamic method for the 2018 winter season at the locations Ganja La and Yala. The seasonal cumulative increase and decrease of SWE are based on the CS725 SWE observations. Values are also given for the snow seasons 2017 and 2019 at Ganja La. However, note that the snow processes are not captured in January 2019 due to station failure.	72
A.1	Overview of WRF configuration.	86

Summary

The word Himalaya stems from Sanskrit, and literally translates as the abode of snow. This is illustrative of the importance of snow in this mountain range. The Himalaya is the highest mountain range on earth. Large areas are seasonally or even permanently covered in snow. The Himalaya is often referred to as the water tower of Asia, mostly because large amounts of fresh water are stored in snow and glacier ice. These frozen water towers act as a seasonal storage of water and provide a reliable and steady supply of meltwater to millions of people who live downstream in particular during droughts. In the last decade, glacier research in the Himalaya has really taken off and a plethora of studies has been published quantifying mass balances and glacier hydrological processes using direct observations, remote sensing or modelling. However, Himalaya snow research did not evolve as quickly and was mainly constrained to remote sensing studies focusing on snow cover trends. Since the snow covered area in the Himalaya is considerably larger than the glacier area, it is safe to assume that snowmelt plays a key role in the Himalayan water cycle, possibly, even more important than glacier melt. There is therefore a very large knowledge gap in data driven snow studies in the region that focus on critical processes in the energy and mass balance of the snowpack in the Himalaya. In this thesis, I contribute to closing this knowledge gap by using a combination of unique snow observations high in the Himalaya, remote sensing and modelling to study a number of those key processes. In particular, I focus on quantifying the snow water equivalent, the cold content, sublimation and refreezing of meltwater in the snowpack.

In chapter 2, I combine in situ snow depth observations, remotely sensed snow cover and a snow model to estimate the spatial patterns of snow water equivalent and snowmelt runoff in the Langtang catchment in Nepal. An ensemble Kalman filter is successfully used to assimilate the in situ and remotely sensed snow observations into a snow model to obtain optimal parameter values. A novel component is the use of in situ snow depth observations for assimilation and independent validation because it allows to validate the snow quantity rather than snow cover alone. The model results show a strong gradient in the snow water equivalent with elevation. At high altitude the spatial distribution of the snow water equivalent is largely determined by the spatial distribution of precipitation. Climate sensitivity tests, in which temperature and precipitation are perturbed, reveal that at high altitude an increase in melt due to temperature increase can be offset by an increase in precipitation. Both outcomes emphasize the importance of accurate prediction of the changes in spatial distribution of precipitation in future. Furthermore, the climate sensitivity tests show that snowmelt runoff increases in December-May, but decreases in June-September as a result of earlier melt onset because of increased air temperature.

In chapter 3, I quantify snow sublimation on a Himalayan glacier using eddy covariance measurements at an altitude of 5350 m a.s.l. A one-month timeseries reveal that daily sublimation values reach approximately 1 mm on average in October/November due to favourable meteorological conditions. I also model sublimation at the same site and I validate the model with the field observations. The bulk-aerodynamic method proves to be most suited for sim-

ulating snow sublimation. Simulations driven by in situ meteorological observations show that for the entire winter cumulative sublimation is 125 mm at the location of the station. Together with 9 mm of evaporation, this implies that 21% of the annual snowfall is directly returned to the atmosphere in form of water vapor. Spatially distributed simulations of sublimation and evaporation for a non-humid day reveal increased sublimation rates for increased wind speed. Close to the ridge the sublimation is 1.7 times higher than the station location as high wind speed prevails at the ridge. This shows that sublimation may return even more than 21% of the annual snowfall to the atmosphere.

In chapter 4, I assess the importance of refreezing of snow meltwater and snowpack cold content dynamics in the energy and mass balance of the snowpack at two high-altitude sites. An experimental setup based on local meteorological observations, surface energy balance observations and mass balance observations shows that 32 and 34% of the meltwater refreezes again at the two locations. At one of the locations observed snow temperature profiles were used to quantify the cold content dynamics of the snowpack. 21% of the positive net energy is used to overcome the nightly increase in cold content and to reach the 0 °C isothermal state to initiate snowmelt during the day. This even increases to up to 50% for all months with the exception of May for both sites.

This thesis shows the critical role that sublimation, refreezing of snow meltwater and snowpack cold content dynamics play in the energy and mass balance of the snowpack at high altitude. Future snow and hydrological studies should include these essential processes. So far, the vast majority of models applied in the region use the air temperature as a proxy for melt. However, in my thesis I showed that the reality is much more complex and that using the air temperature does not capture those processes which control the energy and mass balance of the snowpack. Future hydrological model studies in the Himalaya should attempt to simulate the full energy balance and mass balance, despite the fact that a lot of data is required. By setting up a number of well instrumented snow observatories, combined with smart downscaling of reanalysis data and high-resolution remote sensing, most of these data challenges can be overcome. Admittedly it is a large investment, but it is the only way forward to improve the hydrological forecasts and projections in this complex environment.

Samenvatting

Het woord 'Himalaya' komt uit het Sanskrit en vertaalt zich letterlijk als 'de verblijfplaats van sneeuw'. Dit illustreert hoe belangrijk sneeuw is in deze gebergteketen. De Himalaya is de hoogste gebergteketen ter wereld. Grote gebieden worden bedekt met seizoensgebonden of zelfs eeuwige sneeuw. Er wordt vaak gerefereerd naar de Himalaya als de watertoren van Azië, voornamelijk omdat grote hoeveelheden zoet water liggen opgeslagen in sneeuw en gletsjerijs. Deze bevroren watertorens dienen als een tijdelijke wateropslag en bieden, vooral gedurende droogte, een betrouwbare en stabiele toevoer van smeltwater voor miljoenen mensen die benedenstrooms wonen. Het laatste decennium kenmerkte zich door een enorme groei aan gletsjerstudies waarin de massabalans en hydrologische gletsjerprocessen werden gekwantificeerd met behulp van metingen, satellietbeelden of rekenmodellen. Echter, het sneeuwonderzoek in de Himalaya ontwikkelde zich minder snel en beperkte zich voornamelijk tot het onderzoeken van trends in de sneeuwbedekking op basis van satellietbeelden. Hierdoor is in de regio een groot tekort ontstaan aan studies die gebaseerd zijn op waarnemingen en die zich focussen op de belangrijke processen van de energie- en massabalans van het sneeuwpakket in de Himalaya. Het met sneeuw bedekte oppervlakte is aanzienlijk groter dan het gletsjeroppervlakte. Het is daarom aannemelijk dat sneeuwsmelt een belangrijke rol heeft in de watercyclus van de Himalaya en mogelijk zelfs belangrijker is dan gletsjersmelt. In deze thesis bestudeer ik een aantal van deze belangrijke processen en draag ik bij aan het verkleinen van het kennishiaat door gebruik te maken van unieke veldwaarnemingen van sneeuweigenschappen in de Himalaya, evenals satellietbeelden en rekenmodellen. Ik focus in het bijzonder op het kwantificeren van de hoeveelheid water die in het sneeuwpakket is opgeslagen, de koudeopslag van het sneeuwpakket, sublimatie en het opnieuw bevriezen van smeltwater in het sneeuwpakket.

In hoofdstuk 2 combineer ik lokale sneeuwobservaties met rekenmodellen en satellietbeelden, om de ruimtelijke patronen van de sneeuwwaterequivalent en sneeuwsmeltafvoer in het Langtang stroomgebied in Nepal te bepalen. Een ensemble Kalman filter wordt succesvol toegepast om veldwaarnemingen en waarnemingen gebaseerd op satellietbeelden, in een sneeuwmodel te assimileren, om zo optimale parameterwaarden te verkrijgen. Het gebruik van lokale sneeuwdieptewaarnemingen voor assimilatie en onafhankelijke validatie is nieuw, omdat het de mogelijkheid geeft om de hoeveelheid sneeuw te valideren in plaats van alleen de sneeuwbedekking. De resultaten van het rekenmodel laten zien dat er een sterke relatie bestaat tussen de sneeuwwaterequivalent en de hoogte. Op grote hoogte wordt de ruimtelijke verdeling van de sneeuwwaterequivalent grotendeels bepaald door de ruimtelijke verdeling in neerslag. Klimaatgevoeligheidsstests, waarin de luchttemperatuur en neerslag worden verstoord, laten zien dat op grote hoogte een toename van smelt als gevolg van een toename van de temperatuur, kan worden gecompenseerd door een toename in de neerslag. Beide resultaten benadrukken het belang van accurate verwachtingen van de veranderingen in de ruimtelijke verdeling van neerslag in de toekomst. Verder laten de klimaatgevoeligheidsstests zien dat de sneeuwsmeltafvoer toeneemt in december tot en met mei. Echter, dit neemt af in juni tot en met september door een eerdere start van sneeuwsmelt als gevolg van een

hogere luchttemperatuur.

In hoofdstuk 3 kwantificeer ik de sneeuwsublimatie op een gletsjer in de Himalaya met behulp van eddy covariantie metingen op een hoogte van 5350 meter boven zeeniveau. Een tijdserie van één maand in oktober/november laat zien dat de dagelijkse sublimatie gemiddeld ongeveer 1 mm bedraagt door gunstige meteorologische condities. Ik modelleer op dezelfde locatie ook de sublimatie en ik valideer het model met veldwaarnemingen. De 'bulk-aerodynamic' methode bewijst zich als de beste methode om sneeuwsublimatie te modelleren. Simulaties, gevoed met lokale meteorologische waarnemingen, laten zien dat voor de gehele winter de cumulatieve sublimatie op de locatie van het meetstation 125 mm bedraagt. Samen met 9 mm verdamping, impliceert dit dat 21% van de jaarlijkse sneeuwval terugkeert naar de atmosfeer in vorm van waterdamp. Ruimtelijke simulaties van sublimatie en verdamping voor een niet-vochtige dag laten een toename van sublimatie zien door een toename van de windsnelheid. Dichtbij de graad is de sublimatie 1.7 keer hoger dan op de locatie van het meetstation, omdat hoge windsnelheden prevaleren op de graad. Dit laat zien dat sublimatie mogelijk zelfs nog meer dan 21% van de jaarlijkse sneeuwval kan zijn.

In hoofdstuk 4 bestudeer ik het belang van het opnieuw bevriezen van smeltwater en de koudeopslag voor de energie- en massabalans van het sneeuwpakket op twee locaties op grote hoogte. Een experimentele benadering, gebaseerd op lokale meteorologische waarnemingen, energiebalans waarnemingen en massabalans waarnemingen, laten zien dat 32 en 34% van het smeltwater opnieuw bevriest op de twee locaties. Op één van de locaties wordt de koudeopslag gekwantificeerd met behulp van veldwaarnemingen van sneeuwtemperatuurprofielen. 21% van de positieve netto energie wordt gebruikt om de nachtelijke toename in koudeopslag te overwinnen en om de isotherme staat van 0 °C te bereiken zodat de sneeuws-melt kan starten. Met uitzondering van mei, neemt dit zelfs toe tot waarden van 50% voor beide locaties.

Deze thesis laat de belangrijke rol zien van sublimatie, het opnieuw bevriezen van smeltwater en de koudeopslag van het sneeuwpakket voor de energie- en massabalans in de Himalaya. Toekomstige sneeuw- en hydrologische studies zouden deze essentiële processen moeten toevoegen. Tot dusver gebruikt het overgrote deel van de toegepaste rekenmodellen de luchttemperatuur als benadering voor sneeuwsmelt. Echter, in mijn thesis laat ik zien dat de realiteit veel complexer is en dat de gebruikte luchttemperatuur niet alle processen vastlegt die de massa- en energiebalans van het sneeuwpakket bepalen. Toekomstige hydrologische modelleerstudies in de Himalaya zouden moeten pogen om de volle energie- en massabalans te simuleren, ondanks het feit dat dit om veel data vraagt. De meeste uitdagingen op het gebied van data kunnen worden overwonnen door een aantal goede referentie locaties met uitgebreide sneeuwobservaties op te zetten gecombineerd met het neerschalen van meteorologische model uitvoer en hoge resolutie satellietbeelden. Dit vereist een grote investering, maar dit is de enige weg vooruit om hydrologische verwachtingen en projecties te verbeteren in deze complexe omgeving.

Chapter 1

Introduction

1.1 Snow dynamics in alpine catchments

Snow is an important component of the hydrological cycle in mountainous regions as it represents a seasonal or sometimes permanent storage of water. The timing of melt onset and magnitude of snowmelt runoff is important for domestic water use, hydropower and flood and drought forecasting. In addition, snow in mountain regions exerts a large influence on the local climate as snow is an almost perfect reflector of incoming shortwave radiation, reflecting up to 90% of the incoming solar radiation. Besides that, snow also acts as an insulator, insulating the ground or glacier ice below the snowpack from atmospheric variability and influences. Ecosystems are also largely affected by the presence of snow and its duration.

The properties of a snowpack typically have a high variability in space and time in mountainous areas due to various snow processes. The general complex topography in alpine catchments enhances the spatiotemporal variability. This makes it challenging to study and understand the local snowpack in mountainous terrain. The snowpack can be described with the snow energy balance and snow mass balance, which are coupled, and explained below.

The energy available for melt or warming of the snowpack depends on its energy balance. The energy balance of a snowpack (at a non-vegetated site) consists of the radiative fluxes, turbulent fluxes, ground heat flux (G) and advection of heat by precipitation (H_{prec}). The radiative fluxes are composed of the net shortwave (S_{net}) and longwave radiation (L_{net}). The turbulent fluxes are formed by the sensible and latent heat flux (H and LE , respectively). The change in internal energy state or energy available for melt is then given by Equation 1.1 (all in W m^{-2}):

$$E_{net} = S_{net} + L_{net} + H + LE + G + H_{prec} \quad (1.1)$$

Fluxes pointing towards the surface are assumed positive whereas fluxes pointed towards the atmosphere are negative. The net radiative flux is the difference between the incoming and outgoing shortwave and longwave fluxes. The outgoing shortwave radiation is determined by the incoming shortwave radiation and the albedo of the snow cover. A large part of the incoming shortwave radiation is directly reflected back into the atmosphere as a snow surface typically has a high albedo. The albedo of a snow surface can vary between 0.9 for fresh snow and 0.5 for dirty, old, ripened snow (Brock et al., 2000). The albedo typically varies in space and time. The incoming longwave radiation depends, among others, on the atmospheric temperature, cloud cover and humidity (e.g. Kok et al., 2019). The outgoing longwave radiation can be approximated using the Stefan-Boltzmann law and the snow surface temperature. However, this is a simplification as the emissivity of snow varies with wavelength. The turbulent fluxes are driven by wind and near-surface gradients in temperature and humidity for the sensible and latent heat flux, respectively. The ground heat flux is determined by the ground temperature underlying the snowpack. Stronger temperature gradients result in higher fluxes. The ground heat flux is often higher at the start of the snow season when there

still is a large difference between the snowpack temperature and ground temperature.

The snowpack mass balance is determined by precipitation in the form of snowfall (*snow*) or in the form of rainfall (*rain*) in case of rain-on-snow events, melt, refreezing of meltwater (*refr*), sublimation (*subl*), evaporation (*evap*), deposition (*dep*), condensation (*cond*) and redistribution of snow by wind and avalanches (*red*), and is given by Equation 1.2 (all in mm):

$$\Delta mass = melt + refr + subl + evap + dep + cond + precip + red \quad (1.2)$$

The mass balance is coupled to the energy balance via melt, refreezing, sublimation, evaporation, deposition and condensation. Melt, refreezing and warming of the snowpack are determined by the net energy resulting from the energy balance, whereas sublimation, evaporation, deposition and condensation follow from the latent heat flux.

Globally there is a large disparity in the breadth of scientific snow studies. This is largely dependent on the mountain range. For example, numerous detailed, yet region-wide, studies have been performed in the Alps (e.g. Griessinger et al., 2019; Matiu et al., 2021), in Norway (e.g. Saloranta, 2012; Saloranta, 2016) and in the western US (e.g. Serreze et al., 1999; Sun et al., 2019), because monitoring networks exist and the scientific infrastructure is in place. The abundance of snow observations in these mountain ranges help to understand the local snowpack dynamics and support modelling efforts. However, there are still alpine regions that have remained (relatively) unexplored and understudied, in particular the Andes and High Mountain Asia. The snow energy and mass balance in these ranges have only been marginally studied.

1.2 Monitoring and modelling snow dynamics in alpine catchments

1.2.1 In situ snow observations

This section provides a concise description of the variety of in situ snow measurements that can be performed and which can be relevant from a hydrological point of view. The first and most detailed way of measuring a snowpack is via a snow pit and measuring the properties of all individual snow layers. Properties that are commonly measured are: the snow density, snow depth, snow water equivalent, grain size, grain type and snow temperature. However, this method is labor-intensive and provides an observation at a single moment at a specific point location. Similarly, a snow core can be taken. Even though this requires no snow pit, this is still a point observation in time and space. Therefore, automated measurements are more often used to (continuously) measure the properties of a snowpack.

Snowfall

The formation of a snowpack starts with snowfall. Three types of snowfall measurements can be distinguished to automatically measure snowfall: heated tipping bucket, rain gauge and ground-based radar. For a heated tipping bucket snowfall falls into a funnel, where the snow melts as the tipping bucket is heated. The meltwater drains into a small bucket with known volume. Once the small bucket is filled with the meltwater, it tips over. The tips are recorded and provide information about the amount of snowfall and the snowfall rate. The other way to measure snowfall is with a rain gauge. For these measurements the precipitation, which falls in a bucket, is weighed. Both methods have in common that for snowfall undercatch occurs when wind speed is significant and needs to be corrected for. Also, both methods cannot distinguish between rain and snow and, therefore, additional measurements are required. For example, a disdrometer can be used to measure the phase of precipitation. Other options to approximate the phase partitioning is by additionally measuring air temperature or snow

depth. Radar measurements of precipitation rely on the scattering of microwave energy when the emitted beam encounters precipitation. The scattered energy is being measured, which provides information about the precipitation type and intensity. However, a disadvantage of radar measurements is the high power consumption.

Snow water equivalent

From a hydrological point of view, the snow water equivalent is the most important property of a snowpack as it is the amount of water that results from a snowpack when it melts completely. This can be measured automatically in multiple ways. The snow water equivalent can be measured using a snow pillow (e.g. Sorteberg et al., 2001). A snow pillow is installed in the season when no snow is present. During the snow season the snow pillow is covered by snow and its mass is weighed via a difference in exerted pressure on the pillow by the snow. The disadvantage of a snow pillow is the requirement of a concrete base, which is not feasible in remote places. Also, the formation of ice layers, may reduce the accuracy of the measurements due to the snow supporting capability of these layers. Another way of measuring the snow water equivalent is the usage of a radiation sensor. Two types are available, yet the principle is the same for both types. The presence of a snowpack attenuates the emitted gamma-ray radiation or cosmic rays, either emitted from the surface or space, respectively. By measuring this attenuation, the snow water equivalent is measured. A gamma-ray sensor that measures the attenuation of gamma-ray emitted from the surface is installed above the (snow) surface pointing toward the surface. In contrast, a cosmic ray sensor that measures the attenuation of cosmic rays emitted from space, is installed at the surface pointing toward the sky and is buried by snow during the snow season. The disadvantage of a gamma-ray sensor is that it only accurately measures snow water equivalent for relatively little accumulation. In study areas with significant accumulation (>600 mm w.e.) this method cannot be applied. More novel methodologies exist, but are less well studied. For example Kinar and Pomeroy (2015) describe an acoustic method to measure snow properties. Another example is the study of Koch et al. (2019) in which low-cost gps sensors are used to measure snow water equivalent, as well as liquid water content and snow depth.

Snow depth

Even though snow depth does not give direct information about the snow water equivalent, it is a measure of the quantity of snow. The snow depth can be automatically measured using either a sonic distance sensor or an electronic laser distance sensor. Both devices measure the distance between the sensor and the snow surface. The difference lies within the type of signal that is sent to the snow surface and which is received again. A disadvantage of a sonic distance sensor can be that it requires measurements of the air temperature in order to correct the distance measurement for variations of the speed of sound in air.

Wind-induced snow transport

Snow transport can be automatically measured based on an acoustic (Doorschot et al., 2004; Lehning and Fierz, 2008; Cierco et al., 2007), an optic (Doorschot et al., 2004) or an impact-pulse-counting technique (Bintanja et al., 2001). These systems give information about the occurrence, frequency and intensity of wind-induced snow transport. The acoustic technique relies on the principle that snow particles which hit the measurement device, creates sound. This sound is being measured. The impact-pulse technique measures the momentum of the snow particles hitting the measurement device (Bintanja et al., 2001). For the optic technique a laser sends out a light signal which is received by a sensor. Snow particles pass through the

laser beam causing a signal which can be translated in particle size and the number of particles (Doorschot et al., 2004).

1.2.2 Satellite remote sensing of snow

Satellite remote sensing provides a valuable source of information about the snowpack in alpine catchments. It gives information without having to access the study area. Below, I describe the use of satellite imagery for obtaining information about the local snowpack. Satellite remote sensing can be divided into two classes of methods based on wavelength: optical remote sensing and microwave remote sensing.

For optical remote sensing the natural reflected radiation is measured of wavelengths ranging from visible to near-infrared, up to thermal infrared. Every surface type has a different reflecting behavior through the optical spectrum. The distinctive spectral properties of snow are the basis for snow mapping based on optical satellite remote sensing. Snow strongly reflects visible light, whereas snow strongly absorbs shortwave infrared. The presence of snow is generally determined with the normalised difference snow index (NDSI), which is a ratio of green and shortwave infrared (Dozier, 1989). Multiple operating satellite sensors exist that can be used for snow mapping, e.g. Landsat sensors (e.g. Dozier, 1989; Gascoïn et al., 2019; Crawford et al., 2013), Sentinel-2 (e.g. Gascoïn et al., 2019), Advanced Very High Resolution Radiometer (AVHRR) (e.g. Hüsler et al., 2012; Simpson et al., 1998) and Moderate Resolution Imaging Spectroradiometer (MODIS) (e.g. Hall et al., 2002; Hall and Riggs, 2007). Though, MODIS snow maps are most widely used as these snow maps are readily available and offer a decent spatiotemporal resolution. Namely, these snow maps have a daily temporal resolution and 500 m spatial resolution. Besides information on snow cover, the albedo of the snow surface can also be approximated by optical remote sensing, providing valuable information about how much solar radiation is reflected by the snow surface. The disadvantage of optical remote sensing is its sensitivity to clouds. Cloud cover prohibits retrieval of snow cover based on optical satellite imagery, which can be problematic in regions with persistent cloud cover.

In microwave remote sensing, electromagnetic radiation is measured of wavelengths in the order of 1 mm to 1 m. Microwave remote sensing can be divided into active and passive microwave remote sensing systems. The difference between these two is that active systems use their own source of electromagnetic energy, whereas passive systems measure naturally emitted microwave radiation by the surface. As the emitted microwave radiation by the land surface is low, a large pixel size is required to receive sufficient radiation in order to meet the sensor sensitivity for passive microwave systems. The pixel size is usually in the order of 25 km. For active microwave remote sensing the pixel size is much smaller, usually in the order of tens of meters. In contrast to optical remote sensing, microwave remote sensing is insensitive for clouds and is also not dependent on daylight which is an advantage. Passive microwave remote sensing has been used to detect (changes in) snow water equivalent (Smith et al., 2017; Smith and Bookhagen, 2018). However, due to the coarse pixel size the application of this in alpine catchments is questionable where spatial variability in snow conditions is generally very high. Besides snow water equivalent, various properties of the snowpack can be measured using microwave remote sensing. Marin et al. (2020) describes that three phases of snowpack melt can be sensed, i.e. melt onset, ripening, and melt runoff. Also, snow depths have been estimated using microwave remote sensing (e.g. Lievens et al., 2019; Lievens et al., 2022).

1.2.3 Snow modelling

Modelling of a snowpack can be performed with snow models of varying complexity. The complexity of a snow model depends on whether the snowpack is simulated as a single homogeneous layer or as a multi-layer snowpack. Also, the number of included snow processes determines the snow model complexity. Finally, the approach can be either empirical or physically-based. The simpler snow models assume that only snowfall and snowmelt occurs and simulate the snowpack as a single homogeneous snow layer. In contrast, more complex snow models take into account all snow processes as described in Equations 1.1 and 1.2. The difference between the most complicated models and more simple models is also the way in which melt is modelled. Melt is in hydrological studies commonly related to air temperature only (Hock, 2003) or in combination with incoming shortwave radiation (Pellicciotti et al., 2005). In more complex snow models the full energy balance (Equation 1.1) is considered to estimate how much energy is available for melt. Multiple studies have investigated the influence of varying process representation in modelling and the models capability of representing the actual snowpack. Examples of detailed physical-based snow models are: SNOWPACK (Bartelt and Lehning, 2002), ALPINE3D (Lehning et al., 2006), CROCUS (Brun et al., 1989; Brun et al., 1992), SNOBAL (Marks et al., 1999), SnowModel (Liston and Elder, 2006) and COSIPY (Sauter et al., 2020). Simpler models are often used in alpine catchments when the meteorological input data is not available for a more detailed model. Multiple studies have been performed to study whether an increase in complexity yields better results when compared to observations (e.g. Avanzi et al., 2016; Förster et al., 2014; Warscher et al., 2013; Wever et al., 2014; Günther et al., 2019). Also, snow model intercomparison projects, such as SnowMIP and ESM-SnowMIP have provided valuable insights regarding model complexity and performance (e.g. Etchevers et al., 2004; Krinner et al., 2018).

1.3 Snow research in the Himalaya

1.3.1 Himalayan climate

Four seasons can be distinguished in the Himalaya: the monsoon (June-September), the post-monsoon (October-November), the winter (December-February) and the pre-monsoon (March-May). During the monsoon warm moist air from the Indian Ocean moves north to the Himalaya where the extreme topography forms a barrier and forces orographic uplift. This causes cooling of the warm moist air and consequently the formation of clouds resulting in significant almost daily precipitation in the months from June to September. Immerzeel et al. (2014) showed that 68-89% of the annual precipitation falls during monsoon in the Langtang catchment in the central Himalaya. Most precipitation falls on the southern flanks of the Himalaya and dies out towards the north. Also, the influence of the monsoon decreases from east to west in the Himalaya. For example, Azam et al. (2014) showed that the monsoon contributed only 21% to the annual precipitation in the western Himalaya. The vertical distribution of precipitation is season-dependent (Collier and Immerzeel, 2015). Results of Collier and Immerzeel (2015) show peak precipitation above 5000 m a.s.l. during the winter, whereas the precipitation maximum lies at approximately 3000 m a.s.l. during the monsoon for the Langtang catchment in Nepal. During monsoon the air temperature is relatively high and the diurnal cycle in temperature is small compared to the other seasons (Shea et al., 2015b). The wind regime can be characterized by a diurnal cycle with weak nighttime wind and strong daytime up-valley wind (Potter et al., 2018; Ohata et al., 1981). This wind regime is evident for all seasons (Ohata et al., 1981). However, more exposed sites at higher altitude are prone to the influence of synoptic scale winds (Shea et al., 2015b).

In contrast to the monsoon, winters are generally rather dry. Atmospheric humidity is very low and typically only few, but substantial snowfall events form the seasonal snowpack at high elevation (Shea et al., 2015b; Immerzeel et al., 2014). Winter precipitation events follow from westerly disturbances where moist air is brought in from the west. The influence of westerlies decrease from west to east. In winter clear-sky conditions prevail, leading to high incoming solar radiation. This drives large diurnal cycles in both temperature and atmospheric vapor pressure. Both variables show a peak in the afternoon (Shea et al., 2015b). Also, wind speeds are particularly high during winter (Shea et al., 2015b).

Post-monsoon and pre-monsoon are the seasons with a transition from a monsoon-dominated climate to a westerlies-dominated climate and the other way around, respectively. The post-monsoon season is identified by a sharp drop in temperature after the monsoon. Very dry conditions prevail and rarely any precipitation falls (Collier and Immerzeel, 2015; Immerzeel et al., 2014). During the pre-monsoon the precipitation frequency increases again towards the monsoon. In both post-monsoon and pre-monsoon periods the highest precipitation intensities are observed (Shea et al., 2015b).

1.3.2 Snow observations

In situ observations

Only few snow observations are available in the Himalaya (Pritchard et al., 2020; Rohrer et al., 2013). Also, the time series are generally short. Putkonen (2004) used five cosmic-ray sensors, that recorded the attenuation of cosmic radiation from space, in order to measure daily snow water equivalent for the winters 1999-2000 and 2000-2001. The stations were located in the Annapurna range in the central Himalaya at elevations ranging between 3133 and 4400 m a.s.l. The snow water equivalent increases with increasing altitude. In March the variation in snow water equivalent is largest between the different stations, as at low elevation the melt season started, whereas at the highest station snow still accumulated until May (Putkonen, 2004). The maximum snow water equivalent had a similar magnitude at the highest station for both winters (~1000 mm). This accumulation is significantly higher compared to the maximum snow water equivalent (~200 mm) measured at 4962 m a.s.l. for the winters 2016-2017 and 2017-2018 in the study of Kirkham et al. (2019). This study observed snow water equivalent in the Langtang catchment in the central Himalaya. Kirkham et al. (2019) used data from a gamma-ray sensor that measured the attenuation of gamma-ray radiation emitted by the ground. Veldhuijsen et al. (2022) used the same station to validate a snow model and show that accumulation for the 2018-2019 winter is more than twice the accumulation for the 2017-2018 winter. This demonstrates the high interannual variability in snow water equivalent. All three studies show that at higher elevation the snow season lasts for approximately 6 months (Kirkham et al., 2019; Putkonen, 2004; Veldhuijsen et al., 2022).

Recently, multiple AWSs have been placed at high altitude by the Rolex National Geographic Perpetual Planet expedition to Mount Everest. Three AWSs located at an elevation of 3810, 5315 and 6464 m a.s.l. record the snow depth (Matthews et al., 2020). However, a detailed study on the accumulation and ablation based on this data has not yet been performed. Both Azam et al. (2014) and Litt et al. (2019) used surface height change data as well to estimate snow accumulation and ablation of the snowpack and glacier ice, to complement their studies on the surface energy balance and temperature indexed melt models for on-glacier sites. Azam et al. (2014) showed substantial snowfall events of up to 80 mm water equivalent (w.e.) at the station location at 4670 m a.s.l in the western Himalaya. Though, the mean daily snowfall was much lower: 5.3, 6.3 and 1.4 mm w.e. for the post-monsoon, the winter and the monsoon, respectively. Litt et al. (2019) show accumulation of snow at two sites on Mera glacier in the central Himalaya. At the higher site (6432 m a.s.l.) accumulation of snow

of up to two meters was observed, whereas this is less than 1 m at the lower site (5380 m a.s.l.). Note, however, that these values cannot be directly compared to the values reported by Putkonen (2004), Kirkham et al. (2019) and Veldhuijsen et al. (2022), as those values are in w.e. Nevertheless, assuming a snow density of 300 kg m^{-3} , the accumulation at Mera glacier at high altitude is significantly higher compared to the values of Kirkham et al. (2019) and Veldhuijsen et al. (2022). This can be explained by the fact that this site is located in the accumulation zone of Mera glacier, where snow accumulates in summer during the monsoon when more precipitation falls compared to winter (Litt et al., 2019; Wagnon et al., 2013).

Annual accumulation rates have also been studied at multi-decadal timescales using an ice core from East Rongbuk Col on Mount Everest (Kaspari et al., 2008). This ice core spans from AD 1534 to 2001. Annual accumulation rates have varied between 0.3 and 0.8 m ice equivalent, which is likely linked to intensification/reduction of monsoonal influence (Kaspari et al., 2008; Kaspari et al., 2007). Wagnon et al. (2013) drilled snow cores and measured ablation stakes to estimate snow accumulation and glacier-wide mass balance on Mera and Pokalde glaciers, located in the central Himalaya. Their study shows that accumulation of snow occurs during the monsoon, whereas wind-induced snow transport (and likely sublimation) causes near-zero mass balance during the winter.

Remote sensing

Snow remote sensing studies in the Himalaya have been performed based on optical remote sensing and microwave remote sensing. Remote sensing studies are more common for this region than studies based on in situ observations as it does not require access to the study site. This is advantageous in the desolate landscape of the Himalaya with steep and inaccessible terrain. Optical remote sensing has been used to determine the snow cover extent in the Himalaya (e.g. Girona-Mata et al., 2019; Gurung et al., 2017; Immerzeel et al., 2009; Maskey et al., 2011; Mishra et al., 2014). Past studies show that the snow cover extent has a large seasonality in the Himalaya. Generally there is extensive snow cover during winter and early spring, and only snow cover at the highest altitudes during monsoon (e.g. Mishra et al., 2014). Only at very high altitude perennial snow is present. The snow cover has typically a decreasing trend from west to east, which can be observed in all seasons (Immerzeel et al., 2009). Besides the decreasing trend, the snow cover is largely dependent on altitude because of the according air temperature gradient (Gurung et al., 2017). The spatial variability of snow cover is high within a catchment, which cannot be explained by altitude solely. Girona-Mata et al. (2019) and Veldhuijsen et al. (2022) show that aspect is decisive too for the spatial distribution of snow cover, as it determines the incoming solar radiation that contributes to the energy available for melt. Trends in snow cover extent were studied by Maskey et al. (2011). Snow extent was shown to decrease in winter at elevations below 6000 m a.s.l. over an 8-year period (2000-2008). Contrastingly, snow extent increased in March and Autumn at elevations above 5000 m a.s.l. and 4000 m a.s.l., respectively (Maskey et al., 2011). Similarly, Mishra et al. (2014) showed an increase in snow extent in Autumn at elevations higher than 4700 m a.s.l. for a catchment in the Central Himalaya. This is based on a study period from 2000 to 2010. Remotely sensed snow cover has frequently been combined with a distributed hydrological/snow model in order to estimate snowmelt runoff and/or snow water equivalent (e.g. Saloranta et al., 2019; Bookhagen and Burbank, 2010; Wulf et al., 2016). Studies that have combined a remote sensing product and a hydrological/snow model are described in Section 1.3.3.

Besides snow cover extent, snowmelt has been detected using both active and passive microwave remote sensing. The advantage of microwave remote sensing is the insensitivity for clouds. Cloud cover obstructs snow studies based on optical remote sensing during the

monsoon when cloud cover is extensive and persistent. Panday et al. (2011) show regional differences in snowmelt season in the Himalaya based on active microwave remote sensing. The duration of the snowmelt season (averaged over 2000-2008) is longest in the eastern Himalaya and shortest in the western Himalaya. This is explained by an earlier melt onset in the eastern Himalaya compared to the western Himalaya, as a consequence of stronger solar forcing at lower latitude in the eastern part. Spatial variability in the duration of the snowmelt season can be linked to elevation and aspect (Panday et al., 2011). A preliminary study by Xiong et al. (2017) also shows a correlation of the melt onset date with elevation. The melt onset date is relatively late for the higher peaks in the Himalaya. A trend analysis of the melt onset date and melt period was performed over three decades by Smith et al. (2017) based on passive microwave data. In general, the trend in melt onset date is negative in the Himalaya for the time period 1987-2016, meaning that the snow melt starts earlier in the season over time (Smith et al., 2017). However, the length of the melt season is shortening, caused by an earlier end of the snow season. For shorter time periods, it appears that the trends of snowmelt end date are sometimes positive and thus are not uniform in time. The exact causes have remained unexplained as the length of the data set is relatively short (Smith et al., 2017).

Passive microwave remote sensing was also used to estimate trends in snow water equivalent (Smith and Bookhagen, 2018; Smith and Bookhagen, 2020). Smith and Bookhagen (2018) and Smith and Bookhagen (2020) show a variable annual trend in snow water equivalent for the time period 1987-2016 per elevation band in the Himalaya. At higher elevation annual snow water equivalent trends have been detected to be positive, whereas at the forefront of the Himalaya an alternating pattern of positive and negative trends exist (Smith and Bookhagen, 2020). This is likely related to micro climates resulting from the extreme topography. The trends in the seasonal snow water equivalent are less uniform in space compared to the annual trends. Though, it should be mentioned that passive microwave snow water equivalent products are uncertain, especially in complex terrain such as the Himalaya (e.g. Xiong et al., 2017). The spatial resolution (25x25 km) is generally relatively coarse compared to the scale that snow dynamics occur in steep topography. Also, no absolute value for the snow water equivalent can be derived.

Apart from snow water equivalent, snow depth is also a variable indicating the accumulation of snow. Lievens et al. (2019) used active microwave remote sensing (Sentinel-1) to study snow depth with a spatial resolution of 1 km² for all mountain ranges in the Northern Hemisphere for two consecutive winters. Even though the high spatial resolution allows detailed analysis of the snow depth, validation of the results are largely lacking in the Himalaya. The snow depth retrievals were validated at only 6 sites in the Himalaya (Lievens et al., 2019). The majority of the described remote sensing studies have in common that the results are not, or only limited, validated with in situ observations of the local snowpack in the Himalaya, leading to large uncertainties in their estimates.

Snow remote sensing studies in the Himalaya mainly investigated the presence of snow cover, which gives no information on either the mass or energy balance of the snowpack. More recently, trends in snow water equivalent were studied, but only relative changes can be studied using this remote sensing method, not absolute changes (Smith and Bookhagen, 2020). A single preliminary study, based on active microwave remote sensing, demonstrates that melt can be detected (but not quantified) (Xiong et al., 2017). Based on this, it can be concluded that snow remote sensing studies in the Himalaya have given us only limited understanding of snow processes.

1.3.3 Snow modelling

Multiple studies have focused on the contribution of snowmelt runoff to total runoff (e.g. Bookhagen and Burbank, 2010; Armstrong et al., 2019; Wulf et al., 2016; Singh and Jain, 2003; Jeelani et al., 2012). The contribution of snowmelt to total runoff varies from west to east in the Himalaya (Bookhagen and Burbank, 2010; Armstrong et al., 2019). Bookhagen and Burbank (2010) estimated the contribution of snowmelt to the seasonal and annual discharge for the entire Himalaya. They estimated that the annual contribution of snowmelt to total discharge is 50% in the western part of the Himalaya, 25% in the eastern part, and 20% in the central part of the Himalaya. Seasonal contributions are higher in spring and during early monsoon, because at this time of the year rainfall has a minor contribution to discharge (Bookhagen and Burbank, 2010). The spatial distribution of snowmelt runoff contribution can be explained by variations in snow accumulation. Bookhagen and Burbank (2010) provide three factors that control the snow accumulation and therefore snowmelt runoff. The first factor is the catchment hypsometry. When a larger part of the catchment is located at a higher elevation, more snow accumulates because of lower air temperature. Due to a lower air temperature, more precipitation will fall as snow instead of rain and also snowmelt reduces. The second factor is precipitation magnitude. Due to the complex topography in the Himalaya the spatial distribution of precipitation is highly variable. For example, orographic uplift causes more precipitation to fall at higher elevation. The third factor is the seasonality of precipitation. More winter precipitation generally leads to more snow accumulation, because precipitation will fall as snow due to low air temperature. In contrast, more precipitation during monsoon only leads to snow accumulation at the highest peaks.

The estimations of snowmelt contribution to total runoff actually varies significantly among studies. For the western part of the Himalaya the estimated contributions of annual snowmelt runoff to total runoff varies between 35 and 68% (Wulf et al., 2016; Singh and Jain, 2003; Armstrong et al., 2019; Bookhagen and Burbank, 2010; Jeelani et al., 2012). This varies between 20 and 43% for the central Himalaya (Bookhagen and Burbank, 2010; Brown et al., 2014; Armstrong et al., 2019; Ragetti et al., 2015). This can be explained in several ways, namely: i) varying model structure/complexity, ii) varying input data, iii) the definition of snowmelt (i.e. melt of on-glacier snowpacks are in some studies defined as snowmelt, whereas in other studies this is defined as glacier melt), iv) distance from source (i.e. the relative contribution of meltwater decreases more downstream as the rainwater contribution is increasing), v) varying study periods and interannual variability. This complicates direct comparisons between studies.

In the future, the snowpack in the Himalaya will keep being affected by climate change (Jeelani et al., 2012; Immerzeel et al., 2012; Singh and Bengtsson, 2004). The projected increase in temperature will decrease the accumulation of the snowpack in two ways. Firstly, the fraction of precipitation which will fall as snow will decrease. Secondly, the snowpack will melt earlier in the season. The future change in precipitation is less certain (Lalande et al., 2021; Palazzi et al., 2013; Lutz et al., 2016; Ménégoz et al., 2013). Immerzeel et al. (2012) show a nearly constant annual contribution of snowmelt runoff to total runoff for the 21st century under increased temperature and precipitation. However, the largest changes in snowmelt runoff due to climate change mainly occur at the seasonal scale (Singh and Bengtsson, 2004). The snowmelt runoff increases in (early) spring, but decreases in summer by the end of the 21st century due to increasing temperature (Jeelani et al., 2012).

In general, the focus of snow modelling studies in the Himalaya has mainly been on quantifying snowmelt and snowmelt runoff. A significant part of the studies model snowmelt runoff in a simplistic way based on a combination of remotely sensed snow cover and a modelled melt flux. This melt flux is commonly quantified with a temperature index model or enhanced

temperature index model (Jeelani et al., 2012; Bookhagen and Burbank, 2010; Wulf et al., 2016; Singh and Jain, 2003; Armstrong et al., 2019). This provides no information about the snow water equivalent and the approach ignores other snow processes that influence either the energy and mass balance. Only few and more recent studies discuss spatiotemporal distribution of the snow water equivalent and/or additional snow processes besides melt and snowfall (Saloranta et al., 2019; Kraaijenbrink et al., 2021; Brown et al., 2014; Pritchard et al., 2020; Ragetti et al., 2015; Hegdahl et al., 2016). Hegdahl et al. (2016) tested the performance of different snowmelt representations for a catchment in the Indian Himalaya. Snowmelt was modelled using a temperature index model, enhanced temperature index model and an energy balance approach. Their study showed that the modelled discharge and model performance were more sensitive to the meteorological input than the choice of snowmelt representation. Pritchard et al. (2020) also investigated the influence of model process representation on simulated snowmelt (runoff) in a catchment in the western Himalaya. Their use of a model with a coupled energy and mass balance allows to also study the turbulent fluxes. The model simulations appear to be most sensitive to interactions with the parameterisations of snowpack hydrology, snow albedo and atmospheric stability effects on the turbulent fluxes (Pritchard et al., 2020). Snowpack hydrology links to refreezing as meltwater stored within the snowpack can potentially refreeze. Saloranta et al. (2019) made a first-order approximation of refreezing of snow meltwater in the Langtang catchment. 36% of total melt refreezes according to Saloranta et al. (2019). In their study snowmelt is modelled with the enhanced temperature index and the refreezing rate is related to (negative) air temperature. However, the melt parameters are estimated based on in situ meteorological and snow observations, which has been a new approach in the Himalaya. Veldhuijsen et al. (2022) studied refreezing in more detail using the same snow model in the same catchment and show the spatial and temporal variability of refreezing. The estimated maximum amount of refreezing is located at a height of 5850 m a.s.l. and amounts 38% of the snowmelt. They also show that refreezing mainly occurs in the non-monsoon seasons when snow is more abundant.

Only a small number of studies have investigated the surface energy balance based on in situ meteorological observations and modelling of the surface energy balance in the Himalaya (Datt et al., 2008; Azam et al., 2014; Matthews et al., 2020; Litt et al., 2019; Mandal et al., 2022; Soheb et al., 2018). These modelling studies show that net shortwave radiation is the main source of energy. Sublimation can be significant (16-42% of the total winter snowfall) and effectively reduces the energy available for warming of the snowpack or melting (Mandal et al., 2022). There is an ongoing discussion about whether considerable melt occurs at very high altitude above an elevation of 8020 m a.s.l. (Potocki et al., 2022; Brun et al., 2022). In the study of Potocki et al. (2022) a shallow ice core (10 m), retrieved from the South Col (8020 m a.s.l.) of Mount Everest, is interpreted and combined with energy balance modelling. They conclude that substantial melt occurs at this elevation. Even though, air temperature remains below the freezing point. However, Brun et al. (2022) convincingly argue that melt is not likely to occur at this elevation. One of the potential explanations why Potocki et al. (2022) simulate melt at this altitude, is that the used model settings are questionable (Brun et al., 2022). This discussion emphasizes the importance of performing field observations to constrain and validate model results and improve our understanding of the local meteorological and snow processes.

1.4 Research questions and thesis outline

Equations 1.1 and 1.2 summarize all snow processes that influence the mass and energy balance of a snowpack in alpine terrain. From the previous sections it becomes evident that snow studies in the Himalaya have only studied few of all these processes and have predominantly relied on remote sensing and modelling. Studies based on in situ observations are lacking, which hampers our understanding of the (seasonal) snowpack in the Himalaya. The relevance of the snow processes influencing the mass and energy balance of the snowpack, have remained largely unquantified in the Himalaya. Therefore, the main objective of this thesis is:

To improve the understanding of snow processes in the Himalaya by combining in situ observations of the seasonal snowpack with remote sensing and modelling.

In this thesis I focus on a selection of all the snow processes described in Equation 1.2. The focus is on accumulation of snow, melt, sublimation, evaporation, deposition, refreezing of snow meltwater and cold content dynamics of the snowpack. The research questions I aim to answer are:

1. *How much water is (seasonally) stored as a snowpack in a Himalayan catchment? And what is the sensitivity of the snowpack to changes in precipitation and air temperature?*

The actual amount of water that is stored as a snowpack, i.e. the snow water equivalent, has rarely been studied in the Himalaya and its quantity has hardly been validated. In Chapter 2, in situ snow depth observations and remotely sensed snow cover are assimilated in a snow model in order to simulate the snow water equivalent in the Langtang catchment in Nepal. A network of meteorological stations is used to drive the snow model. Also, in situ observations of snow cover and snow depth are used to validate the remotely sensed snow cover and simulated snow depth. Climate sensitivity tests are performed to study the change in snow water equivalent resulting of perturbed temperature and precipitation.

2. *What is the importance of snow sublimation in the high-altitude water cycle?*

Measurements of sublimation are non-existing in the Himalaya. I hypothesize that sublimation is a considerable amount as conditions at high altitude may be favorable for sublimation, i.e. low atmospheric humidity during winter, strong incoming solar radiation and high wind speeds. In Chapter 3, I use a one-month timeseries of unique eddy covariance observations to quantify the latent heat flux, and thus, sublimation, evaporation and deposition on a Himalayan glacier. These observations are additionally used to calibrate a model to simulate snow sublimation for the entire snow season and glacier-wide.

3. *What is the role of meltwater refreezing and cold content dynamics in the energy and mass balance of a seasonal snowpack at high altitude?*

Cold content dynamics of the snowpack have generally not been accounted for in snow models in the Himalaya. Similarly, our understanding of snow meltwater refreezing and snowmelt dynamics based on an energy-balance-approach is limited. In Chapter 4, I combine automated in situ observations of snow water equivalent and snow temperature to quantify the cold content dynamics of the seasonal snowpack at high altitude. In addition, in situ meteorological observations are combined with observed snow water equivalent at two high-altitude sites in order to understand the role of snow meltwater refreezing in the energy and mass balance of the snowpack at the two high-altitude sites.

These research questions focus on snow processes that influence the energy and mass balance of the snowpack, but have not, or only limited been quantified in the Himalaya. Each research question is discussed in a separate chapter. In the last chapter (Chapter 5), I will provide a synthesis of the main chapters and put my results in a broader perspective and discuss potential future research directions.

Chapter 2

Assimilation of snow cover and snow depth into a snow model to estimate snow water equivalent and snowmelt runoff in a Himalayan catchment

Snow is an important component of water storage in the Himalaya. Previous snowmelt studies in the Himalaya have predominantly relied on remotely sensed snow cover. However, snow cover data provide no direct information on the actual amount of water stored in a snowpack, i.e., the snow water equivalent (SWE). Therefore, in this study remotely sensed snow cover was combined with in situ observations and a modified version of the seNorge snow model to estimate (climate sensitivity of) SWE and snowmelt runoff in the Langtang catchment in Nepal. Snow cover data from Landsat 8 and the MOD10A2 snow cover product were validated with in situ snow cover observations provided by surface temperature and snow depth measurements resulting in classification accuracies of 85.7 and 83.1 % respectively. Optimal model parameter values were obtained through data assimilation of MOD10A2 snow maps and snow depth measurements using an ensemble Kalman filter (EnKF). Independent validations of simulated snow depth and snow cover with observations show improvement after data assimilation compared to simulations without data assimilation. The approach of modelling snow depth in a Kalman filter framework allows for data-constrained estimation of snow depth rather than snow cover alone, and this has great potential for future studies in complex terrain, especially in the Himalaya. Climate sensitivity tests with the optimised snow model revealed that snowmelt runoff increases in winter and the early melt season (December to May) and decreases during the late melt season (June to September) as a result of the earlier onset of snowmelt due to increasing temperature. At high elevation a decrease in SWE due to higher air temperature is (partly) compensated by an increase in precipitation, which emphasizes the need for accurate predictions on the changes in the spatial distribution of precipitation along with changes in temperature.

Based on: Stigter, E. E., Wanders, N., Saloranta, T. M., Shea, J. M., Bierkens, M. F. P., and Immerzeel, W. W. (2017), Assimilation of snow cover and snow depth into a snow model to estimate snow water equivalent and snowmelt runoff in a Himalayan catchment, *The Cryosphere* 11 (4), 1647–1664, doi: 10.5194/tc-11-1647-2017

2.1 Introduction

In the Himalaya a part of the precipitation is stored as snow and ice at high elevations. This water storage is affected by climate change resulting in changes in river discharge in downstream areas (Barnett et al., 2005; Bookhagen and Burbank, 2010; Immerzeel et al., 2009; Immerzeel et al., 2010). The Himalaya and adjacent Tibetan Plateau are important water towers, and water generated here supports the water demands of more than 1.4 billion people through large rivers such as the Indus, Ganges, Brahmaputra, Yangtze and Yellow River (Immerzeel et al., 2010). So far, the main focus has been on the effect of climate change on the glaciers and the resulting runoff. However, snow is an important short-term water reservoir in the Himalaya, which is released seasonally, contributing to river discharge (Bookhagen and Burbank, 2010; Immerzeel et al., 2009). The contribution of snowmelt to total runoff is highest in the western part of the Himalaya and lowest in the eastern and central Himalaya (Bookhagen and Burbank, 2010; Lutz et al., 2014).

Although Himalayan snow storage is important for the water supply in large parts of Asia, in situ observations of snow depth are sparse throughout the region. Many studies benefit from the continuous snow cover data retrieved from satellite imagery to estimate snow cover dynamics or contribution of snowmelt to river discharge (Bookhagen and Burbank, 2010; Gurung et al., 2011; Immerzeel et al., 2009; Maskey et al., 2011; Wulf et al., 2016). Studies about snowmelt in the Himalaya have predominantly relied on remotely sensed snow cover and a modelled melt flux estimating melt runoff resulting from this snow cover (e.g. Bookhagen and Burbank, 2010; Immerzeel et al., 2009; Tahir et al., 2011; Wulf et al., 2016). However, this approach provides no or limited information on snow water equivalent (SWE), which is an important hydrologic measure as it indicates the actual amount of water stored in a snowpack. SWE can be reconstructed based on the integration of a simulated melt flux over the time period of remotely sensed observed snow cover. However, this method provides only information on the peak SWE value and introduces errors when snowfall occurs during the melt season (Durand et al., 2008; Molotch, 2009; Molotch and Margulis, 2008). Currently there is only limited reliable information available on SWE for the Himalaya (Lutz et al., 2015; Putkonen, 2004). SWE can be retrieved with passive microwave remote sensing, but the results are highly uncertain, especially for mountainous terrain and wet snow (Dong et al., 2005). In addition, the spatial resolution is coarse and therefore inappropriate for catchment scale studies in the Himalaya. Estimating both the spatial and temporal distribution of SWE and snowmelt is important for flood forecasting, hydropower and irrigation in downstream areas.

Selection of a suitable snow model is critical to correctly represent snow cover and SWE. Snow models of different complexity exist and can be roughly divided into physically based and temperature-index models. Several studies have compared snow models of different complexity and their performance. Physically based models typically outperform temperature-index models in snowpack runoff simulations on a sub-daily timescale (Avanzi et al., 2016; Magnusson et al., 2011; Warscher et al., 2013). However, physically based and temperature-index models have a similar ability to simulate daily snowpack runoff (Avanzi et al., 2016; Magnusson et al., 2015). Avanzi et al. (2016) showed that the use of a temperature-index model does not result in a significant loss of performance in the simulation of SWE and snow depth with respect to a physically based model. Even though physically based models outperform temperature-index models in some cases, temperature-index models are often preferred, as data requirements and computational demands are lower. Especially in the Himalaya, data availability constrains the choice of a snow model.

Assimilation of remotely sensed snow cover and groundbased snow measurements has been

proved to be an effective method to improve hydrological and snow model simulations (Andreadis and Lettenmaier, 2006; Clark et al., 2006; Leisenring and Moradkhani, 2011; Liu et al., 2013; Nagler et al., 2008; Saloranta, 2016). Although different data assimilation techniques exist, Kalman filter techniques are often selected, due to their relatively low computation demand. They estimate the most likely solution using an optimal combination of observations and model simulations. Especially in catchments with strong seasonal snow cover, assimilation of remotely sensed snow cover is expected to be most useful as a result of fast changing conditions in the melting season (Clark et al., 2006).

The aim of this study is to estimate SWE and snowmelt runoff in a Himalayan catchment by assimilating remotely sensed snow cover and in situ snow depth observations into a modified version of the seNorge snow model (Saloranta, 2012; Saloranta, 2014; Saloranta, 2016). Climate sensitivity tests are subsequently performed to investigate the change of SWE and snowmelt runoff as result of changing air temperature and precipitation. The approach of modelling snow depth allows us to validate the quantity of simulated snow rather than snow cover alone and is a new approach in Himalayan snow research.

2.2 Methods and data

2.2.1 Study Area

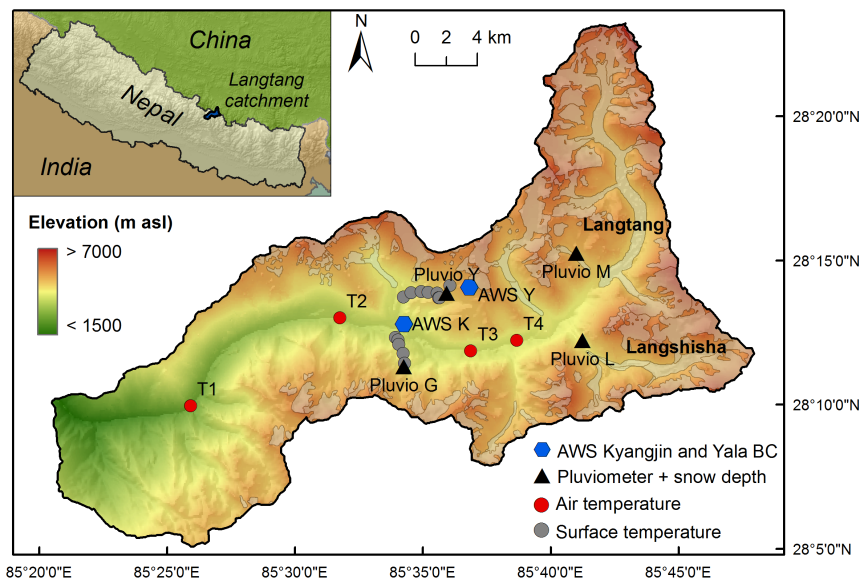


Figure 2.1: Study area with the locations of the in situ observations. Langtang and Langshisha refer to the two main glaciers in the upper Langtang valley.

The study area is the Langtang catchment, which is located in the central Himalayas approximately 100 km north of Kathmandu (Figure 2.1). The catchment has a surface area of approximately 580 km² from the outlet near Syabru Besi upwards. The elevation ranges from 1406 m above sea level (a.s.l.) at the catchment outlet to 7234 m a.s.l. for Langtang Lirung, which is the highest peak in the catchment. The climate is monsoon dominated and 68–89% of the annual precipitation falls during the monsoon (Immerzeel et al., 2014). Spatial pat-

terns in precipitation are seasonally contrasting, and there is a strong interaction between the orography and precipitation patterns. At the synoptic scale, monsoon precipitation decreases from south to north, but at smaller scales local orographic effects associated with the aspect of the main valley ridges (Barros et al., 2004) determine the precipitation distribution. Numerical weather models suggest that monsoon precipitation mainly accumulates at the southwestern slopes near the catchment outlet at low elevation, while winter precipitation mainly accumulates along high elevation southerneastern slopes (Collier and Immerzeel, 2015). Winter westerly events can also provide significant snowfall. Snow cover has strong seasonality with extensive, but sometimes erratic, winter snow cover and retreat of the snowline to higher elevations during spring and summer. For the upper part of the catchment (upstream of Kyangjin) it has been estimated that snowmelt contributes up to 40% of total runoff (Ragetti et al., 2015).

2.2.2 Calibration and validation strategy

2.2.3 Data sets

Remotely sensed snow cover MOD10A2

MOD10A2 is a Moderate Resolution Imaging Spectroradiometer (MODIS) snow cover product available at <http://reverb.echo.nasa.gov/>. The online sub-setting and reprojection utility was used to clip and project imagery for the Langtang catchment. MOD10A2 provides the 8-day maximum snow extent with a spatial resolution of ~ 500 m. If there is one snow observation within the 8-day period, then the pixel is classified as snow. The 8-day maximum extent offered a good compromise between the temporal resolution and the interference of cloud cover. The snow mapping algorithm used is based on the normalized difference snow index (NDSI; (Hall et al., 1995)). The NDSI is a ratio of reflection in shortwave infrared (*SWIR*) and green light (*GREEN*) and takes advantage of the properties of snow i.e., snow strongly reflects visible light and strongly absorbs SWIR (Equation (2.1)):

$$NDSI = \frac{GREEN - SWIR}{GREEN + SWIR} \quad (2.1)$$

The NDSI is calculated with MODIS spectral bands 4 (0.545–0.565 μm) and 6 (1.628–1.652 μm). Pixels are classified as snow when the $NDSI \geq 0.4$. Water and dark targets typically have high NDSI values, and, to prevent pixels from being incorrectly classified as snow, the reflection should exceed 10 and 11% for spectral bands 2 (0.841–0.876 μm) and 4 respectively for a pixel to be classified as snow (Hall et al., 1995). A full description of the snow mapping algorithm is given by Hall et al. (2002).

Landsat 8

Landsat 8 imagery from 15 April 2013 to 5 November 2014 was downloaded from <http://earthexplorer.usgs.gov/>. Cloudfree scenes (10 out of 34), based on visual inspection, were used to derive daily snow maps with high spatial resolution (30 m). For each image digital numbers were converted to top of atmosphere reflectance. For Landsat 8 the NDSI was calculated with Equation (2.1) with spectral bands 3 (0.53–0.59 μm) and 6 (1.57–1.65 μm). The chosen threshold value was equal to that used for the MOD10A2 snow cover product. The NDSI has proven to be a successful snow mapping algorithm for various sensors with a threshold value around 0.4 (Dankers and De Jong, 2004). Although the spectral bands have slightly different band widths and spectral positions, a threshold value of 0.4 gave satisfactory results when compared with in situ snow observations. In addition, the reflection in near-infrared light

should exceed 11% to prevent water from being incorrectly classified as snow (Dankers and De Jong, 2004). Therefore, a pixel is classified as snow when the NDSI value ≥ 0.4 and the reflectance in near-infrared light $> 11\%$.

In situ observations

Different types of snow and meteorological observations were available for the study period (January 2013–September 2014; Table 2.1, Figure 2.1). Two transects of surface temperature measurements on a north- and south-facing slope provided information on snow cover. The 13 temperature sensors (Hobo Tidbits) were positioned on the surface and covered by a small cairn and recorded surface temperature with 10-min sampling intervals. Snow depths were measured with sonic ranging sensors at four locations at 15-min intervals. Hourly measurements of snow depth were also made at the Kyangjin and Yala base camp automatic weather stations (AWS K and AWS Y; Figure 2.1). Hourly means (or totals) of air temperature, liquid and solid precipitation, and incoming shortwave radiation were also recorded at AWS Kyangjin (Shea et al., 2015b). Air temperature data were also acquired at several locations with 10- and 15-min recording intervals.

Table 2.1: Definition of measurement periods and seasons in this study

Description	Code	Data availability (dd-mm-yy)	Latitude	Longitude	Elevation m.a.s.l.	Observations
Yala 1	Y1	06/05/13–03/05/14	28.22645	85.56878	4117	TS
Yala 2	Y2	06/05/13–03/05/14	28.22897	85.57391	4214	TS
Yala 3	Y3	06/05/13–03/05/14	28.2298	85.58051	4328	TS
Yala 4	Y4	06/05/13–02/03/14	28.22932	85.58492	4441	TS
Yala 5	Y5	06/05/13–03/05/14	28.22894	85.5908	4541	TS
Yala 6	Y6	06/05/13–03/05/14	28.22635	85.5918	4656	TS
Yala 7	Y7	06/05/13–02/03/14	28.22635	85.59246	4759	TS
Yala 8	Y8	06/05/13–02/03/14	28.23342	85.59921	4960	TS
Ganjala 1	G1	03/11/13–11/10/14	28.20305	85.56405	3908	TS
Ganjala 2	G2	03/11/13–06/09/14	28.20155	85.56577	3998	TS
Ganjala 3	G3	03/11/13–11/10/14	28.19899	85.56617	4094	TS
Ganjala 4	G4	03/11/13–30/04/14	28.1938	85.56916	4201	TS
Ganjala 5	G5	03/11/13–11/10/14	28.18831	85.57001	4300	TS
Pluvio Yala	Pluvio Y	01/01/13–30/06/13 26/10/13–16/10/14	28.22900	85.59700	4831	T, SD
Pluvio Ganjala	Pluvio G	20/01/14–03/05/14	28.18625	85.56961	4361	SD
Pluvio Langshisha	Pluvio L	29/10/13–01/07/14	28.20265	85.68619	4452	SD
Pluvio Morimoto	Pluvio M	17/05/13–09/10/14	28.25296	85.68152	4919	T, SD
Lama Hotel	T1	01/01/13–07/10/14	28.16212	85.43073	2492	T
Langtang	T2	01/01/13–07/10/14	28.21398	85.52745	3557	T
Jathang	T3	01/01/13–07/10/14	28.1958	85.6132	3947	T
Numthang	T4	01/01/13–07/10/14	28.20213	85.64313	3983	T
AWS Kyangjin	AWS K	01/01/13–07/10/14	28.2108	85.5695	3862	T, SD, P, IR
AWS Yala base camp	AWS Y	01/01/13–07/10/14	28.23252	85.61208	5090	SD

2.2.4 Model forcing

The snow model was forced with daily average and maximum air temperature, cumulative precipitation and average incoming shortwave radiation for the time period January 2013–September 2014. Hourly measurements of air temperature, precipitation and incoming shortwave radiation at AWS Kyangjin (Shea et al., 2015b) were therefore aggregated to daily values. This study period was chosen based on availability of forcing data and observations.

Table 2.2: Parameters in the snow model. Initial value indicates the uncalibrated parameter value and the value range indicates the range which is used for the sensitivity analysis. Sensitivity of snow depth (SD) and snow extent (SE) represents the difference between the 90th and 10th percentile of mean snow depth and snow extent resulting from the sensitivity analysis.

Parameter	Unit	Description	Initial value	Value range	Sensitivity	
					SD (mm)	SE (km ²)
T_T	°C	Threshold temperature for onset of melt or refreezing	0 ^g	-6-2 ^{d,f,i,g}	157.3	57.25 ^g
F_{SR}	m ² mm W ⁻² d ⁻¹	Melt factor dependent on incoming shortwave radiation	0.15 ^g	0.13-0.19 ^{d,g}	9.486	2.721
F_T	mm °C ⁻¹ d ⁻¹	Melt factor dependent on temperature	4.32 ^g	2.54-5.19 ^{d,g}	9.486	2.721
thr_{snow}	°C	Threshold for partitioning in rain or snow	0 ^g	-1-1 ^{e,i,g}	35.82	11.99
C_{rf}	mm °C ⁻¹ d ⁻¹	Degree-day refreezing factor	0.16 ^e	0.08-0.40 ^e	8.188	0.3248
α_{ini}	-	Decay of albedo deep snow (initial)	0.713 ^b	-	-	-
α_u	-	Albedo of surface underlying snow (ground, ice)	0.15, 0.25 ^g	-	-	-
α_1	-	Decay of albedo deep snow	0.112 ^b	0.112-0.34 ^{b,g}	56.39	7.279
α_2	-	Decay of albedo shallow snow	0.442 ^b	0.3-0.5	0.2410	0.2818
α_3	-	Decay of albedo shallow snow (exponent)	0.058 ^b	0.03-0.1	0.2001	0.2132
r_{max}	-	Maximum allowed fraction of liquid water in snowpack	0.1 ^e	0.05-0.20 ^e	31.66	0.3278
d^*	cm	Scaling length for smooth transition albedo from deep snow to shallow snow	2.4 ^b	1-25	0.0012	0.0007
SS_1	m	Regression function of parameter snow holding depth dependence on slope angle	250 ^g	200-300	10.86	2.033
SS_2	-	Regression function of parameter snow holding depth dependence on slope angle	0.172 ^g	0.16-0.19	26.45	7.170
S_{min}	°	Minimum slope for avalanching to occur	25 ^a	15-35	34.00	1.640
ρ_{av}	kg L ⁻¹	Density of avalanching snow	0.200 ^c	-	-	-
ρ_{min}	kg L ⁻¹	Minimum density of new snow due to snowfall	0.050 ^e	0.050-0.15 ^e	-	-
α_{ns}	-	Coefficient for density of new snow	100 ^e	-	-	-
η_0	MN s m ⁻²	Coefficient related to viscosity of snow(at zero temperature and density)	7.6 ^e	1-10 ^e	75.75	-
C_5	°C ⁻¹	Coefficient for temperature effect on viscosity	0.1 ^e	0.04-0.12 ^e	10.44	-
C_6	L kg ⁻¹	Coefficient for density effect on viscosity	21 ^e	15-35 ^e	268.8	-
k_{comp}	-	Compaction factor	0.5 ^e	-	-	-
P	-	Precipitation correction factor	1	0.6-1.4	320.1	14.17
T_{lapse}	-	Temperature lapse rate correction factor	1	0.9-1.1	116.0	24.63

^aBernhardt and Schulz (2010), ^bBrock et al. (2000), ^cHopfinger (1983), ^dPellicciotti et al. (2012), ^eSaloranta (2014), ^fRagetti et al. (2013), ^gRagetti et al. (2015)

Daily temperature lapse rates were interpolated from the air temperature measurements throughout the catchment and used to extrapolate (average and maximum) daily air temperature observed at AWS Kyangjin (Figure 2.1). The derived temperature lapse rates agree with the values found by (Immerzeel et al., 2014). The daily observed precipitation and temperature lapse rates were corrected in the modified seNorge snow model with the correction factors P and T_{lapse} respectively to account for the uncertainty related to undercatch and the derived temperature lapse rates (Table 2.2). Although temperature has a strong relation with altitude and can be accurately derived from multiple weather stations at different altitudes, small differences in the temperature lapse rate (e.g., $0.001 \text{ }^\circ\text{C m}^{-1}$) can result in temperature differences of up to several degrees at high altitude in Langtang due to the extreme topography (Immerzeel et al., 2014). Hence, there is a need to consider a potential correction on the temperature lapse rate. A correction is also applied to the daily observed precipitation as precipitation measurements are typically biased due to wind-induced undercatch, especially for solid precipitation (Wolff et al., 2015). Collier and Immerzeel (2015) modelled the spatial distribution of precipitation in Langtang using an interactively coupled atmosphere and glacier mass balance model (Collier et al., 2013). Their study revealed seasonally contrasting spatial patterns of precipitation within the catchment. Monthly modelled precipitation fields from this study were therefore normalized and used to distribute the observed precipitation at AWS Kyangjin. Similarly, a radiation model (van Dam, 2001; Feiken, 2014) was used to extrapolate observed incoming shortwave radiation. The radiation model takes into account the aspect, slope, elevation and shading due to surrounding topography.

The model initial conditions for January 2013 (i.e., SWE and snow depth) were set by simulating year 2013 three times.

2.2.5 Modified seNorge model

The seNorge snow model (Saloranta, 2012; Saloranta, 2014; Saloranta, 2016) is a temperature-index model which requires only data of air temperature and precipitation. In addition, the seNorge snow model includes a compaction module that can be used to assimilate and validate snow depth rather than snow cover only. The low data requirements and the compaction module make the seNorge snow model suitable for application in this study.

The seNorge snow model was rewritten from its original code into the environmental modelling software PCRaster Python (Karssenberget al., 2010) to allow spatiotemporal modelling of the SWE and runoff within the catchment. The snow is modelled as a single homogeneous layer with a spatial resolution of 100 m and a daily time step. The seNorge model was further improved by implementing a different melt algorithm, albedo decay and avalanching. These novel model components are described hereafter, and the model parameters used are given in Table 2.2.

Water balance and snowmelt

Precipitation in the model is partitioned as rain or snow based on an air temperature threshold thr_{snow} ($^\circ\text{C}$). The snowpack consists of a solid component and possibly a liquid component. Meltwater and rain can be stored within the snowpack until its water holding capacity is exceeded and has the possibility to refreeze within the snowpack. The original melt algorithm of the seNorge snow model is substituted by the enhanced temperature-index approach (Pellicciotti et al., 2005; Pellicciotti et al., 2008). When air temperature (T ; $^\circ\text{C}$) exceeds the temperature threshold for melt onset (TT ; $^\circ\text{C}$), the potential melt (M_{pot} ; mm d^{-1}) is calculated for each pixel by Equation 2.2:

$$M_{pot} = T * F_T + F_{SR} * (1 - \alpha) * R_{inc} \quad (2.2)$$

where F_{SR} ($\text{m}^2 \text{ mm W}^{-2} \text{ d}^{-1}$) is a radiative melt factor, F_T ($\text{mm } ^\circ\text{C}^{-1} \text{ d}^{-1}$) is a temperature melt factor, α (-) is the albedo of the snow cover and R_{inc} (W m^{-2}) is the incoming shortwave radiation. In case that the threshold temperature is negative, the potential melt can become negative when the radiation melt component is not positive enough to compensate for the negative temperature melt component. When the potential melt is negative it is set to zero to prevent negative values.

The simulated runoff in the seNorge snow model is the total runoff, i.e., the sum of snowmelt and rain. As the focus of this study is on snowmelt runoff it is necessary to split the runoff in snowmelt and rain runoff. Meltwater and rain fill up the snowpack until its water holding capacity is exceeded. The surplus is defined as snowmelt and rain runoff respectively. If both rain and snowmelt occur it is assumed that rain saturates the snowpack first. Rain falling on snow-free portions of the basin is included in the rain runoff totals.

Albedo decay

Decay of the albedo of snow is calculated with the algorithm developed by Brock et al. (2000) in which the albedo is a function of cumulative maximum daily air temperature T_{max} ($^\circ\text{C}$). When T_{max} is above 0°C the air temperature is summed as long as snow is present and no new snow has fallen. When T_{max} is below 0°C the albedo remains constant. Albedo decay is calculated differently for deep snow ($\text{SWE} \geq 5 \text{ mm}$) and shallow snow ($\text{SWE} < 5 \text{ mm}$). The albedo decay for deep snow is a logarithmic decay, whereas the decay for shallow snow is exponential. This results in a gradual decrease of the albedo for several weeks, which agrees with reality (Brock et al., 2000). When new snow falls the albedo is set to its initial value. In Langtang the observed albedo of fresh snow is 0.84 and the observed minimum precipitation rate to reset the snow albedo is 1 mm d^{-1} (Ragettli et al., 2015).

Avalanching

After snowfall events, avalanching occurs regularly on steep slopes in the catchment. Therefore, snow transport due to avalanching is considered to be an important process for redistribution of snow in the Langtang catchment (Ragettli et al., 2015). Snow avalanching is implemented in the model using the SnowSlide algorithm (Bernhardt and Schulz, 2010). For each cell a maximum snow holding depth SWE_{max} (m), depending on slope S ($^\circ$), is calculated using an exponential regression function following Equation 2.3:

$$\text{SWE}_{max} = SS_1 * e^{-SS_2 * S} \quad (2.3)$$

where SS_1 and SS_2 are empirical coefficients. If SWE exceeds SWE_{max} and the slope exceeds the minimum slope S_{min} for avalanching to occur, then snow is transported to the adjacent downstream cell. Snow can be transported through multiple cells within one time step.

As the snowpack is divided into an ice and liquid component, both the ice and liquid components should be transported downwards. Avalanches in the Langtang catchment mainly occur at high elevations where temperatures are low and (almost) no liquid water is present in the snowpack. It is therefore assumed that avalanches are dry avalanches and that no liquid water is present in the avalanching snow. When there is, in rare circumstances, liquid water present in avalanching snow, the liquid water is converted to the ice component to ensure water balance closure.

Compaction and density

The compaction module is described in detail in Saloranta (2014) and Saloranta (2016). In this module SWE is converted into snow depth. Change in snow depth occurs due to melt, new

snow and viscous compaction. The change in snow depth due to new snow is adapted such that an increase in snow depth can occur due to both snowfall and deposition of avalanching snow. The increase in snow depth due to deposition of avalanching snow is calculated using a constant snow density for dry avalanches (200 kg m^{-3} ; (Hopfinger, 1983)).

2.2.6 Data assimilation

Sensitivity analysis

In order to assess which model parameters to calibrate, a local sensitivity analysis was performed by varying the value of one parameter at a time while holding the values of other parameters fixed. This gives useful first order estimates for parameter sensitivity, although it cannot account for parameter interactions. Plausible parameter values were based on the literature (Table 2.2). The model was run in Monte Carlo (MC) mode with 100 realisations for each parameter. The values for the parameters were randomly chosen from a uniform distribution with defined minimum and maximum values for the parameters. The snow extent and snow depth were averaged over the study period and study area for the sensitivity analysis. The sensitivity of the modelled mean snow extent and mean snow depth were compared to the changes in parameter values. A pixel is determined to be snow covered in the model when the simulated SWE exceeds 1 mm. All the parameters were varied independently per run, except for the melt factors F_T and F_{SR} , as these are known to be dependent on each other (Ragetti et al., 2015). Therefore, F_T and F_{SR} were varied simultaneously in the sensitivity analysis using a linear relation between these melt factors.

Parameter calibration

Using the ensemble Kalman filter (EnKF; Evensen, 1994), data assimilation of snow extent and snow depth observations was used to calibrate model parameters using the framework developed by Wanders et al. (2013). Both the EnKF and particle filter (PF) have been used in several studies to assimilate snow observations into snow models (e.g. Charrois et al., 2016; Leisenring and Moradkhani, 2011; Liu et al., 2013; Magnusson et al., 2016). The EnKF and PF are similar in their approach (estimate the model uncertainty from the particle or ensemble spread). The EnKF can only be used for assimilation of continuous values and not for binary values (i.e., snow cover present or not). Therefore, it is necessary to assimilate snow extent (continuous values) into the model, which results in a partial loss of spatial information of snow cover. However, the EnKF has a higher efficiency when it deals with Gaussian data and related errors. The computational demand required for a PF exceeds the EnKFs computer requirements, due to the need to cover the entire (non-Gaussian) distribution. When the number of particles becomes too low, there is an additional risk of particle collapse, especially when one wants to take into account all the grid cells in the simulation with or without snow. This would require a total particle number exceeding the total number of grid cells in the domain, in combination with all the possible parameter combinations to avoid collapse of the filter. For a single site or small sites a PF would be a good alternative (e.g. Charrois et al., 2016; Magnusson et al., 2016), but, limited by the current available computational power, this is only feasible with an EnKF implementation. As we deal with continuous values, it is computationally efficient and allows for dual-state parameter estimations. The lower number of ensemble members compared to a PF allowed us to run multiple simulations over longer time periods, providing a better estimate of the potential of the EnKF improvements.

An advantage of the EnKF calibration framework is that it allows for the obtaining of an uncertainty estimate for the calibrated parameters. The EnKF obtains the simulation uncertainty by using an MC framework, where the spread in the ensemble members represents the combined uncertainty of parameters and input data. Unfortunately, the EnKF does not allow

us to reduce and estimate the model structure uncertainty, since it relies on the assumption that the ensemble members are normally distributed. This assumption is no longer valid if multiple model schematizations are used. Therefore, it is assumed that the model is capable of accurately simulating the processes, when provided with the correct parameters. Besides the parameter and model uncertainty, there is uncertainty in the observations which are assimilated. The EnKF finds the optimal solution for the model states and parameters, based on the observations and modelled predicted values and their respective uncertainties. With sufficient observations the parameters will convert to a stable solution with an uncertainty estimate that is dependent on the observations error and the ability of the model to simulate the observations. It was found that 50 ensemble members are sufficient to obtain stable parameter solutions and correctly represent the parameter uncertainty.

The EnKF was applied for each time step that observations were available. The MOD10A2 snow extent was divided into six elevation zones. The snow extent per elevation zone was derived from the MOD10A2 snow cover and used for assimilation to include more information on spatial distribution of snow. The elevation zone breakpoints are at 3500, 4000, 4500, 5000 and 5500 m a.s.l. Snow maps with more than 30% cloud cover and with obvious misclassification of snow were exempted from assimilation (3 snow maps out of 88). Only for cloud-free pixels, comparisons were made between modelled and observed snow extent. Two snow depth observation locations (Pluvio Langshisha and AWS Kyangjin; Figure 2.1) were also assimilated.

The EnKF framework allows for the inclusion of an uncertainty in the assimilated observations. Point snow depth measurements have high uncertainties that are related to limited representativeness of point snow depth observations in complex terrain due to local influence of snow drift (Grünewald and Lehning, 2015). For the snow depth measurements a variance of 25 cm was chosen to represent the uncertainty of point snow depth measurements. The MOD10A2 snow extent was assigned an uncertainty based on the classification accuracy (fraction of correctly classified pixels) determined with the in situ snow observations (Sect. 2.3.1). The uncertainty is dependent on the snow extent (SE ; m^2), i.e., an increase in uncertainty for an increase in snow extent. To prevent the uncertainty from becoming zero when there is no snow cover, the minimum variance for each zone was restricted to the average snow extent $\overline{SE_{zone}}$ (m^2) * the accuracy (-). Therefore, the variance σ^2 per elevation zone is defined following Equation 2.4:

$$\sigma^2 = \max((SE_{zone} * accuracy)^2, (\overline{SE_{zone}} * accuracy)^2) \quad (2.4)$$

The four most sensitive parameters (T_T , T_{lapse} , P and C_6) resulting from the sensitivity analysis were optimised based on the assimilation of snow depth and MOD10A2 snow extent. The first three parameters (T_T , T_{lapse} and P) influence both snow depth and snow extent and were optimised by assimilating MOD10A2 snow extent. The fourth parameter (C_6) is an empirical coefficient relating viscosity to snow density and only influences snow depth. C_6 was optimised by assimilating snow depth observations and taking into account the full uncertainty in the previously determined parameters. The two-step approach was chosen to restrict the degrees of freedom and to prevent unrealistic parameter estimates.

2.2.7 Climate sensitivity

Climate sensitivity tests were performed to investigate changes in SWE and snowmelt runoff as a result of temperature and precipitation changes. Climate sensitivity was tested by perturbing daily average air temperature, daily maximum air temperature and daily cumulative precipitation using a delta-change method. Immerzeel et al. (2013) extracted temperature

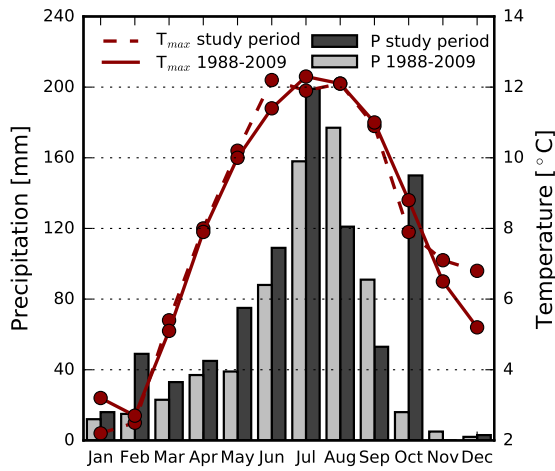


Figure 2.2: Comparison of maximum temperature (T_{max}) and cumulative monthly precipitation (P) for the study period (January 2013–September 2014) and the 1988–2009 time series (based on measurements in Kyangjin). The average yearly cumulative precipitation is 853 and 663 mm for the study period and the 1988–2009 time series respectively.

and precipitation trends from all available CMIP5 simulations for the emission scenario RCP 4.5 for the Langtang catchment. They selected four models that ranged from dry to wet and from cold to warm. Four climate sensitivity tests were performed based on the projected changes in temperature and precipitation found by Immerzeel et al. (2013) (Table 2.3).

Figure 2.2 shows the monthly cumulative precipitation and the average daily maximum temperature per month measured at AWS Kyangjin for the study period. These data are also available for the time period 1988–2009 and are used to characterize the climatology of the catchment. Comparison of the measurements of the 1988–2009 period and the study period shows that the maximum temperature is similar for both time periods, whereas more variability exists in the cumulative precipitation. Especially in October, a large difference exists in cumulative precipitation, which is caused by a large precipitation event of approximately 100 mm during the study period.

Table 2.3: Changes in temperature (ΔT) and precipitation (ΔP) for the climate sensitivity tests (same as Immerzeel et al. (2013)).

Sensitivity test	$\Delta T(^{\circ}C)$	$\Delta P(\%)$
Dry, cold	1.5	-3.2
Dry, warm	2.4	-2.3
Wet, cold	1.3	12.4
Wet, warm	2.4	12.1

2.3 Results and discussion

2.3.1 Validation of snow maps with in situ observations

In situ snow observations

Surface temperature is an indirect measure of presence of snow. Figure 2.3 shows observed surface temperature for two locations. Snow cover is distinguishable based on the low diurnal variability in surface temperature when snow is present due to the isolating effect of snow (Lundquist and Lott, 2008). An optimal threshold for distinguishing between snow and no snow was determined to be a 2 °C difference between daily minimum temperature and maximum temperature. The use of a larger temperature interval as threshold value was explored; however, as diurnal temperature variability is small during monsoon (Immerzeel et al., 2014), setting the diurnal cycle temperature threshold above 2 °C may result in incorrect monsoon snow observations.

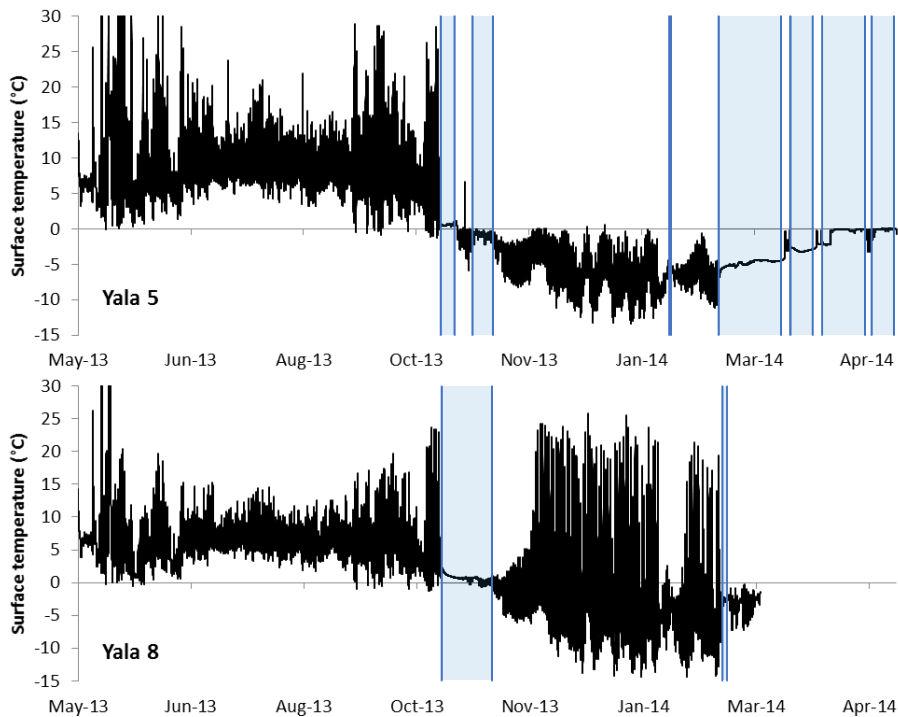


Figure 2.3: Observed surface temperature with 10-min interval at two locations (Table 2.1). The blue vertical lines indicate the start and end of the snow cover.

Remotely sensed snow cover

Both observed surface temperature and snow depth measurements were converted to daily and 8-day maximum binary snow cover values to validate Landsat 8 and MOD10A2 snow cover respectively. We find that the classification accuracy of MOD10A2 and Landsat 8 snow maps based on all in situ snow observations is 83.1 and 85.7% respectively. The classification accuracy is defined as the number of correctly classified pixels divided by the total number of pixels. Table 2.4 shows the confusion matrices. Misclassification can be a result of variability of snow conditions within a pixel and classification of ice clouds or high cirrus clouds as snow

(Parajka and Blöschl, 2006). Large viewing angles, and consequently larger observation areas, may also result in misclassification (Dozier et al., 2008). MOD10A2 has a lower spatial resolution than Landsat 8 which likely causes the slightly lower accuracy for the MOD10A2 snow cover product (Hall et al., 2002). Visual inspection of MOD10A2 snow maps also revealed that some clouds are erroneously mapped as snow cover.

The accuracy of MODIS daily snow cover products are reported to be 95% for mountainous Austria (Parajka and Blöschl, 2006) and 94.2% for the upper Rio Grande basin (Klein and Barnett, 2003). The lower accuracy presented in this study is likely a result of the simplification of the 8-day composite product and more extreme relief and consequently larger spatial variability in snow cover. Besides classification errors, uncertainty in the in situ snow observations should be considered as well. For the in situ snow cover observations provided by surface temperature, there are relatively many observations for which snow is not observed in situ, while the MOD10A2 and Landsat 8 snow maps indicate that snow should be present (Table 2.5). This may be caused by the fact that a thin snow layer may not result in sufficient isolation to reduce the diurnal temperature fluctuations for observation as snow (Lundquist and Lott, 2008). This observation bias in the temperature-sensed snow cover data would indicate that MOD10A2 and Landsat 8 snow maps possibly have even higher accuracies than presented here based on this validation approach.

Table 2.4: Confusion matrices for comparison of Landsat 8 snow maps and MOD10A2 snow maps with in situ snow observations.

	MOD10A2		Landsat 8	
	Snow	No snow	Snow	No snow
In situ snow	83	31	20	3
In situ no snow	75	438	18	106

Table 2.5: Confusion matrices for comparison of in situ snow observations provided by snow depth and surface temperature observations with remotely sensed snow maps (MOD10A2 and Landsat 8 combined).

	In situ snow depth		In situ surface temperature	
	Snow	No snow	Snow	No snow
Remotely sensed snow	52	16	51	77
Remotely sensed no snow	17	80	17	464

2.3.2 Model calibration

The results of the sensitivity of mean snow extent and mean snow depth to parameter variability are shown in Table 2.2. The sensitivity analysis shows that the threshold temperature for melt onset (T_T), precipitation bias (P), temperature lapse rate bias (T_{lapse}) and the coefficient for conversion for viscosity (C_6) are the most sensitive parameters. For the snow compaction parameters, snow depth is most sensitive for changes in C_6 , which is in agreement with (Saloranta, 2014). The melt parameters F_{SR} and F_T influence melt directly but show small sensitivity, as these parameters are dependent on each other. A higher value for F_T coincides with a lower value for F_{SR} where the value of both parameters is climate zone dependent (Ragetti et al., 2015).

Only the four most sensitive parameters were chosen to be calibrated by the EnKF to limit

the degrees of freedom and to prevent the absence of convergence in the solutions for the parameters. Table 2.6 shows the prior and posterior parameter distribution resulting from the assimilation of snow extent per zone and snow depth. The parameter values for T_{lapse} , P and C_6 show a narrow posterior distribution (i.e., small standard deviation) indicating that parameter uncertainty is small. T_{lapse} and P represent measurement uncertainties of the model inputs. After calibration the modelled precipitation is increased and the temperature lapse rate is slightly steeper (more negative) than derived. The calibrated value of T_T shows a large standard deviation indicating absence of convergence in parameter solutions. This can be either a result of insufficient data to determine the parameter value or insensitivity of the model to the parameter value. A negative value for T_T is plausible as melt can occur with air temperatures below 0 °C when incoming shortwave radiation is sufficient. Especially at low latitudes and high elevation, solar radiation is an important cause of snowmelt (Bookhagen and Burbank, 2010). T_T is reported to be as negative as -6 °C for Pyramid Station, Nepalese Himalaya (Pellicciotti et al., 2012). Here T_T lies in a range which is even more negative than -6 °C. This is likely to be partly a result of the model structure. When T_T is negative the melt algorithm (Equation 2.2) can give negative values. The temperature term in Equation 2.2 becomes negative in case the air temperature is below zero degrees but higher than T_T . The reason for negative melt to occur in a few rare cases is a limitation of the EnKF calibration in combination with the enhanced temperature-index method. The EnKF does not allow us to constrain parameter ranges and this results in a relative low T_T , which may occasionally lead to negative melt when incoming shortwave radiation is low and the air temperature is above T_T . In those cases when negative melt occurs, it is capped to zero, and as a result the model is relatively insensitive for low temperatures close to the T_T and the EnKF does not converge into a parameter solution.

Table 2.6: Parameter value range prior to calibration and after calibration. The standard deviation of posterior parameter values is based on the standard deviation of all members.

Parameter	Prior (min-max)	Posterior mean	Posterior standard deviation
T_T	-6 – 2	-8.18	1.66
T_{lapse}	0.9 – 1.1	1.1	0.01
P	0.6 – 1.4	1.31	0.02
C_6	15 – 35	16.07	0.52

2.3.3 Model validation

Snow cover

Both the modelled and MOD10A2 snow extent show strong seasonality of snow cover in the catchment (Figure 2.4). After calibration, modelled snow extent shows notable improvement in elevation zone 3500–4000 m a.s.l. during the melt season in 2014. After calibration the threshold temperature for melt onset is lower, resulting in more and earlier onset of snowmelt. Consequently there is a decreased snow extent. The zones in the lower areas are expected to show most improvement, as this is the area where snow cover is ephemeral, and considerable improvements of the modelled snow extent in elevation zone 3500–4000ma.s.l. are indeed observed (Figure 2.4). The root mean square error (RMSE) decreased from 14.2 to 11.2 km² after calibration. The simulated snow extent agrees well with MOD10A2-observed snow cover for the higher elevation zones (>4500 m a.s.l.). An exception is the snow extent in summer 2013 in the elevation zone 5000–5500 m a.s.l. The snow model underestimates the snow extent compared to the MOD10A2 snow extent. This discrepancy is possibly the

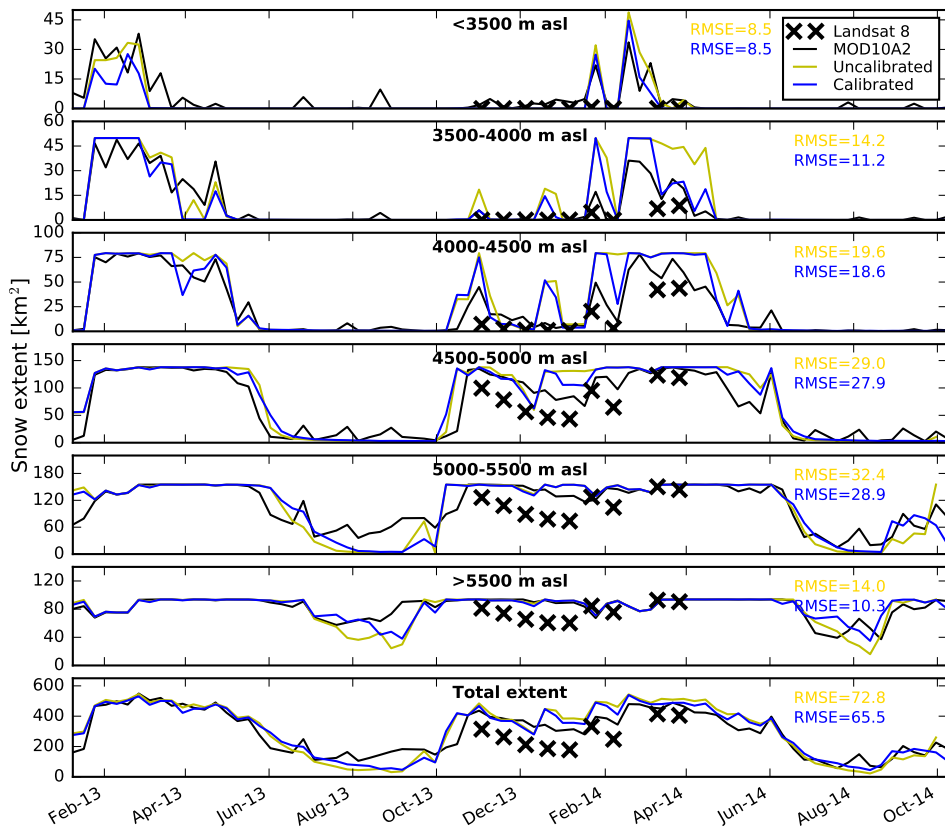


Figure 2.4: Modelled 8-day maximum snow extent before and after calibration (ensemble mean); Landsat 8 snow extent and MOD10A2 snow extent per elevation zone. The RMSE (km²) is given per zone for the fit between modelled (before and after calibration) and MOD10A2 snow extent.

result of (i) overestimation of simulated melt, (ii) an actual snow event that is simulated as rain by the model due to too high air temperature or (iii) erroneous mapping of clouds as snow in the MOD10A2 snow cover.

The model classification accuracy of snow cover after calibration is 85.9% based on pixel comparison between modelled 8-day maximum snow extent and MOD10A2 snow extent. The classification accuracy is the average classification accuracy over all members. There is only a slight increase of 0.2% in accuracy after calibration; however, the performance was already high (85.7 %) before calibration. The classification accuracy is lower on steep slopes where avalanching is common, and as the snow extent in avalanching zones is highly dynamic, this is not well captured in the model. Calibration of parameters that influence avalanching might overcome this discrepancy to some degree; however, a more advanced approach to avalanche modelling may be required. In addition, the spatial resolution of the remotely sensed snow cover is likely to be insufficient to detect the avalanche dynamics. Other potential explanations for lower classification accuracies are uncertainties related to the simulated precipitation phase (rain or snow) and the simulated spatial distribution of precipitation based on Collier

and Immerzeel (2015).

Landsat 8-derived snow extent is lower in winter than the modelled snow extent and the MOD10A2 snow extent (Figure 2.4). Distinct differences between the Landsat 8 instantaneous snow cover observations and the MOD10A2 8-day maximum snow cover extents (Figure 2.4) can be attributed to (i) the sensitivity of the Landsat 8 snow cover maps to misclassified snow pixels in the shaded area, (ii) the much higher spatial resolution of Landsat 8 (Hall et al., 2002), and (iii) the difference between an instantaneous image and an 8-day composite.

The model classification accuracy, based on pixel comparison with Landsat 8 snow maps, increased from 74.7 to 78.2% after calibration. In Table 2.7 individual model classification accuracy is given based on comparison with each Landsat 8 snow map. Relative low accuracies occur in winter (especially on 20 December 2013 and 5 January 2014), and the model overestimates snow cover compared to the Landsat 8 snow maps (Figure 2.4). The overestimation of snow cover by the model on 20 December 2013 is particularly large, and it can be explained by a small snow event (2.3 mm measured at Kyangjin) a few days before the acquisition. With below zero temperatures the model simulates a large snow cover extent, but based on a very small amount. Snow redistribution by wind, a patchy snow cover and/or sublimation may also explain the mismatch with the Landsat 8 snow cover in this particular case.

Table 2.7: Classification accuracy of modelled snow extent based on pixel comparison with Landsat 8 snow maps. Calibrated accuracies are averaged over all members and the standard deviation represents the standard deviation in individual member accuracies (after calibration).

Date (dd/mm/yy)	Accuracy uncalibrated (%)	Accuracy calibrated (%)	Standard deviation accuracy (%)
02/11/13	80.96	84.41	0.12
18/11/13	78.43	79.15	0.11
04/12/13	77.41	77.10	0.05
20/12/13	54.97	60.38	0.08
05/01/14	63.46	67.07	0.07
20/01/14	74.30	81.33	0.04
06/02/14	65.55	73.24	0.05
10/03/14	84.94	89.67	0.05
26/03/14	87.03	86.90	0.04
11/04/14	80.29	82.92	0.05

Snow depth

The observed and modelled snow depths at four locations are shown in Figure 2.5. The simulated snow depth is given for the model simulations i) without calibration, ii) after calibration of snow extent, and iii) after calibration of both snow extent and snow depth. After calibration with snow extent there is an increase in snow depth for Yala Pluvio and Yala BC for the entire snow season as a result of increased simulated precipitation. For Langshisha and Kyangjin the snow depth mainly decreased after calibration with snow extent. These stations are at a lower elevation, and, since the threshold temperature for melt onset is lowered after calibration, this leads to reduced snow depth. At all locations the modelled snow depth decreased after calibration with both snow extent and snow depth due to lowering of the parameter relating snow density to snow depth. After calibration with both snow extent and snow depth, comparison of modelled and observed snow depth at Langshisha shows good agreement. Especially after calibration, the timing of the melt onset during spring is

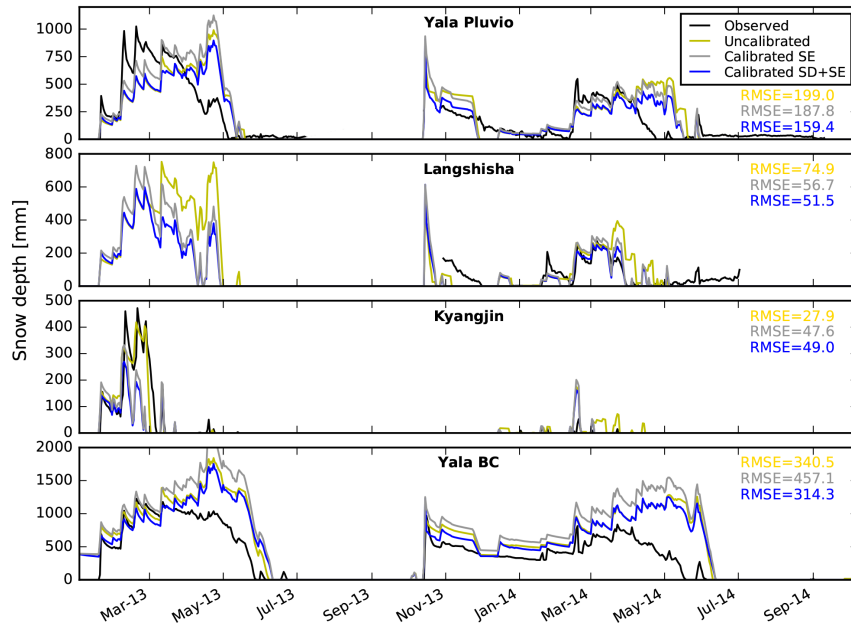


Figure 2.5: Observed snow depth and modelled snow depth (i) before calibration, (ii) after calibration of snow extent (SE), and (iii) after calibration of both snow extent and snow depth (SD+SE; ensemble mean) at three locations. The RMSE (mm) is given for the fit between modelled (before and after calibration) and observed snow depth.

improved. For Yala Pluvio and Yala BC the agreement between modelled and observed snow depth is also good, though improvement of the timing of melt onset is limited. For Kyangjin the modelled snow depth does not agree as well with observed snow depth in spring 2013, but it improves in 2014. In spring the snow cover duration of snow events decreases after calibration and improves the fit with the observed snow depth.

Yala Pluvio and Yala BC are the only locations that serve as an independent validation of snow depth, as these stations are not used for the assimilation. The simulated melt onset in spring is later compared to what is observed. The diurnal variability of air temperature is high during the pre-monsoon season (March to mid-June; Immerzeel et al., 2014)). Though, daily average air temperatures are below zero, positive temperatures and snowmelt can occur in the afternoon above 5000 m a.s.l. (Shea et al., 2015b; Ragetti et al., 2015). This can explain the difference between simulated and observed melt onset. Using an hourly time step might therefore improve the simulation of snowmelt in spring (Ragetti et al., 2015). While the timing of snowpack depletion at Yala Pluvio and Yala BC are offset from the observations, the modelled quantity of snow is in the same order of magnitude for both modelled and observed time series. Hence, there is no substantial overestimation or underestimation of snow depth. The RMSE between simulated and observed snow depth decreases after calibration with both snow extent and snow depth compared to the uncalibrated simulation of snow depth and after calibration of only snow extent. This shows the benefit of assimilating both snow extent and snow depth into the snow model to obtain optimal parameter values.

While this study shows an approach in using snow depth observations for assimilation and

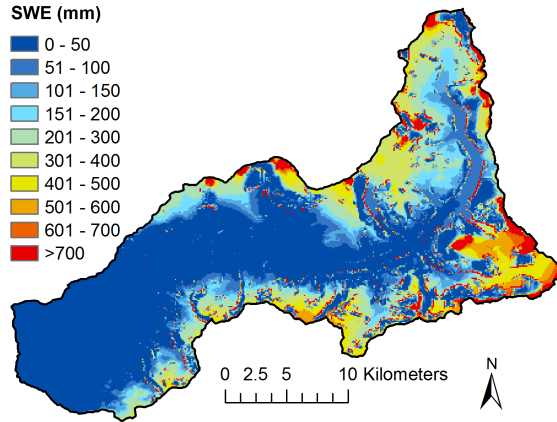


Figure 2.6: Spatial distribution of ensemble mean annual average snow water equivalent (SWE).

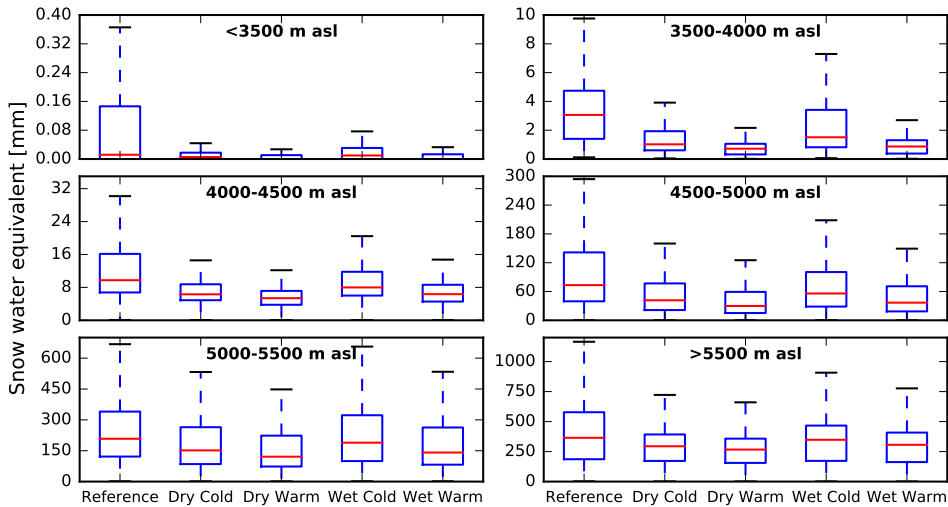


Figure 2.7: Boxplots of SWE per elevation zone averaged over the simulation period and all ensemble members for the study period (reference) and the four climate sensitivity tests (Table 2.3).

validation, only four locations with snow depth observations were available. The number of available snow depth observations and the choice of different stations for assimilation might influence the results. Four snow depth observations are insufficient for systematic assimilation and independent validation. However, our approach is useful and is recommended for future studies in the Himalaya, in particular when more point observations of snow depth are available.

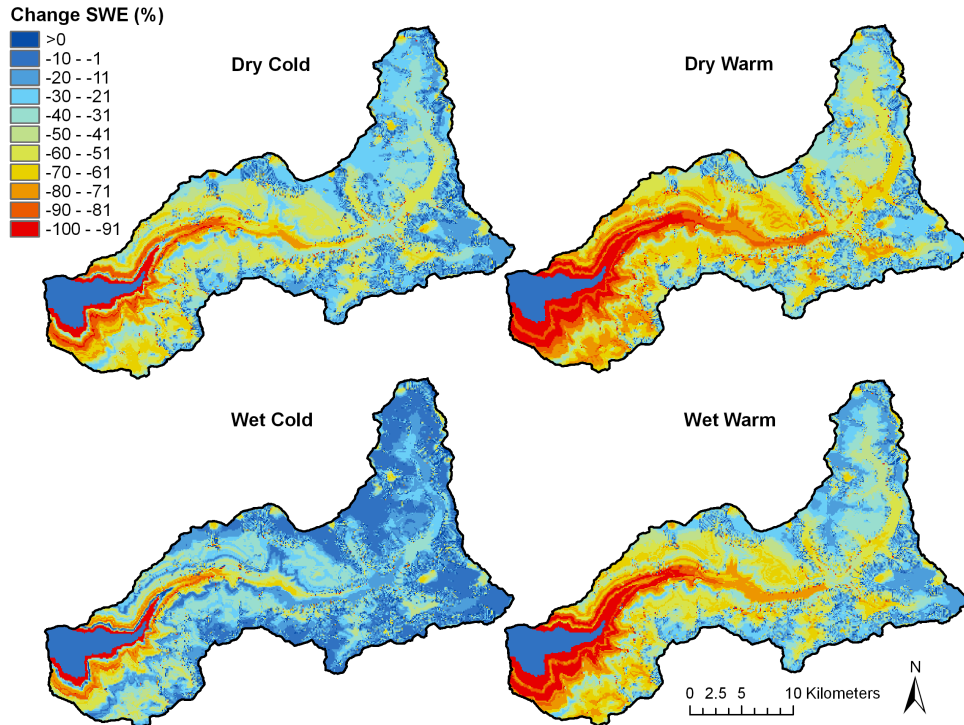


Figure 2.8: Change in SWE averaged over the simulation period and all members for each climate sensitivity test (Table 2.3).

2.3.4 Climate sensitivity of SWE and snowmelt runoff

The cumulative basin-wide mean snowfall is 1222 mm for the simulation period. Nearly one-third (31.4%) of the snowfall is transported to lower elevations due to avalanching, and 16.2% of the snowfall is transported to elevations lower than 5000 m a.s.l. Transport of snow to lower elevations contributes to snowmelt runoff and has been estimated to be 4.5% of the total water input for the upper part of the Langtang catchment (Ragettli et al., 2015).

The simulation of the SWE for the study period shows a pattern of increasing SWE with increasing elevation (Figures 2.6 and 2.7). At higher elevation, air temperature is lower with more snow accumulation than melt, resulting in a higher gain in SWE over time. The glaciers Langtang and Langshisha are positioned at approximately the same elevation (Ragettli et al., 2015), though the SWE is considerably higher at the Langshisha glacier (Figure 2.6) due to the precipitation distribution approach we use. Also, some areas at higher elevation show less SWE than surrounding areas at the same elevation. These areas represent the steep slopes in the catchment where avalanching occurs regularly. The transported snow accumulates below these steep slopes. The simulated avalanches are based on a simple model parameterization in which the snow is transported via single stream paths, resulting in a few pixels with extreme accumulation of SWE. This is mainly visible in the northeastern part of the catchment. Modelling the divergence of transported snow might improve the extreme accumulation simulated for some pixels.

For the climate sensitivity tests a delta-change method is used. This method has limita-

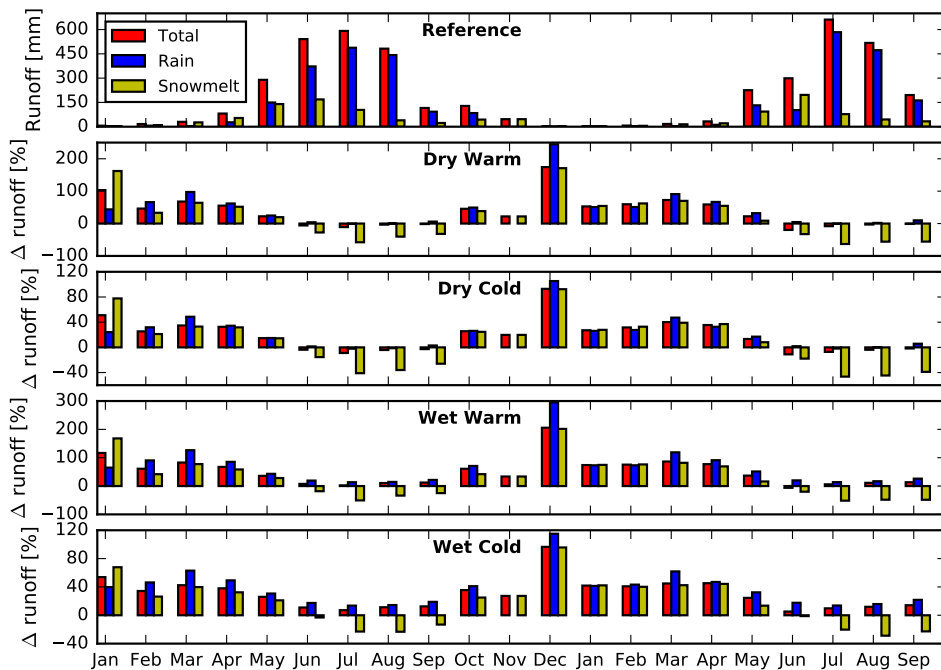


Figure 2.9: Modelled runoff at catchment outlet for the study period (January 2013–September 2014) and change in runoff compared to the study period for the climate sensitivity tests.

tions as climate variability of future climate is not constant compared to the study period (Kobierska et al., 2013). In addition, Kobierska et al. (2013) showed that changes in runoff due to climate change are predicted differently by a physically based snow model and a parameterised snow model for a glacierized catchment. Parameterised snow models (such as the modified seNorge snow model that is used in this study) are calibrated to fit the current climate and not future climate and might therefore be incapable of predicting future states of the snowpack. However, the scope of this study is to show the sensitivity of the SWE and snowmelt runoff to changes in air temperature and precipitation and not that of a full-fledged climate impact study. Therefore, the use of a parameterised snow model and the delta-change method is suitable in this case.

Figures 2.7 and 2.8 show the results of the absolute and relative change in SWE for different climate sensitivity tests. All climate sensitivity tests show a decrease in SWE, but the relative change is greatest at low elevations in the valley. We also observe a strong gradient of decreased relative change in SWE with increased elevation. An increase in temperature leads to an increase in melt and more precipitation in the form of rain instead of snow. Both processes result in decreased relative change of SWE with elevation. Near the catchment outlet there is an area with 100% decrease in SWE, as precipitation will only fall as rain instead of snow.

A slight deviation from the elevational trend in SWE change occurs between 3000 and 4000 m a.s.l., which is a zone that could be sensitive to changes in the elevation at which snowfall occurs. The combination of snowfall at higher elevations due to higher temperature and the

monthly differing spatial patterns in precipitation are likely to explain the banded patterns.

Changes in SWE and the spatial distribution of SWE will also be affected by changes in total precipitation. The influence of precipitation can be determined based on comparison of the two wet and dry climate sensitivity tests (Figures 2.7 and 2.8). A decrease in precipitation results in decreased SWE as there is less snowfall. However, the increased precipitation for the wet/cold and wet/warm climate sensitivity tests (+12.1 and +12.4% respectively) does not compensate for the temperature-related increase in melt and decrease in snowfall in the valley.

Reduced warming under the wet/cold climate sensitivity test results in a smaller decrease of SWE compared to the wet/warm climate sensitivity test, even in the valley. At higher elevations, changes in SWE are weakly negative and in some areas positive. Snowpack sensitivity to temperature change decreases with elevation (Brown and Mote, 2009). The increased SWE under both wet climate sensitivity tests occurs in the southeastern part of the catchment where relatively large amounts of precipitation occur in winter (Collier and Immerzeel, 2015). Schmucki et al. (2015) showed similar results for the Alps. They showed that low- and mid-elevation stations are sensitive to temperature change but not to precipitation change. In contrast, at high-elevation stations an increase in precipitation partly compensates for an increase in temperature. The compensating effect of increased precipitation at high elevations is important for glacier systems and emphasizes the importance of accurate estimations of both change in precipitation and its spatial distribution.

The modelled snowmelt and rain runoff at the catchment outlet is greatest during the monsoon and lowest during winter (Figure 2.9). Peak snowmelt and rain runoff occur in June and July respectively. The snowmelt season starts in March when temperatures and insolation are rising and continues until October. Snowmelt runoff contributes most to total runoff during pre-monsoon and early-monsoon (March–June), which is in agreement with (Bookhagen and Burbank, 2010). Validation of the simulated runoff with observed runoff was impossible, because (i) there were no reliable runoff data available for the study period, as there was no reliable rating curve, and (ii) the model focusses on rain and snowmelt runoff; however, glacier runoff and delay of runoff due to groundwater and glacier storage is not incorporated in the model structure.

The climate sensitivity of snowmelt and rain runoff is shown in Figure 2.9. All climate sensitivity tests show an increase in snowmelt runoff from October to May. In contrast, snowmelt runoff decreases from June to September. Higher temperatures result in more snowmelt and less snowfall during winter and an early melt season which leads to a shift in the peak of snowmelt runoff. In other mountain regions similar changes in runoff patterns appear. Several studies in the Alps show that the peak in snowmelt runoff shifts from summer to late spring (Bavay et al., 2009; Bavay et al., 2013; Kobierska et al., 2013). Immerzeel et al. (2009) showed that in the upper Indus Basin, the peak in snowmelt runoff appears 1 month earlier by 2071–2100 as result of an increase in temperature and precipitation. However, Immerzeel et al. (2012) showed that total snowmelt runoff remains more or less constant under positive temperature and precipitation trends in the upper part of the Langtang catchment. In their study snowmelt on glaciers is not defined as snowmelt runoff and is therefore a minor component of total runoff, leading to different results.

For the wet climate sensitivity tests, total runoff (i.e., the sum of snowmelt and rain runoff) increases throughout the year. The decrease in melt runoff during the late melt season is compensated by the increase in rain runoff as there is more precipitation. The future hydrology of the central Himalaya largely depends on precipitation changes, as it is dominated by rainfall runoff during the monsoon (Lutz et al., 2014). As we perturb the model with a percentage change in precipitation that is constant through the year, the absolute change in precipitation

is greater in the monsoon than in winter. For climate sensitivity tests with decreased precipitation, total runoff from June to September decreases, but from October to May it increases as a result of increased snowmelt. Estimates of seasonal changes in precipitation are thus critical for determining whether rain and snowmelt runoff increases or decreases during monsoon.

2.4 Conclusions

Remotely sensed snow cover, in situ observations and a modified seNorge snow model were combined to estimate (climate sensitivity of) SWE and snowmelt runoff in the Langtang catchment. Validation of remotely sensed snow cover (Landsat 8 and MOD10A2 snow maps) shows high accuracies (85.7 and 83.1% respectively) against in situ snow observations provided by surface temperature and snow depth measurements. Data assimilation of MOD10A2 snow cover and snow depth measurements using an EnKF proved to be successful for obtaining optimal model parameter values. Independent validations of simulated snow depth and snow cover against snow depth measurements and Landsat 8 snow cover show improvement after assimilation of snow depth and snow cover compared to results before data assimilation. The applied methodology of simultaneous assimilation of snow cover and snow depth allows for the calibration of important snow parameters and validation of the snow depth rather than snow cover alone. This opens up new possibilities for future snow assessments and sensitivity studies in the Himalaya.

The spatial distribution of SWE averaged over the simulation period (January 2013–September 2014) shows a strong gradient of increasing SWE with increasing elevation. In addition, the SWE is considerably higher in the southeastern part of the catchment than the northeastern part of the catchment as a result of the spatial and temporal distribution of precipitation.

Finally the climate sensitivity study revealed that snowmelt runoff increases in winter and the early melt season (December–May) and decreases during the late melt season (June–September) as a result of the earlier onset of snowmelt due to increasing temperature. There is a strong relative decrease in SWE in the valley with increasing temperature due to more snowmelt and less precipitation as snow. At higher elevations an increase in precipitation partly compensates for increased melt due to higher temperatures. The compensating effect of precipitation emphasizes the importance and need for the accurate prediction of change in the spatial and temporal distribution of precipitation.

2.5 Acknowledgements

This project was supported by funding from the European Research Council (ERC) under the European Unions Horizon 2020 research and innovation program (grant agreement no. 676819) and by the research programme VIDI with project number 016.161.308 financed by the Netherlands Organisation for Scientific Research (NWO). The authors thank Hendrik Wulf and two anonymous reviewers for their constructive comments that helped in improving the manuscript.

Chapter 3

The importance of snow sublimation on a Himalayan glacier

Snow sublimation is a loss of water from the snowpack to the atmosphere. So far, snow sublimation has remained unquantified in the Himalaya, prohibiting a full understanding of the water balance and glacier mass balance. Hence, we measured surface latent heat fluxes with an eddy covariance system on Yala Glacier (5350 m a.s.l) in the Nepalese Himalaya to quantify the role snow sublimation plays in the water and glacier mass budget. Observations reveal that cumulative sublimation is 32 mm for a 32-day period from October to November 2016, which is high compared to observations in other regions in the world. Multiple turbulent flux parameterizations were subsequently tested against this observed sublimation. The bulk-aerodynamic method offered the best performance, and we subsequently used this method to estimate cumulative sublimation and evaporation at the location of the eddy covariance system for the 2016–2017 winter season, which is 125 and 9 mm respectively. This is equivalent to 21% of the annual snowfall. In addition, the spatial variation of total daily sublimation over Yala Glacier was simulated with the bulk-aerodynamic method for a humid and non-humid day. Required spatial fields of meteorological variables were obtained from high-resolution WRF simulations of the region in combination with field observations. The cumulative daily sublimation at the location of the eddy covariance system equals the simulated sublimation averaged over the entire glacier. Therefore, this location appears to be representative for Yala Glacier sublimation. The spatial distribution of sublimation is primarily controlled by wind speed. Close to the ridge of Yala Glacier cumulative daily sublimation is a factor 1.7 higher than at the location of the eddy covariance system, whereas it is a factor 0.8 lower at the snout of the glacier. This illustrates that the fraction of snowfall returned to the atmosphere may be much higher than 21% at wind-exposed locations. This is a considerable loss of water and illustrates the importance and need to account for sublimation in future hydrological and mass balance studies in the Himalaya.

Based on: Stigter, E. E., Litt, M., Steiner, J. F., Bonekamp, P. N. J., Shea, J. M., Bierkens, M. F. P., and Immerzeel, W. W. (2018), The importance of snow sublimation on a Himalayan glacier, *Frontiers in Earth Science - Cryospheric Sciences* 6 (108), doi: 10.3389/feart.2018.00108

3.1 Introduction

Snow sublimation is a loss of water from the snowpack to the atmosphere due to the direct phase transition of snow to water vapour. Sublimation can occur from a static snow surface, and is enhanced under drifting and blowing snow conditions. Several studies have shown the importance of sublimation to the water balance in the Arctic (Box and Steffen, 2001), Antarctic (Van Den Broeke, 1997), Canadian Prairies (Pomeroy and Li, 2000), and alpine areas (Wagnon et al., 2003; Strasser et al., 2008; MacDonald et al., 2009; MacDonald et al., 2010; Bernhardt et al., 2012; Gascoïn et al., 2013; Marks et al., 2013; Vionnet et al., 2014; Zhou et al., 2014). Snow mass losses due to sublimation have been estimated to vary between 0.1 and 90% of total snowfall (Strasser et al., 2008; MacDonald et al., 2010; Groot Zwaaftink et al., 2013), depending on model approach, location and period of observation. For example, the sublimation due to blowing snow is also largely unknown (e.g. Brun et al., 2013), resulting in a wide variety of sublimation estimates. Based on previous research it is expected that the conditions at high altitude in the Himalaya favor sublimation, i.e., low atmospheric pressure, high wind speed and dry air (Wagnon et al., 2013). However, sublimation rates in the high-altitude Himalaya remain unquantified and the significance of sublimation to the high-altitude water balance is unknown. Consequently, quantifying high-altitude sublimation rates is essential to improve our understanding of the water balance in Himalayan catchments.

Many studies rely on simulated sublimation and lack validation with direct observations (e.g. Bowling et al., 2004; Gordon et al., 2006; MacDonald et al., 2010; Groot Zwaaftink et al., 2013). Two different methods for observing sublimation can be distinguished. The first is a gravimetric method, where the weight of a part of a snowpack is continuously monitored with a sublimation pan (Wagnon et al., 2003; Herrero and Polo, 2016). For conditions without snowmelt the decrease in weight is assigned to sublimation. However, wind-induced erosion of the snowpack also leads to reduced weight of the snowpack, which can be incorrectly interpreted as sublimation, resulting in high inaccuracies in the measurements. The second method is the eddy covariance method (e.g. Litt et al., 2015; Sexstone et al., 2016; Radic et al., 2017), which provides direct observations of turbulent fluxes that can be used to obtain the energy and mass exchange between the snow surface and atmosphere (Molotch et al., 2007; Reba et al., 2012). This method derives turbulent fluxes based on statistical analysis of high frequency data of the vertical wind component, air temperature and water vapour. The derived latent heat fluxes can be converted to sublimation rates using the latent heat of sublimation. Eddy covariance instrumentation is a proven methodology to quantify snow sublimation (Sexstone et al., 2016). However, this data needs extensive post-processing to derive reliable turbulent fluxes (Reba et al., 2009). The method relies on assumptions of both stationarity and homogeneity of the flow, which are violated in complex terrain and for stable boundary layers which are frequently found over snow-covered surfaces. Nevertheless, eddy covariance measurements have been successfully used to quantify snow sublimation over snow-covered surfaces in complex terrains (Reba et al., 2012; Sexstone et al., 2016) due to careful post-processing of the data.

Sublimation measurements give an estimate at the pointscale, while it has been found to vary significantly in space (e.g. Strasser et al., 2008). Turbulent fluxes have high spatial variability in complex terrain, which is mainly induced by local flow (Pohl et al., 2006; Gascoïn et al., 2013; Mott et al., 2015). Parameterizations have been developed at the point-scale to quantify sublimation. These parameterizations can be used to simulate and quantify spatially distributed sublimation at regional and catchment scales when meteorological input in space is available. Simple empirical relations between sublimation and nominal meteorological variables have been developed previously (Kuchment and Gelfan, 1996; Strasser et al.,

2008). However, empirical relations are often region-specific and may not be transferable between geographic regions. The more sophisticated Penman-Monteith approach combines the energy balance with mass transfer equations and is commonly used to estimate evapotranspiration and snow sublimation (Nakai et al., 1994; Mahrt and Vickers, 2005; Wimmer et al., 2009; Knowles et al., 2012). Other methods to estimate sublimation include the bulk-aerodynamic method and the aerodynamic profile method. The bulk-aerodynamic method requires measurements of meteorological variables at one measurement level and snow surface parameters, whereas the aerodynamic profile method requires measurements of meteorological variables at multiple levels. The bulk-aerodynamic method is commonly used in energy balance models to calculate turbulent fluxes between the surface and atmosphere, in which the models are forced with either meteorological distributed forecast or reanalysis data instead of point measurements. The bulk-aerodynamic method is associated with uncertainties that are related to the assumption of a logarithmic vertical wind profile and roughness lengths (Fitzpatrick et al., 2017). The assumption of a logarithmic wind profile is often violated over a snow covered surface as typically strongly stable atmospheric conditions, such as katabatic flow, suppress turbulent fluxes. Stability corrections are often applied to account for this (e.g. Radic et al., 2017; Schlögl et al., 2017). Many stability corrections have been developed, but the Monin-Obukhov length L is commonly applied to account for changing stability (Fitzpatrick et al., 2017; Radic et al., 2017; Schlögl et al., 2017). Though, the Monin-Obukhov similarity theory assumes a stationary, horizontally homogenous flow and constant flux layer. These assumptions are often violated in complex terrain and over snow cover, which makes application of the bulk aerodynamic method challenging on glaciers in complex terrain.

In this study eddy covariance observations were collected above the surface of a snow-covered glacier in Nepal at an altitude of 5350 m above sea level (a.s.l.) for a 32-day period in October–November 2016. Three parameterizations are compared to these measurements. The best performing parameterization is used to derive sublimation at the location of the eddy covariance system for the winter season 2016–2017. In addition, daily sublimation is estimated over Yala Glacier for two characteristic days, i.e., a humid and non-humid day, using a series of meteorological stations and high-resolution meteorological fields simulated with the Weather Research and Forecasting model (WRF; Skamarock and Klemp (2008)) with the aim to assess the importance of sublimation in the high-altitude water balance and glacier mass balance.

3.2 Study area

This study was conducted on Yala Glacier (Figure 3.1), a south-southwest facing clean-ice glacier. Yala Glacier is located in the central Himalaya in Nepal in Langtang Valley, and is part of the Trishuli River system. The surface area of Yala Glacier is approximately 1.5 km² and the elevation ranges from 5120 to 5615 m a.s.l. Baral et al. (2014) calculated a negative mass balance of -0.89 m w.e. for 2011–2012 based on observations. Over the last three decades Yala Glacier experienced a negative mass balance due to a decrease in accumulation area, a shift from snow to rainfall and accelerated glacier melt in the ablation zone as result of a warming climate (Fujita and Nuimura, 2011). The climate is characterized by monsoon precipitation in June, July, and August, and infrequent westerly storm events that bring snowfall during winter. 68 to 89% of the annual precipitation falls during the monsoon (Immerzeel et al., 2014). The elevation of the zero degree isotherm varies between approximately 6000 and 3500 m a.s.l. in monsoon and winter, respectively, in the Langtang catchment (Shea et al., 2015b).

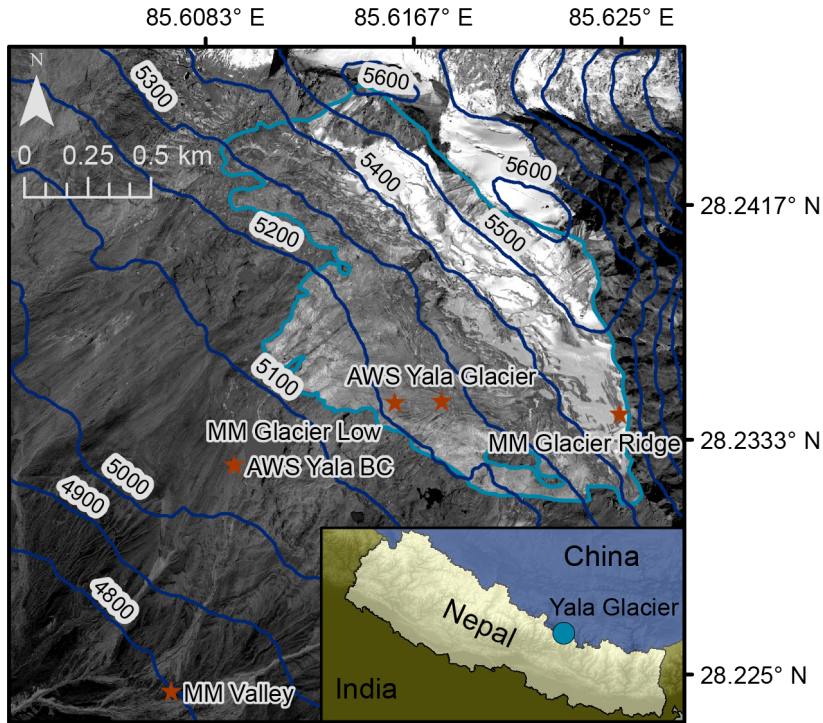


Figure 3.1: Study area, including the outline of Yala glacier (light blue), elevation contour lines (dark blue) and the locations of the three micro-met stations (MM), AWS Yala Glacier and AWS Yala Base Camp (stars). The inset shows the location of Yala Glacier in the central Himalaya, Nepal.

3.3 Data and methods

3.3.1 Instrument and data description

Meteorological data were collected between October 2016 and April 2017 with several automatic weather stations (AWSs) located on or adjacent to Yala Glacier (Figures 3.1 and 3.2, Table 3.1). AWS Yala Glacier and AWS Yala Base Camp, positioned on- and off-glacier respectively, recorded hourly shortwave and longwave radiation, air temperature, relative humidity, wind speed and wind direction. AWS Yala Base Camp also recorded atmospheric pressure. Additionally, an open-path infrared analyser and 3-d anemometer (Campbell Scientific IR-GASON) measured the 3-d wind components, sonic temperature and water vapour density (eddy covariance system) at the AWS Yala Glacier site. These measurements were recorded at 10 Hz frequency in the 2016–2017 winter period, but available measurements were limited to 15 October–17 November due to a corrupt data collection card. In addition to the AWSs, three small meteorological stations were installed on- and off-glacier. These micro-met stations recorded air temperature, relative humidity, atmospheric pressure, wind speed and wind direction with a 15-min time interval. A pluviometer, located approximately 9 km south of Yala Glacier, monitored precipitation.

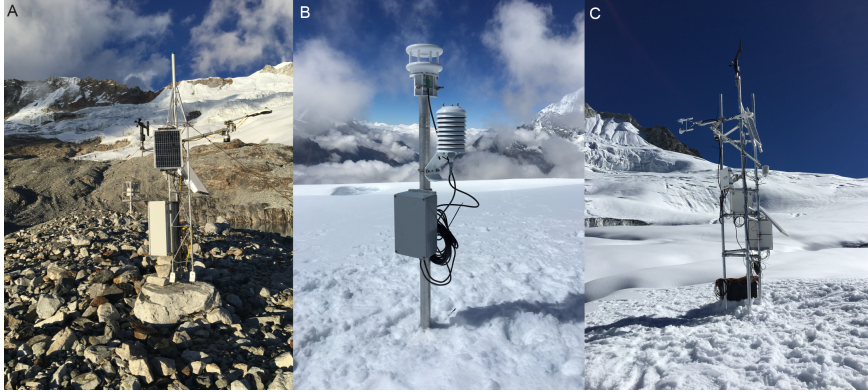


Figure 3.2: Pictures of (A) AWS Yala Base Camp, (B) micro-met station Yala Ridge, and (C) AWS Yala Glacier, including eddy covariance system (Photos: W. Immerzeel).

Table 3.1: Description of the meteorological stations.

Description	Code	Latitude	Longitude	Elevation (m a.s.l.)	Observations*
AWS Yala Base Camp	AWS Yala BC	28.23230	85.60967	5090	$T_a^{1.75}$, $RH^{1.75}$, $u^{2.5}$, $P^{1.75}$, $rad^{2.37}$
AWS Yala Glacier	AWS Yala Glacier	28.23463	85.61797	5350	$T_a^{2.2}$, $RH^{2.2}$, $u^{4.01}$, $EC^{3.3}$, $rad^{2.45}$, $SD^{2.45}$
Micro-Met Valley	MM Valley	28.22424	85.60724	4800	$T_a^{1.2}$, $RH^{1.2}$, $u^{1.5}$, $p^{1.5}$
Micro-Met Yala Low	MM Yala Low	28.23457	85.61608	5278	$T_a^{1.2}$, $RH^{1.2}$, $u^{1.5}$, $p^{1.5}$
Micro-Met Yala Ridge	MM Yala Ridge	28.23425	85.62512	5504	$T_a^{1.2}$, $RH^{1.2}$, $u^{1.5}$, $p^{1.5}$
Pluviometer Ganja La	Pluvio GL	28.1545	85.5625	4962	$T_a^{2.09}$, $prec^{1.55}$, $u^{4.46}$

* T_a , air temperature; RH , relative humidity; u , wind speed; P , atmospheric pressure; rad , incoming and outgoing shortwave and longwave radiation; EC , eddy covariance; SD , snow depth; $prec$, precipitation. Superscripts indicate the sensor height (m).

3.3.2 Derivation of sublimation rates from eddy covariance measurements

Post-processing of eddy covariance data is required to derive reliable turbulent fluxes (Reba et al., 2009). Uncertainties in the latent heat and sensible heat fluxes derived by the eddy covariance method over snow-covered surfaces have been estimated to vary between approximately 10 and 20% (Sexstone et al., 2016). In this study, post-processing was performed using the EddyPro software LI-COR (2016). This consisted of multiple steps. First, wind direction filtering was applied to exclude wind data from behind the eddy covariance system. Second, planar fit tilt ratioing (Wilczak et al., 2001), density correction (Webb et al., 1980), spike/count removal (Vickers and Mahrt, 1997), correction of low-pass filtering effects (Massman, 2000) and detrending using block averaging were applied to the data. Then, the quality of the data was checked based on criteria defined by Mauder and Foken (2004). These criteria test the assumption of stationarity, classifying data as high-quality, moderate-quality or low-quality data. Low-quality data (16%) were excluded from the calculation of the turbulent fluxes. A flux averaging interval of 10 min was chosen which met the stationarity criteria (Vickers and Mahrt, 1997). The 10-min turbulent fluxes were aggregated to hourly fluxes

to reduce flux sampling errors (Vickers and Mahrt, 1997). Finally, the hourly latent heat fluxes were converted to sublimation or evaporation using the latent heat of sublimation or latent heat of evaporation, respectively. The division between sublimation and evaporation was based on the surface temperature. It is assumed that sublimation occurs when the surface temperature is below 0 °C, whereas evaporation occurs when the surface temperature equals 0 °C. In addition, it is assumed that all sublimation and evaporation originates from a static surface. After installation of the eddy covariance system some snowmelt occurred in the afternoon, resulting in a compacted snow surface and unlikely conditions for blowing snow events.

Data gaps were not filled as the amount of missing data in the one-month time series was limited (2.5%). In addition, the few data gaps only occur during precipitation events when snow sublimation is assumed to be insignificant due to saturation of the air with water vapour.

3.3.3 Latent heat flux parameterizations

Existing parameterizations

Different methods are used to simulate the surface latent heat flux. Three existing parameterizations for latent heat flux were tested against the observed latent heat flux at AWS Yala Glacier. The tested parameterizations are the bulk-aerodynamic method, the Penman-Monteith equation, and an empirical relation developed by Kuchment and Gelfan (1996). These parameterizations were chosen as they have variable complexity and/or are commonly applied to calculate the surface latent heat fluxes. The energy fluxes were converted to mass fluxes using the latent heat of sublimation (2.838 MJ kg⁻¹) or latent heat of evaporation L (2.501 MJ kg⁻¹). Different statistical measures were calculated for the fit between hourly simulated and observed sublimation to assess the performance of the different parameterizations. These measures are bias, root mean square error, Nash-Sutcliffe efficiency and the correlation coefficient. The tested parameterizations are described below.

Kuchment and Gelfan (1996) empirical relation

The empirical relation developed by Kuchment and Gelfan (1996), and more recently adopted by Strasser et al. (2008), calculates the latent heat flux LE (W m⁻²) based on the wind speed u (m s⁻¹; usually at 2m level) and difference between the actual vapour pressure e_a (hPa) at measurement level and the water vapour saturation pressure at the snow surface e_{surf} (hPa), Equation 3.1:

$$LE = 32.82(0.18 + 0.098u)(e_a - e_{surf}) \quad (3.1)$$

The saturation vapour pressure e_{sat} (hPa) at the surface and at measurement level was calculated with Tetens (1930) relationship between air/surface temperature T_a/T_s (°C) and e_{sat} . The snow surface was assumed to be saturated whereas at the measurement level e_a was obtained from e_{sat} and the measured relative humidity RH (-). T_s was derived from observed outgoing longwave radiation and the Stefan-Boltzmann relationship, assuming an emissivity of 1.0 (Vionnet et al., 2012).

Penman-Monteith equation

The Penman-Monteith equation is commonly used to calculate evapotranspiration, but several studies have also applied this equation to estimate sublimation (Nakai et al., 1994; Mahrt and Vickers, 2005; Wimmer et al., 2009; Knowles et al., 2012). Equation 3.2 gives the Penman-Monteith equation:

$$LE = \frac{\Delta(R_n - G) + \frac{\rho_a c_p}{r_a}(e_{surf} - e_a)}{\Delta + \gamma(1 + \frac{r_s}{r_a})} \quad (3.2)$$

Where Δ (kPa °C⁻¹) is the gradient of the saturation vapour pressure curve, R_n (MJ) is the net radiation, G (MJ) is the ground heat flux, ρ_a (kg m⁻³) is the air density, c_p (MJ kg⁻¹) is the specific heat of dry air at constant pressure, γ (kPa °C⁻¹) is the psychrometric constant, and r_a and r_s (s m⁻¹) are the aerodynamic and surface resistance respectively. Mahrt and Vickers (2005) showed that G plays a minor role in explaining the variance in observed sublimation over a snow-covered surface. Therefore, G is assumed to be zero. r_s is also set to zero as the sublimation is calculated over a snow surface and there is no resistance imposed by leaf stomata. r_a was set to 400 s m⁻¹ and this value is discussed in Section 3.5.2.

Bulk-aerodynamic method

Previous comparisons of eddy covariance observed latent heat flux over snow covered surfaces with different parameterizations show that the bulk-aerodynamic method performs well (Reba et al., 2012; Sexstone et al., 2016). The bulk-aerodynamic method as adopted by Litt et al. (2015) was used here to estimate the turbulent fluxes. It consists of a set of four equations (Equations 3.3–3.6) that solve the Monin-Obukhov length L_* (m) with an iterative process:

$$LE = \rho_a L k^2 \frac{u(q_a - q_s)}{(\ln(\frac{z_v}{z_0}) - \psi_m(\frac{z_v}{L_*}))(\ln(\frac{z_q}{z_{q0}}) - \psi_q(\frac{z_q}{L_*}))} \quad (3.3)$$

$$H = \rho_a c_p k^2 \frac{u(T_a - T_s)}{(\ln(\frac{z_v}{z_0}) - \psi_m(\frac{z_v}{L_*}))(\ln(\frac{z_t}{z_{t0}}) - \psi_h(\frac{z_t}{L_*}))} \quad (3.4)$$

$$L_* = \frac{T_v u_*^3}{kg(\frac{H}{\rho_a c_p} + 0.61 LE)} \quad (3.5)$$

$$u_* = \frac{ku}{\ln(\frac{z_v}{z_0}) - \psi_m(\frac{z_v - z_0}{L_*})} \quad (3.6)$$

Where H (W m⁻²) is the sensible heat flux, u_* (m s⁻¹) is the friction velocity, k (0.4) is the von Karman constant, T_v (K) is the virtual air temperature, z_v , z_t and z_q (m) are the wind speed, temperature and humidity measurement levels respectively, q_s and q_a (kg kg⁻¹) are the specific humidity at the snow surface and measurement level respectively, and were calculated with observed temperature and relative humidity. z_0 , z_{t0} , z_{q0} (m) are the roughness lengths for momentum, sensible heat and humidity respectively. z_{t0} and z_{q0} are typically one or two orders of magnitude smaller than z_0 (Smeets et al., 1998; Cullen et al., 2007; Radic et al., 2017). The roughness lengths were used to optimise the fit between modelled and observed latent heat fluxes. z_t and z_q were forced to be one order of magnitude smaller than z_0 in the optimisation procedure. After optimisation, by minimising the root mean square error between simulated and observed sublimation, z_0 , z_t , and z_q were 0.013 m, 0.0013 m and 0.0013 m respectively. ψ_m , ψ_h , and ψ_q are stability corrections for momentum, heat and vapour transfer respectively. These stability corrections were defined according to Paulson (1970) and Webb (1970), Equations 3.7–3.10:

If $\frac{z}{L_*} < 0$:

$$\psi_m = 2 \ln\left(\frac{1+x}{2}\right) + \ln\left(\frac{1+x^2}{2}\right) - 2 \tan^{-1}(x) + \frac{\pi}{2} \quad (3.7)$$

$$\psi_h = \psi_q = 2 \ln\left(\frac{1+x^2}{2}\right) \quad (3.8)$$

If $0 < \frac{z}{L_*} < 1$:

$$\psi_m = \psi_h = \psi_q = -5 \frac{z}{L_*} \quad (3.9)$$

If $\frac{z}{L_*} > 1$:

$$\psi_m = \psi_h = \psi_q = -5 \left(\ln\left(\frac{z}{L_*}\right) + 1 \right) \quad (3.10)$$

Where x is defined as $x = (1-16 \frac{z}{L_*})^{\frac{1}{4}}$

Evaluation of meteorological drivers of sublimation

Before testing the different parameterizations described above, it was first assessed which meteorological variables are driving sublimation on Yala Glacier. Linear regressions and multiple linear regressions were applied to the eddy covariance derived sublimation and hourly observed meteorological variables measured at AWS Yala Glacier to determine which variables have the greatest influence on sublimation rates. To investigate whether on-glacier measurements are required to predict on-glacier sublimation, linear and multiple linear regressions were also applied to hourly meteorological data measured at the off-glacier AWS Yala Base Camp. Based on these assessments a relation was derived between sublimation and meteorological observations that drive the process. The relation was evaluated using the coefficient of determination (R^2) of the regressions. In addition, cross-validation was used to estimate the fit of the relation between sublimation and different meteorological variables. For the cross-validation, a single sublimation measurement was omitted before applying linear and multiple linear regressions to the data set with measurements of sublimation and meteorological variables. This procedure was repeated for all sublimation measurements.

3.3.4 Spatial and seasonal simulation of snow sublimation

The best performing sublimation parameterization was used to simulate the seasonal sublimation (15 October 2016–20 April 2017) at the location of the eddy covariance system. In addition, this parameterization was used to simulate the spatial distribution of sublimation over Yala Glacier for two characteristic days with low and high atmospheric humidity, i.e., 12 November 2016 and 1 January 2017, respectively. To simulate the spatial variability, distributed fields of meteorological variables are required. Surface observations and station elevations were used to estimate temperatures, which can be reliably extrapolated using observed temperature lapse rates (Immerzeel et al., 2014). Other meteorological variables were estimated using high-resolution WRF simulations for two characteristic days.

Daily temperature lapse rates were derived from linear regression through air temperature observations at the two AWSs and the three micro-met stations. Air temperature was extrapolated from AWS Yala Glacier to the entire glacier using an 8-m digital elevation model (Noh and Howat, 2015) and the derived temperature lapse rates. Consequently, the simulations of sublimation have a spatial resolution of 8 m.

The spatial distributions of wind speed, humidity and surface temperature were based on WRF simulations. Collier and Immerzeel (2015) successfully applied WRF over complex terrain and simulated the spatial distribution of precipitation in the Langtang catchment in Nepal. Rai et al. (2017) used WRF in a large-eddy-simulation-mode to simulate turbulence

over complex terrain at very high spatial resolution (30 m), showing good agreement with observations. For this study WRF settings were largely based on the settings adopted by Collier and Immerzeel (2015). WRF was used in large-eddy-simulation mode and nested in a larger domain to enable high-resolution simulations (30 m) for Yala Glacier. The WRF fields were downscaled to 8-m resolution using the cubic spline interpolation method. Details of the WRF configurations are given in Appendix A. It was computationally not feasible to run WRF for the entire winter period. Hence, WRF was run for two characteristic days; i) clear sky, low atmospheric humidity and ii) cloudy, high atmospheric humidity. The threshold for a humid or non-humid day was set to 60%. 12 November 2016 and 1 January 2017 were chosen as two representative days for a non-humid and humid day, respectively. The hourly spatial patterns for both days were then scaled with meteorological observations from the three on-glacier stations. Hourly ratios were calculated between field observations and the WRF meteorological fields at the location of the three on-glacier meteorological stations. The average ratio was used to scale the WRF meteorological fields. Surface temperature is however only measured at one location on the glacier, and spatial patterns of surface temperature were therefore scaled based on a single observation.

3.4 Results

3.4.1 Observed surface energy balance, meteorology and sublimation

At AWS Yala Glacier, all radiation components and turbulent fluxes were measured from 15 October to 17 November 2016 (Figure 3.3). This period consists mainly of clear-sky days with a strong diurnal pattern of incoming and outgoing shortwave radiation. A diurnal pattern was also observed for the outgoing longwave radiation due to warming and cooling of the snowpack during day and night. Incoming longwave radiation is higher during the first 5 days compared to the complete time series, which is caused by the high humidity of the atmosphere. On these humid days, the latent heat flux is approximately zero, whereas the latent heat flux on dry days shows a clear diurnal cycle with a peak in the early afternoon (Figure 3.3). Both the sensible and latent heat fluxes are smaller than the radiation components, with daily average values of 5.5 and -31.6 W m^{-2} respectively. The surface energy balance is positive on every day of the time series (Figure 3.3).

For the 32-day period, the observed cumulative loss of water due to sublimation is 31.6 mm, whereas deposition during the nights is negligible (1.3 mm). The sublimation rate is approximately zero on the first 5 days of the time series, whereas daily cumulative sublimation varies between approximately 1.0 and 1.5 mm day^{-1} on days with a clear diurnal cycle. On days with low atmospheric humidity the daily maximum sublimation rate varies between 0.1 and 0.27 mm h^{-1} . Figure 3.4 shows the observed sublimation rate, wind speed and actual vapour pressure for characteristic humid and non-humid days, which illustrates that higher sublimation rates coincide with higher wind speeds and that high near surface vapour pressure constrains sublimation.

Figure 3.5 shows the meteorology observed at AWS Yala Glacier for the 2016–2017 winter season. The monthly mean air temperature decreases from October to January with lowest observed temperatures ($-13.8 \text{ }^\circ\text{C}$) in January. In spring the air temperature increases again. The monthly mean wind speeds show no considerable change throughout the winter period. The monthly mean relative humidity is lowest in November and December, whereas it is approximately 60% in October and April.

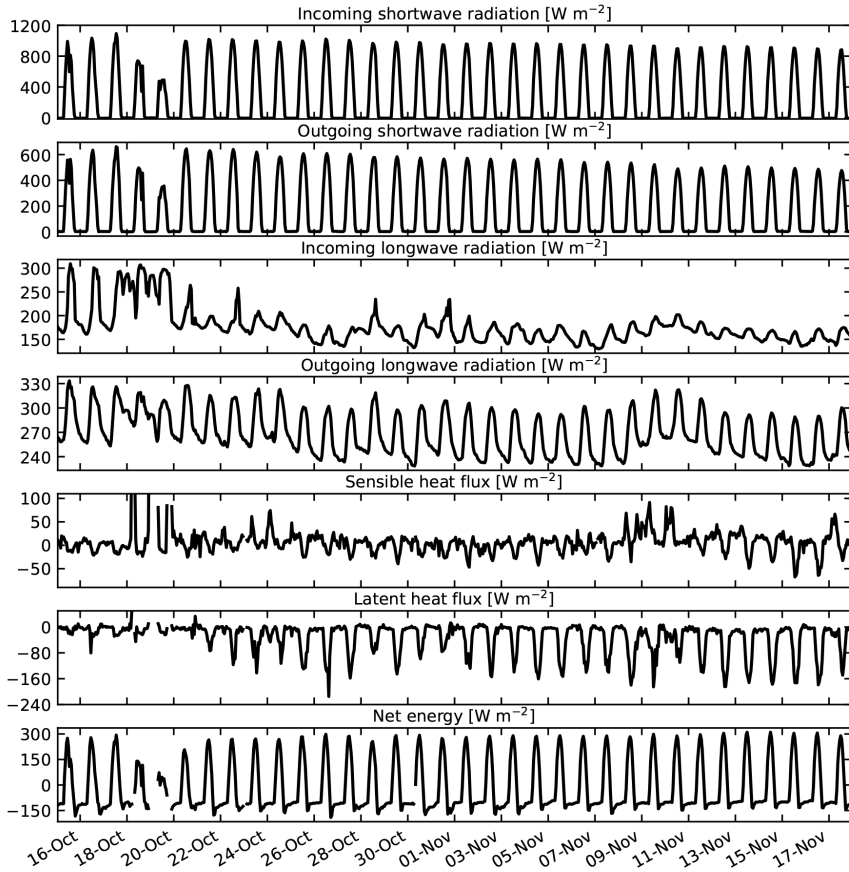


Figure 3.3: Time series of observed turbulent fluxes and radiation components at AWS Yala Glacier. The turbulent fluxes are positive for fluxes pointing from the atmosphere to the snow surface and negative for fluxes pointing from the surface to the atmosphere.

Latent heat flux parameterizations and the importance of different meteorological variables

To examine the influence of meteorological variables on sublimation rates we first excluded nighttime observations (when sublimation and deposition are negligible) and periods where the surface temperature equals 0 °C. Air temperature and surface temperature do not show a clear relation with the sublimation rate (Figure 3.6). At low air temperatures the sublimation rate is almost equal to zero while for higher air temperatures the range of sublimation rates increases. This is likely related to low wind speeds coinciding with low temperatures (Figure 3.6). Net radiation does not show a strong relation with the sublimation rate. However, when net radiation becomes negative (late afternoon until early morning), sublimation rates are reduced. Relative humidity shows two clusters related to sublimation rate: near-saturation conditions ($RH > 90\%$) have very low sublimation rates, but at lower values of RH there is a weakly positive relation between RH and sublimation rate. Vapour pressure deficit (D ; kPa) and wind speed both show clear positive relations with sublimation rate. The vapour pressure deficit is defined as the difference between e_a at measurement level and e_{surf} .

Results of the linear and multiple linear regressions show that wind speed and vapour pres-

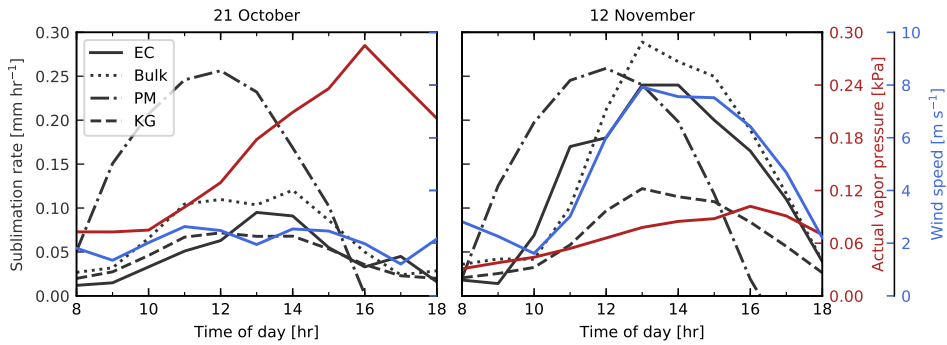


Figure 3.4: Observed and simulated sublimation rate (black), wind speed (blue), and actual vapour pressure (red) at AWS Yala Glacier for 21 October and 12 November 2016 with relatively low ($<1.0 \text{ mm day}^{-1}$) and high sublimation rates ($>1.0 \text{ mm day}^{-1}$). EC refers to the eddy covariance measurements. Bulk, PM and KG refer to the simulated sublimation with the bulk-aerodynamic method, Penman-Monteith equation and Kuchment and Gelfan (1996) empirical relation, respectively.

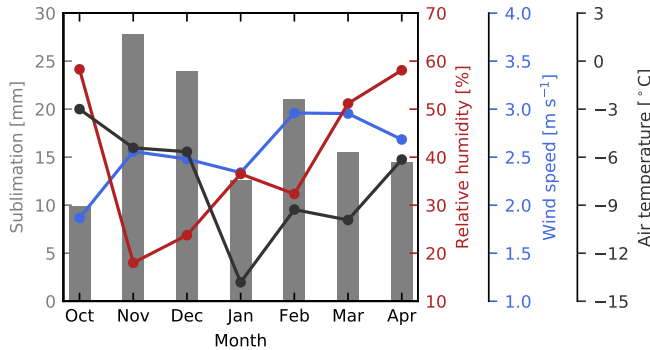


Figure 3.5: Monthly values of air temperature, relative humidity and wind speed observed at AWS Yala Glacier for the 2016–2017 winter season. The bars indicate the monthly cumulative sublimation simulated with the bulk-aerodynamic for 15 October 2016–20 April 2017.

sure deficit are the best sublimation predictors (Table 3.2). Linear regressions through wind speed and vapour pressure deficit explain 54 and 48% of the total variance in sublimation, respectively, based on on-glacier observations. 61 and 38% of the total variance is explained by off-glacier wind speed and vapour pressure deficit observations. In general, sublimation is better predicted by meteorological variables measured on-glacier than off-glacier, but differences are small (Table 3.2). The combination of wind speed, vapour pressure deficit and air temperature yields the highest coefficient of determination for the regression and cross-validation based on on-glacier meteorological data and explains 80% of the total variance in sublimation.

The three parameterizations were used to calculate sublimation at the location of the eddy covariance tower using on-glacier AWS data (Figure 3.7). There is considerable variation between the performance of the different parameterizations. The Penman-Monteith parameterization gives a strong diurnal cycle of sublimation for each day, but does not capture the low sublimation rates during the first days of the time series when relative humidity is high

(Figure 3.4). In addition, the observed diurnal peak in sublimation rate for the Penman-Monteith parameterization is consistently too early. In contrast to this parameterization the empirical relation of Kuchment and Gelfan (1996) results in a correct timing of peak sublimation (Figure 3.4). However, sublimation is strongly underestimated (Figure 3.7). The bulk-aerodynamic method offers an improved estimate of sublimation, but still slightly underestimates hourly rates and sublimation totals. The calculated cumulative sublimation is 16.4, 43.0, and 28.6 mm by the Kuchment and Gelfan (1996) empirical relation, Penman-Monteith parameterization and the bulk-aerodynamic method, respectively for the time period 15 October–17 November. For this period the observed cumulative sublimation is 32 mm.

Different statistical measures were calculated for the fit between simulated and observed sublimation to assess the performance of the different parameterizations (Figure 3.7). The bulk-aerodynamic method has the lowest bias ($-0.0034 \text{ mm h}^{-1}$), lowest root mean square error (0.033 mm h^{-1}) and highest Nash-Sutcliffe efficiency (0.76). Therefore, this parameterization was used to simulate spatially distributed sublimation on Yala Glacier.

To study the model performance in more detail, sublimation residuals for the bulk-aerodynamic method were evaluated. The residuals show no relationship with wind speed, vapour pressure deficit and air temperature (Figure 3.8). However, the bulk-aerodynamic method overestimates sublimation rates in the morning, whereas it slightly underestimates sublimation in the afternoon (Figure 3.8).

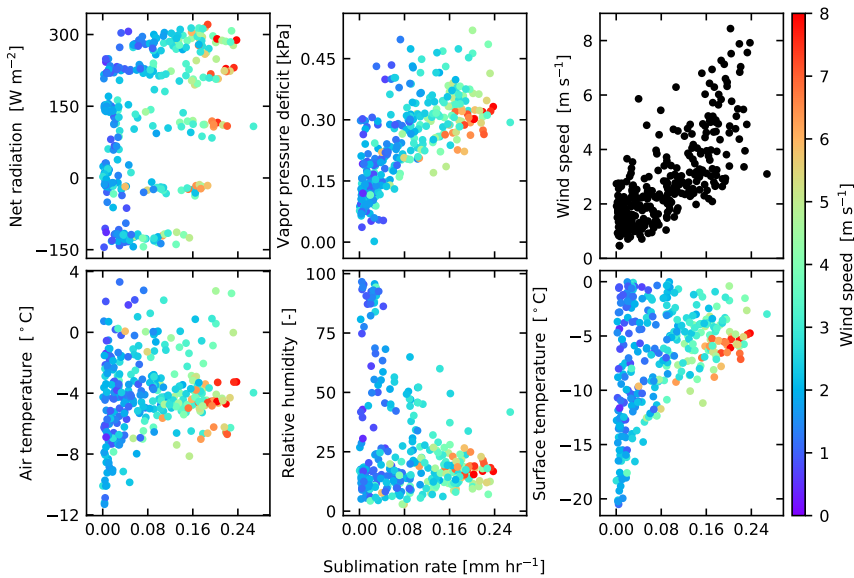


Figure 3.6: Scatter plots of meteorological variables against sublimation rate, observed at AWS Yala Glacier. The colour of the data points refers to the observed wind speed.

Spatial distribution of sublimation and seasonal estimations of sublimation at the location of the eddy covariance system

Spatial fields of wind speed, actual vapour pressure, surface temperature and air temperature are required for the spatial simulation of sublimation. Figure 3.9 shows the daily average meteorological fields for the humid and non-humid day. The spatial fields for the humid and

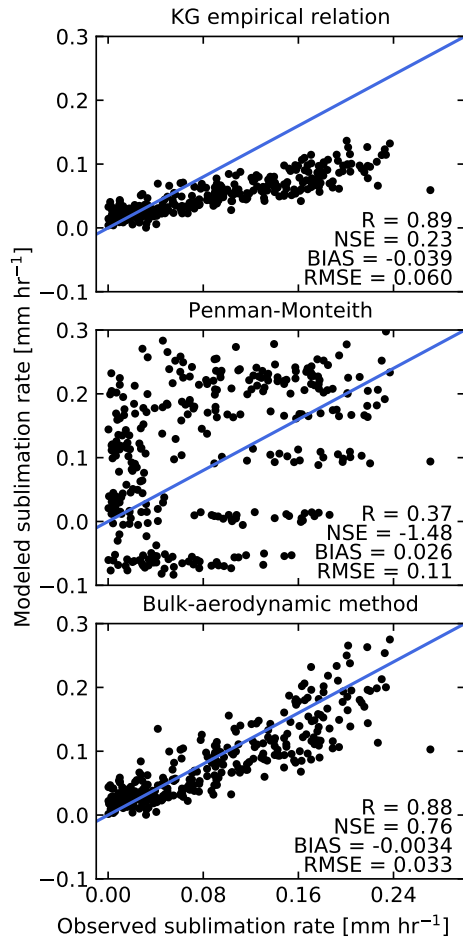


Figure 3.7: Scatter plots of observed and simulated sublimation for different parameterizations. R , NSE , $BIAS$, and $RMSE$ refer to the correlation coefficient, Nash-Sutcliffe efficiency, bias and root mean square error, respectively.

non-humid day show both highest wind speeds close to the ridge (Figure 3.9). On both days the wind speed increases with increasing altitude and the wind speed is relatively higher at the northeastern side of the glacier. The actual vapour pressure and surface temperature also show decreasing patterns with increasing elevations (Figure 3.9). The wind speed and surface temperature are lower on the humid day compared to the non-humid day, whereas the actual vapour pressure is higher. The hourly WRF fields were scaled with hourly meteorological observations at the three on-glacier stations for the sublimation simulations with the bulk-aerodynamic method. The average scaling factor for both days is 1.87 and 1.28 for the wind speed and actual vapour pressure, respectively. The surface temperature is on average corrected with 1.53 °C. Simulated over the entire glacier, cumulative daily sublimation varies between 0.0 and 1.2 mm for the humid and non-humid day, with higher sublimation totals at higher elevations (Figure 3.9). Cumulative sublimation is highest near the ridge, where the greatest wind speeds occur.

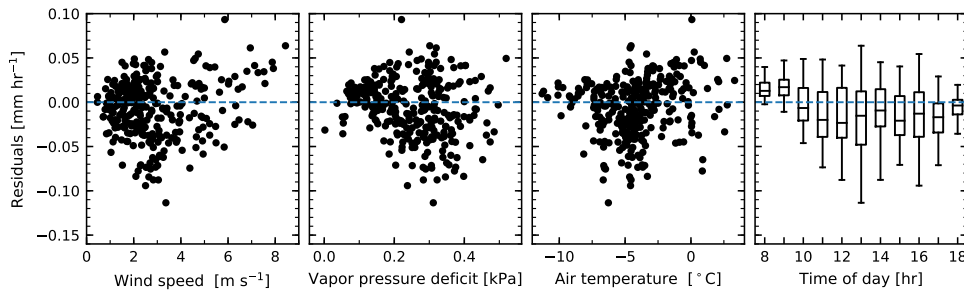


Figure 3.8: Sublimation residuals (observed-modelled) for the bulk-aerodynamic method against observed wind speed, vapour pressure deficit, air temperature and time of day.

The simulated cumulative sublimation and evaporation at AWS Yala Glacier are 125 and 9 mm, respectively for 15 October 2016–20 April 2017. Figure 3.5 shows the simulated monthly sublimation with the bulk-aerodynamic method for the 2016–2017 winter season. The cumulative sublimation is highest in the months November (27.8 mm) and December (24.0 mm), whereas January has relatively low cumulative sublimation (12.6 mm). The monitored cumulative snowfall is 484 mm at pluviometer Ganja La, located 9 km south of Yala Glacier at an elevation of 4962 m a.s.l., between 1 October 2016 and 1 September 2017. The precipitation measurements were corrected for undercatch, according to Wolff et al. (2015). The snowfall at AWS Yala Glacier was derived from Ganja La precipitation and the observed air temperature at AWS Yala Glacier to distinguish between snowfall and rainfall. This method resulted in 634 mm snowfall at the location of AWS Yala Glacier. The fraction of snowfall returned to the atmosphere due to sublimation and evaporation is 21%.

3.5 Discussion

3.5.1 Observed surface energy balance and sublimation

The observed surface energy balance at AWS Yala Glacier is positive on each day of the time series. Theoretically, this surplus in energy would result in snowmelt. A simple calculation reveals that the surplus energy results in approximately 505 mm (w.e.) snowmelt over the measurement period. However, based on observed changes in snow surface height at AWS Yala Glacier (-0.20 m) and an assumed snow density of 350 kg m^{-3} , the actual melt is estimated to be approximately 70 mm. This discrepancy is likely explained by pressure melting causing sinking of the tower into the ice which reduces measured surface lowering, even though we attempted to eliminate sinking by capping the ends of the tower. Assuming that sinking did not occur, the overestimation of the snowmelt could potentially be explained by several other factors. In the melt estimate based on the surface energy balance it is assumed that all meltwater drains the snowpack while it may be retained and potentially refreezes within the snowpack. Melt of the refrozen meltwater requires additional energy and may explain part of the energy surplus. Other explanations can be the cold content of the snowpack and the heat flux from the snowpack into the glacier ice or vice versa, but these processes can only partly explain the energy surplus. Besides the process-based explanations, measurement errors could explain a part of the energy surplus. We observed condensation in the downward-looking radiation sensor that potentially results in underestimation of the outgo-

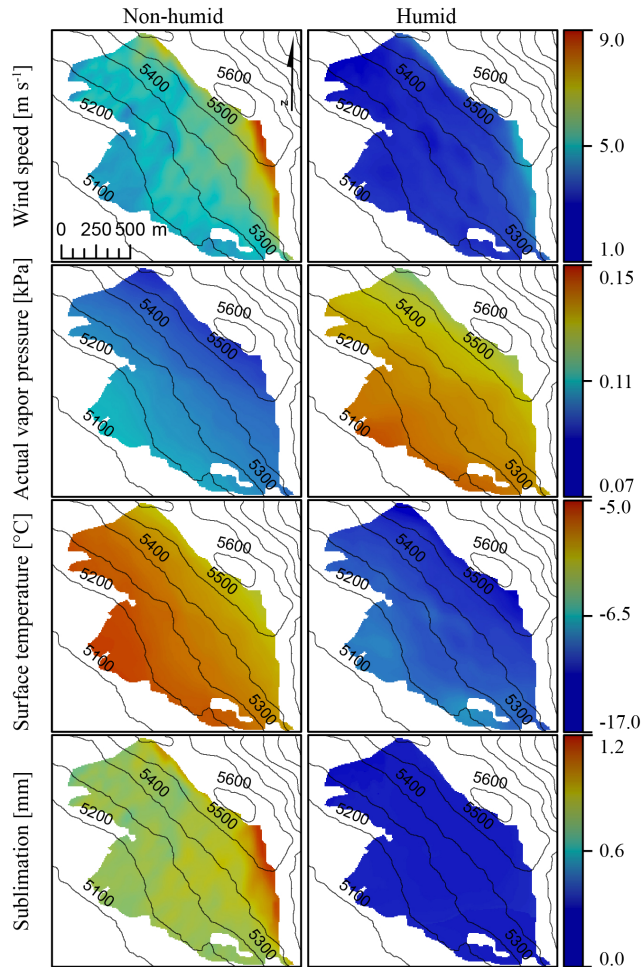


Figure 3.9: Daily cumulative sublimation, simulated with the bulk-aerodynamic method, and daily average WRF fields of (10 m) wind speed, (2 m) actual vapour pressure and surface temperature for a humid day (1 January 2017) and a non-humid day (12 November 2016) at Yala Glacier. The black lines represent the elevation contour lines.

ing shortwave radiation. Moreover, the derived turbulent fluxes are also uncertain and that could influence the energy balance closure as well. These uncertainties of turbulent fluxes have previously been quantified to be approximately 10–20% over snow covered surfaces (Sexstone et al., 2016).

Sublimation rates peak in early afternoon (Figure 3.3), which coincides with findings of Reba et al. (2012) and Sexstone et al. (2016), and they also increase with increasing wind speed (Figure 3.6). Positive net radiation in the daytime results in an increase in the turbulence in the surface boundary layer (Wagnon et al., 2003), and higher sublimation rates. However, sublimation is strongly reduced on days where atmospheric humidity is high. High humidity prohibits sublimation as the atmosphere is saturated and near-surface water vapour pressure gradients are weak. On days with low atmospheric humidity, wind speeds tend to be

higher. Higher wind speeds result in a well-mixed layer above the snow surface and sustained vapour pressure gradients that support sublimation. The primary driver for sublimation is the shortwave radiation and soon after the glacier is sunlit the sublimation increases, conditioned by an initial vapour pressure deficit. Once the wind speeds increase the sublimation is further enhanced and both sublimation and wind peak around 13 h in the afternoon.

The observed average daily sublimation rate (1.0 mm day^{-1}) and the maximum hourly sublimation rate (0.27 mm h^{-1}) are high compared to other studies that measured sublimation with an eddy covariance system. Reba et al. (2012) observed sublimation rates ranging from 0.37 to 0.53 mm day^{-1} and from 0.17 to 0.28 mm day^{-1} for an exposed and sheltered site, respectively in the Owyhee Mountains, USA. Sublimation rates of 0.05 – 0.23 mm day^{-1} were observed by Stössel et al. (2010) in the Swiss Alps. In the Sierra Nevada, Spain, maximum sublimation rates of 0.11 mm h^{-1} were observed (Herrero and Polo, 2016). Sextstone et al. (2016) observed a mean sublimation rate of 0.33 – 0.36 mm day^{-1} in the Colorado Rocky Mountains, USA. However, Cullen et al. (2007) observed high sublimation rates of 1.4 mm day^{-1} on the top of Kilimanjaro (5794 m a.s.l.), Tanzania, for a 2-day measurement campaign. Also, high sublimation rates have been observed in the Andes at high altitude. Wagnon et al. (2003) observed sublimation rates ranging between 0.7 and 1.2 mm day^{-1} during multiple days in the winter in 1999, 2001, and 2002 with a sublimation pan at 6340 m a.s.l. Litt et al. (2015) observed a latent heat flux of -34 W m^{-2} for a 42-day period on a tropical glacier in Bolivia at 5080 m a.s.l. , which is comparable to what we observed at Yala Glacier (-31.6 W m^{-2}). The favorable climate conditions at high altitude, i.e., low atmospheric pressure, high wind speed and low near-surface vapour pressures support the higher observed sublimation rates in our study and the studies of Cullen et al. (2007), Litt et al. (2015), and Wagnon et al. (2003).

3.5.2 Performance of the parameterizations

The bulk-aerodynamic method underestimates the latent heat flux in this study (Figure 3.7), whereas Fitzpatrick et al. (2017) and Radic et al. (2017) showed overestimation of turbulent fluxes with the bulk-aerodynamic method, as the assumptions of the Monin-Obukhov similarity theory may be not valid for a strongly stable atmosphere during katabatic flow (Fitzpatrick et al., 2017). Radic et al. (2017) showed that a combination of a bulk-aerodynamic method with a katabatic model yielded the best results on a temperate glacier in mountain BC, Canada. However, katabatic flow occurs mainly during night on Yala Glacier, which is excluded from the analysis as sublimation is negligible. Therefore, we excluded the method of Radic et al. (2017) from our study and we assumed that the Monin-Obukhov theory is valid for our specific application. The tuned roughness values ($z_0=0.013 \text{ m}$, $z_t=0.0013 \text{ m}$, and $z_q=0.0013 \text{ m}$) are relatively high, but are within the range that has been reported in literature for snow surfaces (Brock et al., 2006; Cullen et al., 2007; Radic et al., 2017). The residuals for the bulk-aerodynamic method show no relation with meteorological variables (Figure 3.8), but only show a relation with the time of day. In the early morning the sublimation is overestimated, whereas in the afternoon it is underestimated. The overestimation in the morning could be explained by stable atmospheric conditions which occur in the early morning. Simulated heat fluxes with the bulk-aerodynamic method are in general sensitive to the chosen stability corrections and these corrections may lead to additional errors compared to eddy covariance observations (Schlögl et al., 2017).

The discrepancies between observed and modelled peak sublimation by the Penman-Monteith equation are explained by high-altitude conditions. This equation is driven by two terms, i.e., the net radiation and vapour pressure deficit. The net radiation typically peaks earlier than the sublimation rate, indicating that the Penman-Monteith equation is stronger driven by the

net radiation than the vapour pressure deficit. This a direct result of the air density which is approximately half of the air density at this altitude compared to sea level. The air density is a factor multiplied with the vapour pressure deficit, reducing the weight of this term for calculation of sublimation. The net radiation is negative during the late afternoon, which results in deposition instead of sublimation and, therefore, we omitted these values in Figure 3.7. The low performance may also be partly explained by the uncertainties regarding the observed net radiation (Section 3.4.1) as it is strongly driven by this variable. The aerodynamic resistance (r_a) in the Penman- Monteith equation was used for calibration. Values of r_a for sublimation of snow strongly vary in literature and relations between wind speed and r_a have been used to estimate r_a over a snow surface (Nakai et al., 1994; Wimmer et al., 2009; Knowles et al., 2012). However, all these relations gave no satisfactory results. Nakai et al. (1994) inversed the Penman- Monteith equation to derive r_a from measured sublimation and wind speed. A similar approach was tested, but no relation was found between r_a and wind speed. Finally, a constant r_a of 400 s m^{-1} gave the best results, after minimisation of the root mean square error between observed and predicted sublimation.

The Kuchment and Gelfan (1996) empirical relation strongly underestimates the sublimation, which indicates that this empirical relation is not transferrable between regions. The use of an empirical relation is often region-specific or even glacier specific due to different climate and topographical conditions in other geographic regions and glaciers. However, linear regressions and multiple linear regressions show that sublimation at AWS Yala Glacier can be predicted with reasonable accuracy by wind speed and vapour pressure deficit (Table 3.2). Interestingly, off-glacier meteorological data has almost equal predicting capabilities as on-glacier data. This shows that off-glacier stations may be used to predict sublimation/latent heat fluxes on-glacier, which is valuable as AWSs are generally positioned off-glacier.

3.5.3 Spatial distribution of sublimation and seasonal sublimation at the location of the eddy covariance system

Spatially distributed sublimation is strongly related to variations of wind speed in space (Figure 3.9). Close to the ridge, wind speed is typically high (Figure 3.9), resulting in high daily sublimation totals. This illustrates a high spatial variability of sublimation on Yala Glacier. The humid day shows lower sublimation totals than the non-humid day as high humidity leads to smaller near-surface vapour pressure gradients, resulting in lower sublimation rates. The surface temperature is lower on the humid day compared to the non-humid day (Figure 3.9). On high-humidity days the observed net radiation is lower than on low-humidity days, resulting in less warming of the snow surface. On high humidity days cloud cover is often present, which reduces the incoming shortwave radiation and therefore reduces the net shortwave radiation. Although the net longwave radiation is larger on humid days, the shortwave radiation dominates the net radiation, leading to less warming of the surface and consequently colder snow surfaces on high-humidity days. This occurs regularly on Yala Glacier on the humid days and reduces near-surface vapour pressure gradients.

The sublimation totals may differ considerably when extrapolated to the whole winter season, and the quality of the sublimation estimates is largely dependent on the quality of the WRF fields (see Appendix A). For example, wind speeds are typically overestimated over crests using atmospheric modelling at very high resolution (e.g. Mott and Lehning, 2010; Vionnet et al., 2017). This could lead to overestimation of our sublimation totals close to the ridge. The used scaling method, in which an average scaling factor is calculated between the WRF fields and the in situ observations, does not take into account the complex and potential non-linearity of the system, which may increase the uncertainty.

The monthly cumulative sublimation shows large temporal variation (Figure 3.5). The

monthly sublimation is highest in October and December when the relative humidity is lowest. Dry air enhances sublimation as it results in a steep near-surface vapour pressure gradient. Contrastingly, in January the monthly sublimation is relatively low when the relative humidity is also low. This is likely explained by the coldest surface temperatures in January compared to the other months. Cold surface temperatures lead to lower saturation vapour pressure at the surface, reducing the near-surface vapour pressure gradient and therefore sublimation.

The fraction of snowfall returned to the atmosphere due to sublimation and evaporation (21%) at the location of AWS Yala Glacier is substantial. The sublimation at the location of AWS Yala Glacier equals the simulated sublimation averaged over the entire glacier. This indicates that the seasonal estimates of sublimation at AWS Yala Glacier may be representative for Yala Glacier. The simulated sublimation fields show high spatial variability, where sublimation totals are approximately a factor 1.7 higher close to the ridge of Yala Glacier and a factor 0.8 smaller at the lower part of Yala Glacier compared to the location of AWS Yala Glacier. This illustrates that the fractions of snowfall returned to the atmosphere may have high spatial variability as well. It is likely that the fraction is higher at more wind-exposed locations, such as the ridge. However, the cumulative winter snowfall has uncertainties that are related to i) undercatch of snowfall by the pluviometer, ii) the actual snow-rain-point, and iii) spatial variability in precipitation. Collier and Immerzeel (2015) showed with WRF simulations that, at the location of the pluviometer used in this study, the snowfall is 1.5 times more than at Yala Glacier. This would indicate even higher importance of sublimation to the water balance. Even though cumulative winter snowfall is uncertain, our results show that sublimation (and evaporation) is a significant component of the water balance. Therefore, it is crucial to include this component in future hydrological and mass balance studies. Studies should be performed to estimate the importance of high-altitude sublimation at both catchment and regional scales. The bulk-aerodynamic method can for example be implemented in existing hydrological models and applied on a larger scale, either forced by WRF simulations, a meteorological monitoring network, or a combination of both.

This study quantifies only surface snow sublimation while blowing snow sublimation may also play an important role. A wide variation of blowing snow sublimation rates have been reported in literature. This variety is a result of different climate regions and blowing snow model setup (Groot Zwaaftink et al., 2013). For example, it has been reported that the sublimation of suspended particles is several factors higher than surface sublimation, as there is more ventilation and supply of dry air (Strasser et al., 2008; MacDonald et al., 2010; Vionnet et al., 2014). However, most models do not include temperature and humidity feedbacks and therefore lack the self-limiting process of blowing snow sublimation (Groot Zwaaftink et al., 2011; Vionnet et al., 2014). Simulating blowing snow sublimation is beyond the scope of this study and might have resulted in an underestimation of the sublimation in this study. Therefore, future research should focus on quantifying the occurrence of blowing snow events and corresponding sublimation rates in the Himalaya.

3.6 Conclusions

An eddy covariance experiment was conducted to measure snow sublimation on Yala Glacier at an altitude of 5350 m a.s.l. The eddy covariance measurements show that the cumulative sublimation is 32 mm for a 32-day period. The average sublimation rate of 1.0 mm per day is relatively high and can be explained by favorable conditions at high altitude, i.e., low atmospheric pressure, high wind speed and low near-surface vapour pressures. The performance of parameterizations of different complexity (i.e., Penman-Monteith equation,

bulk-aerodynamic method and an empirical relation) were tested against the measurements. The bulk-aerodynamic method outperformed the other parameterizations and was used to simulate sublimation at the location of the eddy covariance system from 15 October 2016 to 20 April 2017. The simulated cumulative sublimation and evaporation are 125 and 9 mm, respectively, which is 21% of the annual snowfall. Furthermore, the spatial variability of sublimation was simulated with the bulk-aerodynamic method for a humid and non-humid day. Required meteorological field were obtained from WRF simulations and field observations. The sublimation at the location of the eddy covariance system equals the simulated sublimation averaged over the entire glacier and is therefore representative for the seasonal sublimation on Yala Glacier. The spatial patterns of sublimation are strongly linked to the modelled wind speed patterns. The sublimation totals on the non-humid day are a factor 1.7 higher close to the ridge and a factor 0.8 lower at the lower part of Yala Glacier compared to the location of the eddy covariance system. This illustrates that the fraction of snowfall returned to the atmosphere due to sublimation may be much higher close to the ridge that is more wind exposed. This study quantifies surface sublimation only and future research should focus on including the sublimation of blowing snow as this may increase the sublimation estimate. We conclude that sublimation is an important component of the water balance and glacier mass balance; future hydrological and mass balance studies in the Himalaya can no longer ignore this component.

3.7 Acknowledgements

We are grateful to the Norwegian Water Resources and Energy Directorate (NVE) for providing the Ganja La precipitation data. We thank the four reviewers for their constructive comments that helped improving the manuscript. This project was supported by funding from the European Research Council (ERC) under the European Unions Horizon 2020 research and innovation program (grant agreement no. 676819) and by the research programme VIDI with project number 016.161.308 financed by the Netherlands Organization for Scientific Research (NWO). This study was also supported through the core funds of the International Center for Integrated Mountain Development (ICIMOD; contributed by the governments of Afghanistan, Australia, Austria, Bangladesh, Bhutan, China, India, Myanmar, Nepal, Norway, Pakistan, Switzerland and the United Kingdom). The views and interpretations in this publication are those of the authors and are not necessarily attributable to ICIMOD.

Chapter 4

Energy and mass balance dynamics of the seasonal snowpack at two high-altitude sites in the Himalaya

Snow dynamics play a crucial role in the hydrology of alpine catchments in the Himalaya. However, studies based on in-situ observations that elucidate the energy and mass balance of the snowpack at high altitude in this region are scarce. In this study, we use meteorological and snow observations at two high-altitude sites in the Nepalese Himalaya to quantify the mass and energy balance of the seasonal snowpack. Using a data driven experimental set-up we aim to understand the main meteorological drivers of snowmelt, illustrate the importance of accounting for the cold content dynamics of the snowpack, and gain insight into the role that snow meltwater refreezing plays in the energy and mass balance of the snowpack. Our results show an intricate relation between the sensitivity of melt and refreezing on the albedo, the importance of meltwater refreezing, and the amount of positive net energy used to overcome the cold content of the snowpack. The net energy available at both sites is primarily driven by the net shortwave radiation, and is therefore extremely sensitive to snow albedo measurements. We conclude that, based on observed snowpack temperatures, 21% of the net positive energy is used to overcome the cold content build up during the night. We also show that at least 32–34% of the snow meltwater refreezes again for both sites. Even when the cold content and refreezing are accounted for, excess energy is available beyond what is needed to melt the snowpack. We hypothesize that this excess energy may be explained by uncertainties in the measurement of shortwave radiation, an underestimation of refreezing due to a basal ice layer, a cold content increase due to fresh snowfall and the ground heat flux. Our study shows that in order to accurately simulate the mass balance of seasonal snowpacks in Himalayan catchments, simple temperature index models do not suffice and refreezing and the cold content needs to be accounted for.

Based on: Stigter, E. E., Steiner, J. F., Koch, I., Saloranta, T. M., Kirkham, J. D., and Immerzeel, W. W. (2021), Energy and mass balance dynamics of the seasonal snowpack at two high-altitude sites in the Himalaya, *Cold Regions Science and Technology* 183, doi: 10.1016/j.coldregions.2021.103233

4.1 Introduction

Snow in alpine catchments is a seasonal water storage that strongly influences catchment hydrology. The quantification of the timing and volume of snow meltwater is essential for irrigation, hydropower and flood and drought risk assessment. Snowpack dynamics in the Himalaya have been scarcely studied based on in situ observations (Kirkham et al., 2019). Typically, snow studies in this region rely heavily on satellite remote sensing, modelling, or a combination of both (e.g. Bookhagen and Burbank, 2010; Immerzeel et al., 2009; Lievens et al., 2019; Smith et al., 2017; Smith and Bookhagen, 2018). Remote sensing products provide mainly information on snow cover, but do not provide information about the energy and mass balance of the snowpack. Recent progress has been made in improving the vertical resolution of remotely sensed snow products. Smith and Bookhagen (2018) developed a remotely sensed snow water equivalent (SWE) product from passive microwave data from 1987 until 2009. However, its absolute SWE values are unreliable and hence only relative changes have been investigated to study trends on the scale of High Mountain Asia (Smith and Bookhagen, 2018). In addition, the coarse spatial resolution of this product fails to capture the high heterogeneity of snow processes and properties. Another study by Lievens et al. (2019) derived snow depth at a relatively high spatial resolution (1 km²) from Sentinel-1 satellite data for all mountain ranges in the Northern Hemisphere. Even though this new product is promising to study snow depth variability, the scarcity of validation sites in the Himalaya precludes proper evaluation of this product in this region (Lievens et al., 2019). Besides remotely sensed snow products, models are used to understand the energy and mass balance of a snowpack. Snowmelt simulations can be performed with models of different complexity. In Himalayan snow studies, where data availability is low, the simple degree-day method and the Enhanced-Temperature Index (ETI) method are primarily used (Bookhagen and Burbank, 2010; Ragetli et al., 2015; Saloranta et al., 2019; Stigter et al., 2017). In contrast, physically-based snow models that include a full energy balance approach (e.g. Bartelt and Lehning, 2002; Vionnet et al., 2012) are more complex and have higher data requirements, which are often not available in a Himalayan context (c.f. Bolch et al., 2019). However, simplistic snowmelt models generally do not account for snow processes, such as refreezing, sublimation and wind redistribution, that can be important at high altitude, where snow ablation is not necessarily dominated by melt (Litt et al., 2019; Stigter et al., 2018). Another limitation of these models is that they simulate snowmelt runoff as soon as temperatures rise above the threshold temperature for melt onset. However, melting of a snowpack consists of three phases: i) the warming phase in which absorbed energy raises the average snowpack temperature to an isothermal temperature of 0 °C, ii) the ripening phase in which snow melts but the meltwater is retained within the snowpack in the pore spaces, and iii) the output phase when snowmelt drains from the snowpack as result of additional absorbed energy (Dingman, 2008). These phases alternate at both seasonal and daily time scales as a result of periods with repeated negative net energy, which leads to the cooling of the snowpack and refreezing of meltwater retained within the snowpack. These may be important processes as this potentially leads to the same snow being warmed and melted multiple times before the end of the snow season, resulting in a delay in snowmelt onset and runoff (e.g. Bengtsson, 1982a; Bengtsson, 1982b; Jennings et al., 2018; Pfeffer et al., 1991; Pfeffer and Humphrey, 1998). Several studies have shown that sub-daily runoff simulations are improved by using an energy balance approach instead of the degree-day method in alpine terrain as the more sophisticated energy balance approach accounts for the different phases of snowmelt (Avanzi et al., 2016; Förster et al., 2014; Warscher et al., 2013). Refreezing of snow meltwater, retained within the snowpack, can have a considerable effect on the energy and mass balance of a snowpack. Although re-

freezing has been extensively studied at high latitudes (e.g. van Pelt et al., 2016; Van Pelt et al., 2012; Reijmer et al., 2012; Steger et al., 2017), this process has attained little attention at lower latitudes (Samimi and Marshall, 2017). Mölg et al. (2012) and Fujita and Ageta (2000) estimated that a considerable amount of snow meltwater refreezes, 13 and 20% respectively, on two glaciers on the Tibetan Plateau, using an energy-balance model. Only Saloranta et al. (2019) made a first order approximation of the importance of refreezing in a Himalayan catchment. They estimated that 36% of the meltwater, simulated by an ETI-model, refreezes. Based on an extensive set of meteorological and snow observations at two high-altitude sites in the Himalaya, we will quantify the mass and energy balance of the seasonal snowpack, illustrate the importance of refreezing, and elucidate cold content dynamics of the snowpack.

4.2 Study area

The Langtang Valley is located in the Central Himalaya in Nepal (Figure 4.1). The elevation ranges between 1500 m a.s.l. and 7140 m a.s.l. for the highest peak, Langtang-Lirung. In this valley, an extensive set of snow and meteorological measurements was collected at two high-altitude sites, Ganja La (N28.1545, E85.5625) and Yala (N28.2323, E85.6097), at 4962 and 5090 m a.s.l., located at the southern and northern sides of the valley, respectively (Figure 4.1). The climate is monsoon dominated with most precipitation (up to 84%) falling from June to September as rain (Immerzeel et al., 2014; Kirkham et al., 2019). Westerlies transport moist air into the valley during winter, resulting in snowfall at the two high-altitude sites forming a snowpack. The snowpack is typically shallow in the winter months (November–February) based on only a few snowfall events and further accumulates from March until May (Kirkham et al., 2019; Saloranta et al., 2019). Although the sites are only approximately 15 km apart and have generally the same climatic regime, there are distinct differences in the wind, atmospheric moisture and radiation regimes as Ganja La is located south of the water divide, which acts as a topographic barrier.

4.3 Data and methodology

In this study the main focus is on the snow-covered period in 2018 at Ganja La (5 March–25 May) and Yala (9 February–26 May) when meteorological and snow observations were recorded at both sites and captured the full snow season. In order to show interannual variability, data from the Ganja La site was also analyzed for the snow-covered periods in 2017 (27 January–15 May) and 2019 (15 February–10 June).

4.3.1 Meteorological observations

Two automatic weather stations (AWS) recorded hourly meteorological observations at the Ganja La and Yala sites (Figure 4.1). The observed variables include incoming and outgoing shortwave and longwave radiation, wind speed and direction, air temperature, relative humidity and atmospheric pressure (Table 4.1).

4.3.2 Snow observations

A Campbell Scientific CS725 sensor provided automated measurements of the SWE at both sites (Table 4.1). The CS725 passively measures the emitted electromagnetic radiation from the decay of naturally existing radioactive potassium and thallium in the soil. This signal is attenuated due to accumulation of snow; the attenuation of measured electromagnetic energy is then used to calculate SWE. The CS725 measures over a 24-h window to detect a

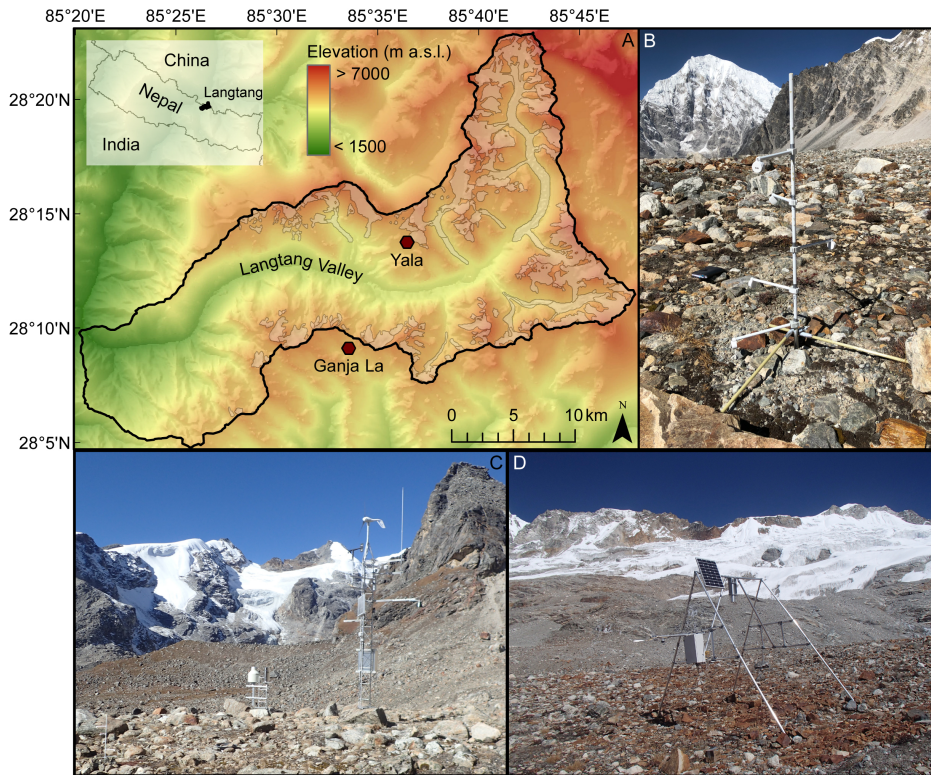


Figure 4.1: Panel A gives an overview of the location of the Langtang Valley and the locations of the two sites (Yala and Ganja La). The white outlines indicate the extent of the glaciers located within the valley. Panel B shows the measurement set-up of the vertical snow temperature profile at Yala (Section 3.2). Panels C and D show the automatic weather stations with the CS725 SWE sensors and the surrounding terrain at Ganja La and Yala, respectively.

sufficient amount of emitted electromagnetic radiation, which is reported every 6 h. The 6-h records of SWE were linearly interpolated to obtain the same hourly temporal resolution as the meteorological observations. In addition, an 18-h time lag was applied to the SWE time series, in accordance with the findings of Kirkham et al. (2019). The footprint of the sensor is a function of the sensor height, i.e. $\sim 150 \text{ m}^2$ and 85 m^2 at the Ganja La and Yala sites, respectively. The accuracy of the measurements is $\pm 15 \text{ mm}$ from 0 to 300 mm and $\pm 15\%$ from 300 to 600 mm. Snow accumulation exceeding 600 mm results in considerable errors. Besides the SWE observations, automated measurements of the vertical snow temperature profiles were measured at the Yala site at approximately 5-m distance from the CS725 (Figure 4.1). Temperature sensors (TidbiT) recorded the snow temperature at 15-min intervals and were positioned at 0, 15, 30, 45 and 60 cm above the snow-ground interface. The observations were aggregated to hourly means to match the temporal resolution of the meteorological observations. The temperature sensors were painted white to reduce the influence of direct radiative warming. The vertical temperature profile provides valuable information on the development of the cold content of the snowpack and the onset of snowmelt. A time-lapse camera provided hourly pictures of the set-up at Yala during the day, which was used to de-

Table 4.1: Description and specifications of the sensors at the locations Ganja La and Yala.

Sensor	Variable	Accuracy	Sensor height (m)
Ganja La			
Campbell Scientific CS725	SWE	$\pm 15 \text{ mm}/\pm 15\%$	4.00
Young Wind Monitor-HD-Alpine 5108-45	Wind speed, wind direction	$\pm 0.3 \text{ m s}^{-1}, \pm 3^\circ$	4.46
Campbell Scientific CS215	Relative humidity	$\pm 4\%$	2.09
Campbell Scientific SR50A-316SS	Air temperature	$\pm 0.2 \text{ }^\circ\text{C}$	3.40
Sutron 5600-0120-3C	Atmospheric pressure	$\pm 0.4 \text{ hPa}$	0.80
Kipp and Zonen CNR4 Net Radiometer	Incoming/outgoing longwave/shortwave radiation	$\pm 3\%$	3.54
Yala			
Campbell Scientific CS725	SWE	$\pm 15 \text{ mm}/\pm 15\%$	2.98
Young Wind Monitor-05103	Wind speed, wind direction	$\pm 0.3 \text{ m s}^{-1}, \pm 3^\circ$	2.50
Campbell Scientific HC2S3	Air temperature, relative humidity	$0.1 \text{ }^\circ\text{C}, \pm 0.8\%$	1.75
Campbell Scientific CS106	Atmospheric pressure	$\pm 1.0 \text{ hPa}$	0.80
Kipp and Zonen CNR4 Net Radiometer	Incoming/outgoing longwave/shortwave radiation	$\pm 3\%$	2.20
HOBO TidbiT v2	Snow temperature	$\pm 0.2 \text{ }^\circ\text{C}$	0.0, 0.15, 0.30, 0.45, 0.60

termine whether the temperature sensors were covered by snow. The time lapse imagery was also used to interpret and quality-check the observed time series of the SWE and to evaluate the patchiness of the snow cover.

4.3.3 Surface energy balance

The net energy (E_{net}) at the snow surface was calculated as the sum of the radiative and turbulent fluxes (all in W m^{-2} ; Equation (4.1)):

$$E_{net} = S_{net} + L_{net} + H + LE \quad (4.1)$$

where S_{net} and L_{net} are the net incoming shortwave and longwave radiation respectively, H is the sensible heat flux and LE is the latent heat flux. Fluxes pointing towards the surface are assumed positive whereas fluxes pointed towards the atmosphere are negative. Heat advection by precipitation has in general a negligible influence on the energy balance of a snow-pack, especially in climates with relatively little accumulation (e.g. Marks and Dozier, 1992). Therefore, heat advection by precipitation was neglected in the calculations of the surface energy balance. The ground heat flux was also excluded in this study as adequate observations of the ground heat flux are non-existing in the Himalaya and therefore its magnitude and potential role in the energy balance remains unknown. The hourly S_{net} was calculated from the hourly observed incoming shortwave radiation multiplied with the albedo at 12 h, when the

solar zenith angle is small. The albedo is inferred from the incoming and outgoing shortwave radiation measurements. However, the albedo was set to a minimum value of 0.46 and 0.41 to exclude the influence of snow patchiness on the observed albedo at the end of the snow season for the Ganja La and Yala sites, respectively. Kirkham et al. (2019) estimated the minimum albedo of continuous snow cover at Ganja La as 0.46. For Yala, the minimum albedo was determined by taking the albedo on the last day that snow cover was continuous (observed using time-lapse imagery). In addition, observations of incoming shortwave radiation at Yala were replaced with observations from a nearby station, located at the same elevation and at 150 m distance (AWS Yala BC; see Shea et al. (2015b) for details), when the measurements of incoming shortwave radiation were influenced by shading of the station structure itself. This mainly occurred in April and May between 7 and 9 h. L_{net} was calculated as the difference between the observed incoming and outgoing longwave radiation. The turbulent fluxes were calculated using the bulk-aerodynamic method, explained in detail in Stigter et al. (2018) and Litt et al. (2014). Stigter et al. (2018) calibrated the roughness lengths for momentum, heat and humidity ($1.3 \cdot 10^{-3}$ m, $1.3 \cdot 10^{-4}$ m and $1.3 \cdot 10^{-4}$ m, respectively) using observed turbulent fluxes with an eddy covariance system on the nearby Yala Glacier, which was snow-covered during the observation period. We used these roughness lengths to calculate the turbulent fluxes at the two sites.

4.3.4 Mass balance

The change in the mass balance of the snowpack (Δ_{mass}) was calculated as the sum of melt, refreezing (*refr*), sublimation (*subl*), evaporation (*evap*), deposition (*dep*), snowfall (*snow*), rainfall (in case of rain-on-snow; *rain*) and redistribution by wind (*red*) at an hourly time step (all in mm; Equation 4.2):

$$\Delta_{mass} = melt + refr + subl + evap + dep + snow + rain + red \quad (4.2)$$

Mass losses were assumed negative, whereas mass gains were positive. Gains in mass by snowfall, rain-on-snow and wind redistribution were merged and derived from increases in the SWE in the CS725 data. Decreases in SWE due to wind redistribution are difficult to derive from the SWE data because decreases in SWE can be a result of both melt and snow erosion by wind, which may both occur during the 24-h measurement interval. Snow erosion by wind has likely only a minor influence on the mass balance, as both locations are relatively sheltered, and especially at Ganja La the wind speed is generally low ($< 2 \text{ m s}^{-1}$). In addition, the footprint of the SWE measurements is relatively large at both sites (85 and 150 m^2), and snow eroded within the footprint may also be deposited within the footprint, resulting in no net change in observed SWE. Therefore, we did not account for mass losses due to wind redistribution in this study.

4.3.5 Snowpack energy balance experiments

Refreezing of meltwater and especially the cold content dynamics of the snowpack are commonly ignored in melt models applied in the Himalaya (e.g. Immerzeel et al., 2012; Ragetti et al., 2015; Saloranta et al., 2019; Shea et al., 2015a; Stigter et al., 2017). We conducted four energy balance experiments using data of the 2018 winter snow season (February until May), with varying assumptions, to quantify the importance of the snowpacks cold content and refreezing of meltwater for the energy and mass balance of the snowpack. The snowpack energy balance experiments in this study are all based on the observed surface energy balance. However, we partitioned the positive net energy at the surface between energy used for warming and energy used for melt of the snowpack, based on applying a threshold value

of 0 °C for the surface temperature (derived from the measured outgoing longwave radiation using the Stefan Boltzmann law). Negative net energy at the surface is either used for cooling of the snowpack or for refreezing of meltwater stored in the snowpack. Cooling of the snowpack only occurs once all meltwater, stored within the snowpack, has refrozen. Consequently, net energy at the snow surface is the same for all experiments. However, the assumption regarding how this energy is used for melting, refreezing or cooling or warming of the snowpack varies among the experiments. The experiments are explained in more detail below. All energy balance calculations were performed as long as the observed SWE exceeded 15 mm, which equals the accuracy of the CS725 (Table 4.1).

Exp. 1 No cold content and no refreezing

It was assumed that all net positive energy is used for melt in this first experiment. Both the cold content of the snowpack and refreezing of liquid water in the snowpack were not accounted for and it was assumed that all meltwater directly runs off.

Exp. 2 Cold content and no refreezing

In this experiment it was assumed that all net negative energy is used for cooling of the snowpack. If the net energy is positive, it is first used to warm the snowpack as long as the surface temperature is below the melting point (0 °C). All remaining positive energy is used for melt, which was assumed to run off directly.

Exp. 3 Cold content and unlimited refreezing

In this experiment, similar to Exp. 2, all positive net energy is first used to warm the snowpack until the surface temperature is 0 °C. All remaining positive energy is used for melt. If the net energy is negative, this energy is directed to refreezing, assuming unlimited availability of water.

Exp. 4 Cold content and water limited refreezing

In this experiment, similar to Exp. 2 and 3, all positive net energy is first used to warm the snowpack until the surface temperature is 0 °C. All remaining positive energy is used for melt. The meltwater is now however retained within the snowpack as long as the water content is lower than 10% of the observed SWE. This 10% of SWE corresponds to a volume % of 1.4–4.6, which, given a range in bulk snow density between 150 and 550 kg m⁻³, is a plausible estimate (Heilig et al., 2015; Samimi and Marshall, 2017; Wever et al., 2015). If the net energy is negative, this energy is used for refreezing as long as liquid water is available in the snowpack. After all available water has refrozen, this negative energy was assumed to cool down the snowpack and increase the cold content.

Using this experimental set-up it is possible to quantify: i) how much of the net positive energy is used for overcoming the cold content of the snowpack (by comparing Exp. 1 and 2), ii) the upper limit of the amount of net negative energy that may be used for refreezing (by comparing Exp. 2 and 3), and iii) how much energy is used for refreezing when the amount of liquid water in the snowpack is realistically constrained by a maximum storage capacity (by comparing Exp. 3 and 4).

4.3.6 Observed vertical snow temperature profile and cold content of the snowpack

In the experimental set-up described above, the cold content is derived based on the surface energy balance. However, the cold content can also be derived independently using the snow

temperature measurements inside the snowpack. The observation-based cold content of the snowpack (CC , J m^{-2}) was calculated using the observations of SWE (m) and average snowpack temperature (T_{snow} , $^{\circ}\text{C}$), based on the observed vertical snow temperature profile (Equation 4.3):

$$CC = c_i \rho_w SWE (T_{snow} - T_{melt}) \quad (4.3)$$

Where c_i is the heat capacity of ice ($2102 \text{ J kg}^{-1} \text{ }^{\circ}\text{C}^{-1}$), ρ_w is the density of water (1000 kg m^{-3}) and T_{melt} is the melting temperature of snow ($0 \text{ }^{\circ}\text{C}$). Warming and cooling of the snowpack was calculated based on changes in the average snowpack temperature and therefore its cold content.

4.4 Results

4.4.1 Observed meteorology and SWE

The 2018 winter season has a continuous time series of SWE at both sites, Ganja La and Yala. There is a persistent ($SWE > 15 \text{ mm}$) snowpack from March 2018 until May 2018 at Ganja La for this season, and from February 2018 until May 2018 at Yala (Figure 4.2). The accumulation of SWE is generally higher at Yala compared to Ganja La, even though the sites only differ slightly in altitude. The SWE time series show large interannual variability of the snow accumulation at both sites, with approximately three times higher maximum accumulation in 2019 than in 2018 (Figure 4.2).

There are clear meteorological differences between Yala and Ganja La when snow is present during the 2018 winter season (Figure 4.3). Figure 4.3 shows differences in the observed wind speed and relative humidity between the two sites. The relative humidity increases at approximately 8 h at Ganja La, whereas it increases at approximately 13–14 h at Yala. At Ganja La, the wind speed is generally low and has no distinct diurnal cycle, whereas at Yala the wind speed has a strong diurnal cycle with higher wind speeds occurring in the afternoon during the entire snow season, potentially linked in with the overall valley circulation. These differences in wind speed are likely a result of the complex interaction between the catchment topography, katabatic and synoptic scale wind patterns.

The surface temperature and air temperature show similar diurnal cycles with equal magnitude at both locations (Figure 4.3). The surface temperature remains below freezing point from February to March at Yala, whereas the surface temperature already reaches $0 \text{ }^{\circ}\text{C}$ at Ganja La in March. The surface temperature shows a gradual shift throughout the snow season towards longer time periods with the surface being at melting point at both sites (Figure 4.3). The snow surface is at melting point for approximately 4–5 h during the day in May, whereas this is roughly 2 h in April on average. The surface temperature occasionally reaches values above $0 \text{ }^{\circ}\text{C}$ in May. This is a result of boulders protruding the snow cover within the footprint of the sensor that can have a higher temperature than a melting snow surface ($0 \text{ }^{\circ}\text{C}$). However, we believe this influence is restricted to late melt season only, when the snowpack is very shallow. The air temperature is consistently higher than the surface temperature during night at Ganja La and Yala for the entire snow season, which is indicative of a positive sensible heat flux. However, at Ganja La the air temperature is considerably lower than the surface temperature from approximately 10 h to 15 h in March and April, whereas at Yala the air temperature is only slightly lower or equal to the surface temperature during daytime.

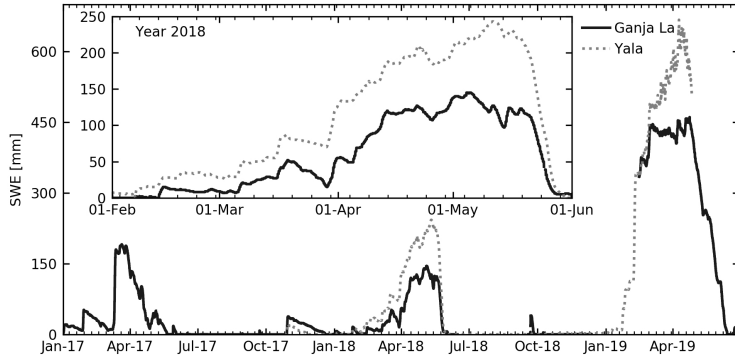


Figure 4.2: Time series of the observed SWE from the CS725 SWE sensor at both Ganja La and Yala from January 2017 until June 2019. Note that the snow accumulation in January 2019 is not captured at Ganja La due to station failure. At Yala, SWE observations are only available from October 2017 until April 2019. Note that observed SWE at Yala exceeds the maximum reliable measurement range of 600 mm in April 2019. The inset shows the evolution of SWE in more detail for the 2018 snow season.

4.4.2 Surface energy balance characterization of the 2018 winter period

Figure 4.4 shows the measured hourly radiative balance and the calculated turbulent fluxes for the two sites Ganja La and Yala for the months February to May 2018 when a snowpack is present. The mean net energy and net shortwave radiation are higher at Ganja La than at Yala during daytime in March, whereas there are negligible differences in the net energy and net shortwave radiation between the two sites during daytime in April and May. The net longwave radiation has a similar magnitude at both sites with less negative values in April and May than in February and March. Conversely, the magnitude of the latent heat flux shows distinct differences between the two sites. During the entire snow season the latent heat flux is considerably higher at Yala compared to Ganja La in the afternoon. This difference is largest in March, where the latent heat flux strongly reduces the net available energy at Yala. The sensible heat flux is a relatively small term compared to the other components of the energy balance and shows similar patterns for both Yala and Ganja La. During daytime the sensible heat flux is negligibly small, whereas the sensible heat flux increases during night, directing energy towards the snowpack, which is most evident in February and March.

4.4.3 Energy and mass balance experiments

The results of the different energy and mass balance experiments are summarized in Table 4.2. These results are discussed in the four Subsections below.

Melt

Snowmelt dominates the seasonal mass and energy balance at both sites, regardless of the experiment (Table 4.2). The seasonal melt estimate is highest for Exp. 1, i.e. 1201 mm/58 $W m^{-2}$ and 1159 mm/43 $W m^{-2}$ for Ganja La and Yala, respectively. The melt estimates are higher at Ganja La compared to Yala (Table 4.2) and are very sensitive to the net shortwave radiation and hence the albedo of the snowpack.

Table 4.3 shows the sensitivity of the melt estimates to the (chosen) albedo at Ganja La and Yala. The cumulative seasonal melt estimates almost double when assuming an albedo of

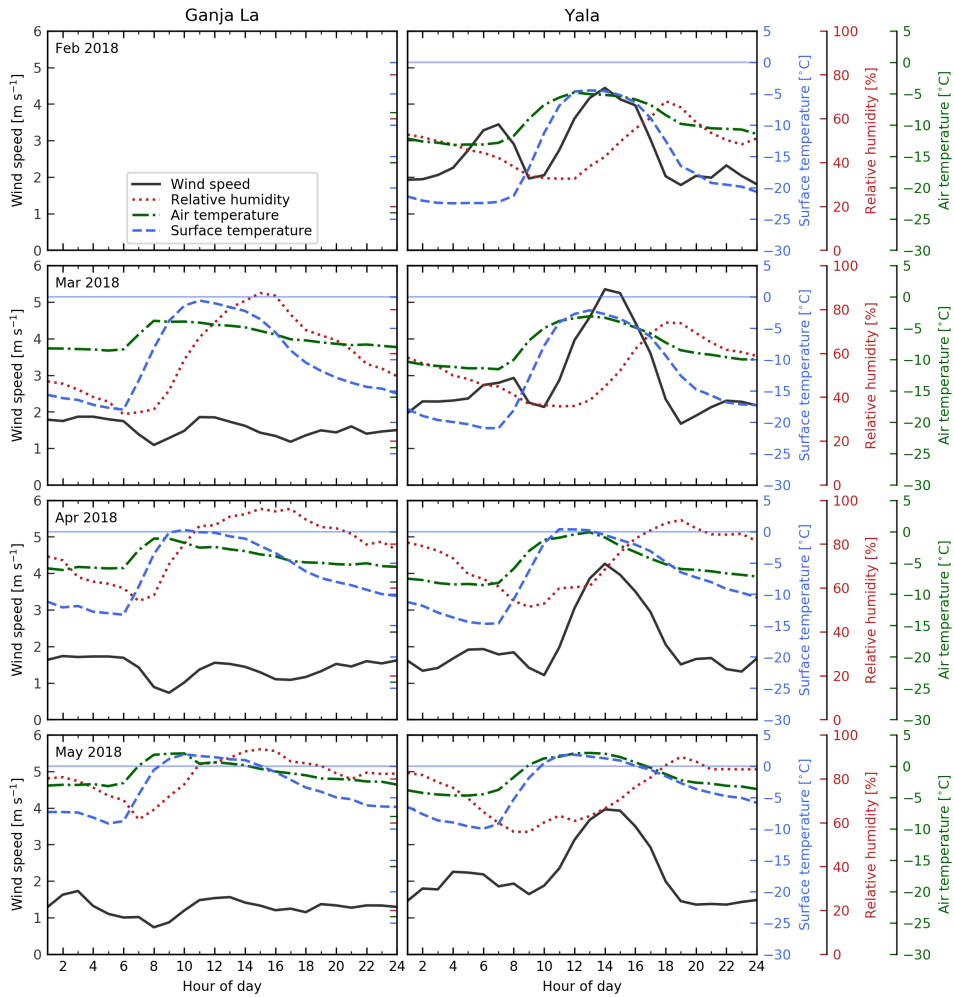


Figure 4.3: Monthly averaged observed wind speed, air temperature, surface temperature and relative humidity at both Yala and Ganja La from February to May 2018 when sufficient snow is present ($SWE > 15$ mm). Snow is not sufficiently present to show the monthly averaged variables at Ganja La in February. The blue horizontal line indicates the zero-degrees line.

0.5 instead of 0.7. For an assumed albedo of 0.9, the major part of the incoming shortwave radiation is reflected resulting in only 67 mm and 60 mm of melt (Table 4.3). Table 4.2 also shows a strong interannual variability in melt at Ganja La. The melt is estimated to be 976 mm in 2017, whereas it is 685 mm and 1066 mm in 2018 and 2019, respectively, according to Exp. 4.

Refreezing

The seasonal refreezing is moderately higher at Ganja La compared to Yala for Exp. 3 and Exp. 4 (Table 4.2). The refreezing estimates in Exp. 3 are higher than in Exp. 4, with increases of 119 and 134 mm at Ganja La and Yala, respectively. This leads to a higher fraction of

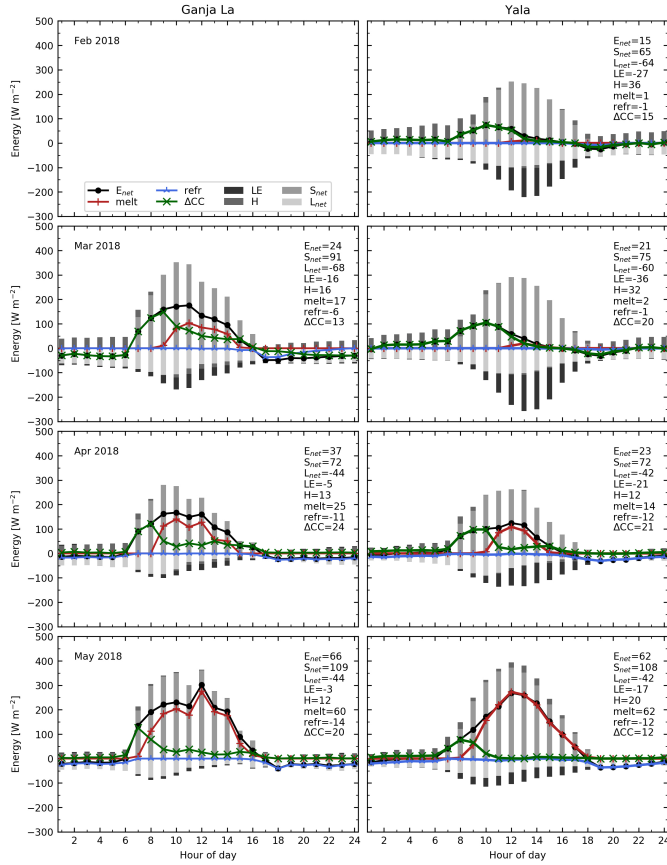


Figure 4.4: Hourly energy balance, including the net shortwave (S_{net}) and net long wave (L_{net}) radiation, latent heat flux (LE) and the sensible heat flux (H). S_{net} and L_{net} are observed values and LE and H are calculated using the bulk-aerodynamic method. The net energy (E_{net}) is the sum of S_{net} , L_{net} , LE and H . Fluxes pointing towards the surface are assumed positive whereas fluxes pointed towards the atmosphere are negative. In addition, the figure illustrates the partitioning of E_{net} over the changes in cold content (ΔCC) of the snowpack (note that a positive ΔCC reduces the CC), melt or refreezing ($refr$). The partitioning of the net energy is based on Exp. 4 (explained in detail in Section 4.3.5). If $E_{net} > 0 \text{ W m}^{-2}$, then E_{net} is partitioned over melt and decrease of the cold content, whereas E_{net} is partitioned over refreezing and increase of the cold content if $E_{net} < 0 \text{ W m}^{-2}$. The monthly averaged values of all energy balance components is given in the text of each panel. Snow is not sufficiently present to show the monthly averaged variables at Ganja La in February.

meltwater that refreezes at Ganja La and Yala for Exp. 3 (0.49 and 0.59, respectively) than for Exp. 4 (0.32 and 0.34, respectively). The refreezing has a strong seasonality and is most substantial in April and May for Exp. 4 (Table 4.2). The refreezing estimates in Exp. 3 are energy limited, whereas the refreezing estimates in Exp. 4 can be either energy or water limited. We used the concept of the Budyko curve to determine whether refreezing is energy or water limited. The Budyko curve normally describes the calculating the ratio of actual and potential evaporation over precipitation. Figure 4.5 shows the adapted Budyko curves (ratio of actual and potential refreezing over melt) for Ganja La and Yala, which illustrate that refreezing (based on Exp. 4) is water limited in February and March (weeks 6–12), whereas

Table 4.2: Results of the different snowpack energy and mass balance experiments at Yala and Ganja La for the 2018 winter season. The experiment numbers refer to the experiments described in Section 3.5. Please note that a positive Δ cold content reduces the cold content of the snowpack. The mass balance is defined as the sum of melt, refreezing, evaporation, sublimation and deposition in which negative values indicate mass losses and positive values indicate mass gains. The evaporation, sublimation and deposition are given in Table 4.4 since these values are constant across the experiments. The results of Exp. 4 are also given for the snow seasons 2017 and 2019 at Ganja La. However, note that the snow accumulation in January 2019 is not captured due to station failure.

		Ganja La				Yala			
		Melt [mm]/ [W m ⁻²]	Refreezing [mm]/ [W m ⁻²]	Δ cold content [W m ⁻²]	Mass balance [mm]	Melt [mm]/ [W m ⁻²]	Refreezing [mm]/ [W m ⁻²]	Δ cold content [W m ⁻²]	Mass balance [mm]
Exp. 1	Feb	-	-	-	-	-113/24	-	-	-128
	Mar	-322/47	-	-	-335	-259/32	-	-	-293
	Apr	-382/49	-	-	-387	-280/36	-	-	-300
	May	-498/80	-	-	-500	-506/76	-	-	-521
2018	Total	-1201/58	-	-	-1222	-1159/43	-	-	-1242
Exp. 2	Feb	-	-	-	-	-6/1	-	14	-21
	Mar	-119/17	-	7	-132	-15/2	-	19	-49
	Apr	-192/25	-	12	-197	-108/14	-	9	-128
	May	-374/60	-	6	-376	-418/62	-	0	-432
2018	Total	-685/33	-	9	-705	-547/20	-	11	-631
Exp. 3	Feb	-	-	-	-	-6/1	41/9	22	20
	Mar	-119/17	158/23	30	25	-15/2	92/11	30	43
	Apr	-192/25	93/12	25	-104	-108/14	99/13	22	-29
	May	-374/60	87/14	20	-288	-418/62	89/13	13	-344
2018	Total	-685/33	338/16	25	-367	-547/20	320/12	22	-310
Exp. 4	Feb	-	-	-	-	-6/1	5/1	15	-17
	Mar	-119/17	44/6	13	-88	-15/2	7/1	20	-41
	Apr	-192/25	87/11	24	-111	-108/14	89/12	21	-39
	May	-374/60	86/14	20	-289	-418/62	82/12	12	-350
2018	Total	-685/33	219/11	19	-486	-547/20	186/7	18	-445
2019	Total	-1066/36	284/10	22	-807				
2017	Total	-976/36	236/10	10	-691				

refreezing is energy-limited in April and May (weeks 13–21).

Table 4.3 also shows the sensitivity of refreezing to the liquid water availability. A difference in albedo of 0.9 and 0.7 gives a large difference in refreezing as melt increases for a lower albedo and so does the liquid water content in the snowpack and the potential for refreezing. However, a difference in albedo of 0.7 and 0.5 does not result in any substantial difference in refreezing (Table 4.3).

Cold content

Table 4.2 shows the average monthly and seasonal cold content changes which were calculated as a residual energy of the surface energy balance for the Exp. 2–4. The seasonal averaged ΔCC is positive, with values ranging between 9 and 25 W m⁻², for all experiments. This means that the cold content of the snowpack is reduced and that the energy is

Table 4.3: Estimated melt and refreezing based on Exp. 4 with differing albedo at Ganja La and Yala for the 2018 snow season. 'Station' refers to the observed albedo at the AWSs, whereas 'Albedo 0.9', 'Albedo 0.7' and 'Albedo 0.5' refer to an assumed seasonal constant albedo of 0.9, 0.7 and 0.5, respectively.

	Melt/Refreezing [mm]			
	Station	Albedo 0.9	Albedo 0.7	Albedo 0.5
Ganja La				
Mar	-119/44	-2/2	-66/41	-160/50
Apr	-192/87	-12/11	-170/84	-343/85
May	-374/86	-53/44	-267/88	-490/84
Total	-685/219	-67/59	-503/216	-993/221
Yala				
Feb	-6/5	0/0	-2/2	-14/6
Mar	-15/7	-1/0	-15/8	-39/11
Apr	-108/89	-4/4	-118/77	-254/74
May	-418/82	-55/49	-293/80	-559/72
Total	-547/186	-60/54	-428/167	-866/164

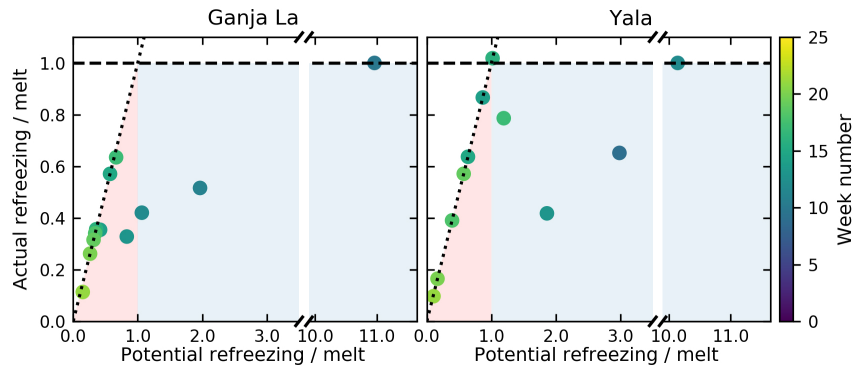


Figure 4.5: Adjusted Budyko curves for Yala and Ganja La for the time period February–May 2018 when sufficient snow is present ($SWE > 15$ mm). The blue shaded area indicates the liquid water limit, whereas the red shaded area indicates the energy limit. The refreezing and melt estimates were aggregated to weekly values. The markers are coloured to the according week number of the year. The potential refreezing is based on the results of Exp. 3, whereas the actual refreezing is based on the results of Exp. 4. Weeks without melt are excluded (weeks 6–8, 10 and 11 for Yala).

used to warm the snowpack. Exp. 3 gives the highest averaged positive values as all negative energy at the snow surface is directed to refreezing in this experiment as water availability is assumed to be unlimited. As a result only positive ΔCC , which warm the snowpack and reduce the cold content, are included in the average value.

Mass balance

The observed seasonal cumulative increase in SWE is higher at Yala (334 mm) than at Ganja La (275 mm), most of which occurs in March and April (Table 4.4). Snowpack ablation is most substantial in May at both sites (Table 4.4). The latent heat flux is considerably higher at Yala, resulting in larger mass losses due to evaporation and sublimation at this site. The deposition is approximately equal at the two sites and has a negligible influence on the mass

balance (Table 4.4). The mass balance does not close for all experiments at both locations, except for Exp. 3 at the Yala site, with only 24 mm difference between observation and calculation of the mass balance. In all other cases, the calculated mass loss for the experiments exceeds the observed mass loss. The overestimation of mass loss is logically largest for Exp. 1, at 966 and 908 mm respectively for Ganja La and Yala.

The interannual variability in accumulation is large at Ganja La. The cumulative increase in SWE in both 2017 and 2019, 364 mm and 737 mm, respectively, are higher than in 2018. The combined loss of snow due to evaporation and sublimation is two times higher in 2017 compared to 2018. The mass balance closes most in 2019 with only 70 mm difference between observation and calculation based on Exp. 4. This gap is larger in 2017 and 2018, at 327 and 230 mm, respectively.

Table 4.4: Seasonal evaporation, sublimation, deposition as calculated with the bulk-aerodynamic method for the 2018 winter season at the locations Ganja La and Yala. The seasonal cumulative increase and decrease of SWE are based on the CS725 SWE observations. Values are also given for the snow seasons 2017 and 2019 at Ganja La. However, note that the snow processes are not captured in January 2019 due to station failure.

	Evaporation [mm]/[W m ⁻²]	Sublimation [mm]/[W m ⁻²]	Deposition [mm]/[W m ⁻²]	Cumulative decrease SWE [mm]	Cumulative increase SWE [mm]
Ganja La					
Mar	-3/-4	-11/-13	1/1	-45	84
Apr	-3/-3	-5/-5	3/3	-35	120
May	-1/-2	-3/-4	3/4	-177	52
Total	-8/-3	-19/-8	6/2	-256	256
2019	-4/-1	-32/-9	10/3	-737	737
2017	-11/-3	-44/-15	4/1	-364	364
Yala					
Feb	-1/-2	-15/-26	1/1	-14	27
Mar	-1/-1	-35/-36	2/2	-28	133
Apr	-6/-5	-16/-18	2/2	-47	127
May	-8/-9	-9/-11	2/3	-246	47
Total	-16/-4	-74/-23	6/2	-334	334

4.4.4 Observed snowpack temperature and change in cold content

Figures 4.6 and 4.7 show the transition of a cold snowpack in winter and early spring to an isothermal snowpack towards the end of the snow season in May. The temperature at the bottom of the snowpack shows no diurnal cycles, whilst the snow temperature closer to the surface shows a diurnal cycle with a minimum temperature of ~ -11 °C around 5 h and a maximum of -2 °C around 13 h at the end of March (Figure 4.6). This diurnal cycle becomes smaller towards the end of the snow season when the snowpack becomes isothermal, with the snow temperature varying between approximately -4 °C and 0 °C. At the end of the snow season the temperature sensor shows above-zero temperature close to the snow-atmosphere interface, due to the influence of solar radiation. The diurnal cycle in snow temperature is a direct indication for the diurnal cycles in cold content. The cold content of the snowpack ranges between 0 and 1.2 MJ m⁻² (Figure 4.7). In February there is first a gradual increase of the cold content followed by a gradual decrease. The data also shows more abrupt increases in cold content, which are related to precipitation events, on 6–7 March, 15–16 March and 30–31 March 2018. From 9 April onwards the snowpack is isothermal during the day, but some cold content develops during the night.

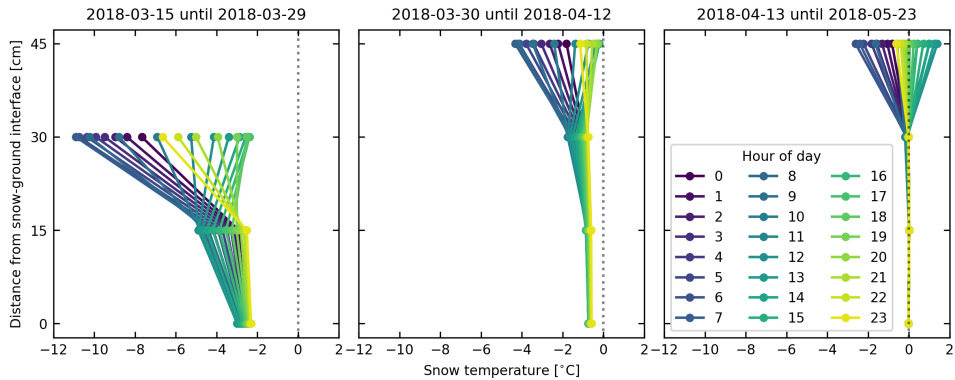


Figure 4.6: Hourly vertical temperature profiles of the snowpack measured with the TidbiTs at Yala, averaged over three different time periods.

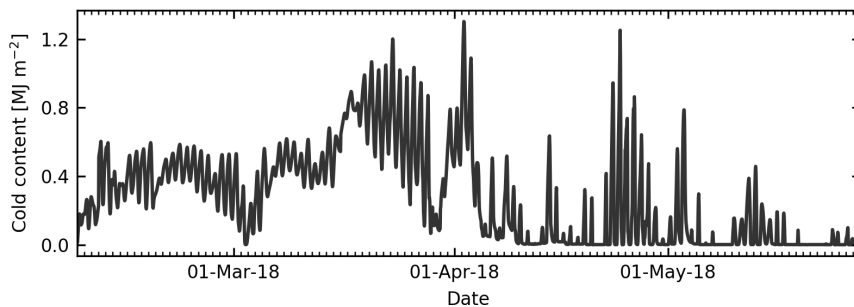


Figure 4.7: The development of the observed cold content of the snowpack throughout the snow season 2018 at Yala.

4.5 Discussion

4.5.1 Meteorological drivers of the surface energy balance

During daytime hours, the net energy is generally more positive at Ganja La compared to the Yala site (Figure 4.4). This is caused by a higher net shortwave radiation at Ganja La due to a lower albedo, which may be partially caused by larger boulders protruding from the snowpack as the snowpack is typically shallower at this site. The surface energy balance is most dominantly influenced by the net shortwave radiation. This is in consensus with the findings of Litt et al. (2019), who studied the contribution of the different surface energy balance components to melt for two glaciers in the Nepalese Himalaya.

Sublimation and evaporation are more pronounced at Yala, effectively reducing the net energy (Figure 4.4) and lowering the surface temperature (Figure 4.3). The higher latent heat flux at Yala is linked to the lower atmospheric humidity and higher wind speeds observed at Yala compared to Ganja La between 10 and 15 h, which is the moment that the latent heat flux typically peaks (Reba et al., 2012; Sexstone et al., 2018; Stigter et al., 2018). The differences in wind speed are likely related to the different aspects of each catchment. Ganja La is located at the end of a north-south oriented valley whereas Yala is located in the middle of an east-west oriented valley (Figure 4.1), resulting in different wind regimes. Figure 4.3 shows that the relative humidity increases at approximately 10 h at Ganja La, whereas this

only increases at approximately 13–14 h at Yala where stronger winds result in stronger mixing. In contrast to the latent heat flux, the sensible heat flux is on average positive at both sites (Figure 4.4), warming the snowpack, with highest values during night when the difference between the temperature of the snow surface and near surface air temperature is largest (Figure 4.3). This is mainly observable in February and March at Yala. During the night, the positive sensible heat flux is (partly) offset by the negative net longwave radiation, resulting in a slightly negative or zero net energy (Figure 4.4).

4.5.2 Energy and mass balance experiments

Melt

The melt estimates are very sensitive to the assumption under which snowmelt conditions occur. In Exp. 1 it was assumed that melt occurs once the net energy is positive. In the other experiments melt only occurred when the snow surface was observed to be at melting point in addition to available positive net energy. The seasonal melt estimates, without accounting for the cold content of the snow, are 2.1 and 1.8 times higher for Yala and Ganja La, respectively (Table 4.2). The melt estimates in Exp. 1 (1159 mm and 1201 mm) are unreasonably high compared to the observed seasonal cumulative decreases in SWE, i.e. 334 mm and 256 mm for Yala and Ganja La, respectively (Table 4.4). This shows that it is essential to include a threshold on the surface temperature when calculating melt based on the surface energy balance. The large difference between the calculated melt in Exp. 1 and the observed decrease in SWE also indicates that a large part of the net positive energy is likely used to overcome the cold content of the snowpack. The melt estimates are primarily driven by the net shortwave radiation, which in turn is highly sensitive to the albedo of the snowpack (Table 4.3). This is because the incoming shortwave radiation is relatively high in the Nepalese Himalaya due to the high altitude and low latitude compared with other mountain ranges in the world. An albedo of 0.7 halves the melt compared to using a value of 0.5, decreasing to just 7% when it is increased further to 0.9. The sensitivity of the surface energy balance to albedo is in consensus with previous studies on high-altitude Himalayan glaciers (Litt et al., 2019; Matthews et al., 2020). Indeed, the mass balance of Himalayan glaciers is most sensitive to variations in shortwave radiation and albedo (Azam et al., 2014; Kayastha et al., 1999). Results from this snowpack study and previous glacier studies indicate that future snow and ice melt estimates based on the surface energy balance should – in the absence of observations – carefully choose an albedo parameterization and account for its uncertainties.

Most of the seasonal melt occurs at the end of the snow season in May at both sites (Figure 4.4 and Table 4.2) 374 mm and 418 mm of snow melts in May, which is 55% and 76% of total melt at Ganja La and Yala, respectively. In May, an increased amount of energy is available for melt at both sites. This is caused by i) increased net shortwave radiation due to decreasing albedo, ii) decreased latent heat flux due to increased atmospheric humidity and iii) less negative net longwave radiation due to more incoming radiation because of higher air temperature and increased atmospheric humidity. Note that at Yala the sensible heat flux also increases during daytime in May (Figure 4.4), which may be (partly) caused by the development of a patchy snow cover and consequently higher air temperature due to heat advection from non-snow-covered areas (Mott et al., 2011; Schlögl et al., 2018; Shook and Gray, 1997). Even though this process is minor compared to the increase in net shortwave radiation at Yala, it does increase the melt rates. This effect is less apparent at Ganja La due to the lower wind speeds observed there.

Refreezing

Refreezing of meltwater in a snowpack can be either water limited or energy limited. Assuming unlimited water availability (Exp. 3) leads to 119 mm and 134 mm more refreezing than for the water limited case (Exp. 4) at Ganja La and Yala, respectively (Table 4.2). This indicates that refreezing is (partly) water limited. Especially in March the refreezing rate is significantly higher in Exp. 3 compared to Exp. 4 as net energy is negative during night, favorable for refreezing, but in Exp. 4 no meltwater is available to refreeze. Figure 4.5 further illustrates when refreezing is energy or water limited. All data points located in the red and blue-shaded areas indicate whether refreezing is energy or water limited, respectively. Figure 4.5 demonstrates that refreezing is water limited at the start of the snow season (darker points), whereas refreezing becomes energy limited in spring (lighter points). The point just above the water limit at Yala means there is more refreezing than the actual meltwater produced during that week. The additional liquid water availability for refreezing can be explained by meltwater storage within the snowpack of the previous week. Table 4.3 shows that albedo also indirectly influences the estimated refreezing as it determines how much meltwater is available for refreezing. Therefore, albedo is not only important to quantify melt, but also to quantify refreezing.

If refreezing occurs, a part of the positive net energy is used to melt previously frozen meltwater. Therefore, in cases where seasonal melt exceeds the observed decreases in SWE, refreezing is likely the process that closes the potential gap in the mass balance. The difference in mass balance closure between Exp. 3 and Exp. 4 (Table 4.2) suggests that the amount of refreezing is insufficient to close the gap when meltwater retention within the snowpack is limited to values reported in literature (Heilig et al., 2015; Mitterer et al., 2011; Samimi and Marshall, 2017; Wever et al., 2015). Bayard et al. (2005) observed the presence of a basal ice layer when the soil beneath a snowpack was frozen for two alpine sites in Switzerland. In their case winter melt occurred. The meltwater percolated throughout the snowpack but at the base of the snowpack the water could not infiltrate due to frozen soil, forming the basal ice layer. If infiltration actually happens in frozen soils, the meltwater can refreeze and contribute to the development of a basal ice layer (Marsh and Woo, 1984). We therefore hypothesize that refreezing may not only consist of meltwater retained within the snowpack, but also of refreezing of ponded meltwater at the snowpack base. Ponding of meltwater at the snowpack base was observed at both Ganja La and Yala during fieldwork in April 2018. Kirkham et al. (2019) observed 3–4 ice lenses, each approximately 10 mm thick, within the snowpack (Figure 4.8) and a basal ice layer of approximately 30 mm w.e. present in 12 snow pits dug within the footprint of the CS725 SWE sensor at Ganja La on April 30th 2018. At some locations within the footprint, the basal ice layer had a thickness of up to 110 mm (Kirkham et al., 2019). This supports the idea of having substantial refreezing at the base of the snowpack besides refreezing within the snowpack itself. However, no basal ice layer was observed on April 25th 2018 in three snow pits within the footprint of the CS725 SWE sensor at Yala. Instead, the snow at the base of the snowpack was wet and each of the three snow pits contained 5 ice layers, 10–15 mm thick within the snowpack (Figure 4.8). The difference in the presence of a basal ice layer at the two sites may be a result of thermal insulation of the snowpack. The accumulation is higher at Yala than at Ganja La (Figure 4.2), resulting in stronger insulation of the meltwater at the bottom of the snowpack from surface energy inputs at Yala. Our bulk approach does not resolve the effect of thermal insulation on deeper layers. Therefore, refreezing of meltwater may be overestimated using a bulk approach under the conditions mentioned above. Nevertheless, a comparison of the observed ice layers with refreezing estimates based on Exp. 4 show that the estimated refreezing at Ganja La (131 mm) is within the range of the observed ice layers (60–140 mm) on 30th of

April. The refreezing estimate (92 mm) slightly exceeds the observed ice layers (50–75 mm) at Yala on the 25th of April. However, refreezing does not necessarily result in ice layers only. For example, a 60 mm thick melt-freeze crust was present in snow pit 3 at a depth of 15–21 cm from the snow surface at Yala (Figure 4.8). This indicates that the actual refreezing is more substantial than estimates based on ice layers only. The estimates of refreezing for Exp. 3 are substantially higher than observations, indicating that Exp. 4, which includes a water limit, captures the refreezing more realistically. The results of Exp. 4 show that 32% and 34% of the seasonal melt is melt of refrozen meltwater at Ganja La and Yala, respectively. This is comparable to a first-order approximation by Saloranta et al. (2019), who estimated that 34% of total snow meltwater refreezes at the Ganja La site and that 36% refreezes on average over the entire Langtang catchment. Samimi and Marshall (2017) measured values of 9% in a supraglacial snowpack in the Canadian Rocky Mountains during the ablation season. In their study the value is likely lower due to the presence of a deeper snowpack and percolation of meltwater to deeper parts that are more isolated from energy changes at the snow-atmosphere interface. In addition, they focused on the ablation season in which the supraglacial snowpack was mainly isothermal, reducing the refreezing. Besides the influence of refreezing on the mass balance, the melt of refrozen meltwater is an energy sink, consuming 19% and 16% of the total observed positive net energy at Ganja La and Yala, respectively. Refreezing is therefore a considerable component in the energy balance and mass balance of the seasonal snowpack in 2018. Again, the energy sink was measured to be 9% in the study of Samimi and Marshall (2017). At Ganja La, the seasonal refreezing was also calculated for 2017 and 2019. In these years the energy sink is 17% and 16%, respectively, which is within the same range as in 2018. The percentage of meltwater that refreezes is also comparable in 2017 and 2019, at 24% and 27%, respectively, to 2018.

Besides temporal variability, refreezing will also vary spatially. For example, Ayala et al. (2017b) showed that refreezing is maximal at an elevation ranging between 4500 and 5000 m a.s.l. in the Andes by using a distributed energy balance model. At higher altitude (> 5000 m a.s.l.), refreezing is limited by available meltwater. At lower elevations (< 4500 m a.s.l.) refreezing is limited to available water, but this is caused by a shallower snowpack and therefore small liquid water storage capacity (Ayala et al., 2017b). For this reason refreezing is also reduced during the ablation season when the snow depth becomes smaller (Ayala et al., 2017a). Saloranta et al. (2019) showed that refreezing is most substantial at an altitude ranging between 5000 m and 6000 m a.s.l. in the Langtang catchment. Future work should focus on quantifying refreezing in space using an energy balance-approach.

Cold content

The seasonal averaged change in cold content (including both positive and negative changes) is only 1 W m^{-2} , based on the observed vertical snow temperature profile at Yala. This appears small compared to the other components of the energy balance. However, the positive and negative changes in the cold content balance each other out. The seasonal average decrease in cold content of the snowpack (positive changes only) was estimated to be 9 W m^{-2} . This means that, on average, 9 W m^{-2} of the net positive energy is used to reach an isothermal snowpack and initiate melt onset. This energy flux is substantial since the total net positive energy available in February–May 2018 is on average 43 W m^{-2} (Figure 4.4). The large fraction of positive energy used (21%), is caused by the strong diurnal cycles of warming during daytime and cooling overnight (Figure 4.6). This illustrates that it is key to account for the daily cycles of the cold content in energy balance based snowmelt models. This has also been shown by the difference in the melt estimate between Exp. 1 and the other experiments (Table 4.2).

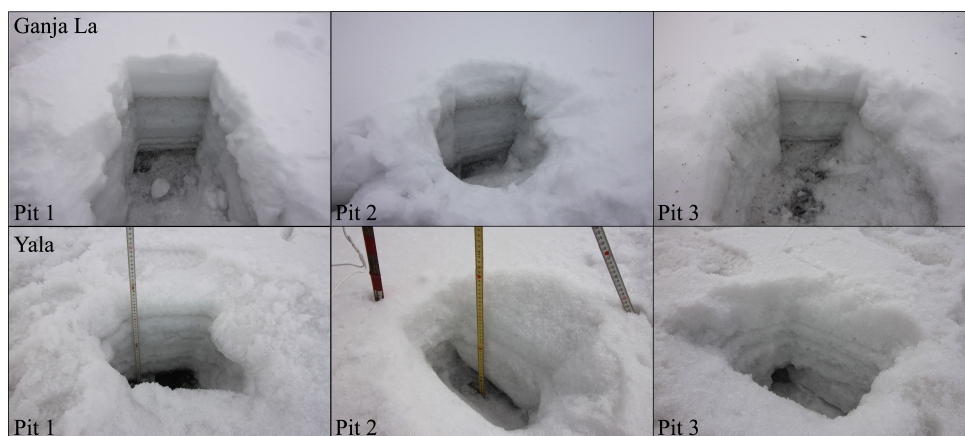


Figure 4.8: Pictures of three snow pits at Ganja La on April 30th 2018 and Yala on April 25th 2018. The snow pits at Ganja La have a depth of 41–42 cm and contain four or five ice layers. The snow pits at Yala have a depth of 38–44 cm and contain five ice layers.

The observed cold content of the snowpack at Yala shows a regular diurnal cycle, but also a few abrupt step-wise increases unrelated to the daily cycle (Figure 4.7). These sudden increases in the cold content of the snowpack on 6–7 March, 15–16 March and 30–31 March 2018 coincide with substantial increases of SWE due to snowfall, i.e. 20 mm, 28 mm and 46 mm, respectively. Jennings et al. (2018) showed that precipitation is the primary source for cold content additions to the snowpack for an alpine snowpack in the Colorado Rocky Mountains. The secondary source in this study is a negative surface energy balance. According to Jennings et al. (2018), three main approaches exist to estimate the cold content of a snowpack, namely: i) as an empirical function of cumulative air temperature, ii) as an empirical function of cumulative precipitation and corresponding temperature (which is often assumed equal to the air temperature), and iii) as a residual of the surface energy balance. As the observed cold content in our study shows both diurnal cycles and abrupt increases, this indicates that the cold content is influenced by both cold content gains from snowfall and from the surface energy balance residuals (Figure 4.7). Nonetheless, no (statistically significant) relation was found between changes in the observed cold content of the snowpack and increases in SWE (following the above-mentioned method ii) or between changes in the cold content of the snowpack and surface energy balance residuals (taken from Exp. 4). This can be (partly) explained by the different climate in the study of Jennings et al. (2018). For example, there is more accumulation of SWE and also the surface energy balance is less driven by shortwave radiation than at Yala. Longer observational time series are required to investigate whether the relations shown by Jennings et al. (2018) also hold for the climate in the Central Himalaya.

4.5.3 Closure of the mass and energy balances

We hypothesize that the results of Exp. 4 should get closest to the observations as it includes melt, the cold content and water limited refreezing. The sum of estimated melt, refreezing, evaporation, sublimation and deposition (disregarding erosion by wind) should match the observations of cumulative decrease in SWE over the entire snow season. However, the observations show a seasonal decrease of SWE of 256 mm (Ganja La) and 334 mm (Yala), whereas the results of Exp. 4 show mass losses of 486 mm and 445 mm, respectively (Tables

4.2 and 4.4). This is a substantial difference. Exp. 3 closes the mass balance most due to more refreezing as there is unlimited water availability for refreezing when the net energy is negative (Tables 4.2 and 4.4). The snow pit observations show that the estimated refreezing in Exp. 4 matches the observed ice layers both within and at the base of the snowpack. Nevertheless, the actual refreezing exceeds these observations as refreezing does not necessarily result in ice layers only. This indicates that Exp. 4 may represent the lower boundary of refreezing estimates. The actual refreezing is likely within the range of the estimates of Exp. 3 and Exp. 4. The remaining gap in the mass balance is due to nonclosure of the energy balance. This nonclosure of the energy balance is visible in the estimates of the seasonal averaged change in cold content according to Exp. 4, i.e. 18 W m^{-2} at Yala (Table 4.2). This value is considerably higher than the observation based estimate of 1 W m^{-2} (described in Section 4.3.6) and suggests a positive imbalance of 17 W m^{-2} in seasonal mean measured energy at Yala. That mass and energy balance do not close has been reported before for seasonal snow cover overlying frozen soils (e.g. Helgason and Pomeroy, 2012a; Pan et al., 2017). Several reasons could explain the imbalance in our study. Firstly, the surface energy balance is highly dependent on the incoming shortwave radiation and albedo (Table 4.3). A small measurement error in either the incoming shortwave radiation or albedo could result in the observed gap in the energy and mass balance. Secondly, and related to the previous argument, the melt estimates are sensitive to the assumed threshold value of SWE (15 mm) for the presence of snow. Thirdly, heat advection of precipitation was not included and is likely a minor term, increasing the cold content of the snowpack. Fourthly, the ground heat flux was not accounted for and can be a potential source or sink of energy (Granger and Male, 1978; Helgason and Pomeroy, 2012a). Yet, no adequate observations exist in the Himalaya to quantify the potential magnitude of this flux and only few observations exist elsewhere. Fifthly, there are uncertainties related to the calculated turbulent fluxes (e.g. Foken, 2008; Helgason and Pomeroy, 2012a; Helgason and Pomeroy, 2012b). However, the magnitude of turbulent fluxes is generally smaller than the radiative components. Helgason and Pomeroy (2012a) concluded that their energy imbalance could be closed with an unmeasured windless sensible heat exchange, but this process remains poorly understood. Besides uncertainties in the quantification of snow processes that influence the snowpack mass balance, there are also uncertainties in the observed SWE. The observed peak SWE is below 300 mm at both sites in the 2018 winter season, which is analyzed here. Therefore, a 15 mm uncertainty estimate applies (Section 4.3.2). In addition, uncertainty in the observed SWE may arise from the relatively large measurement interval of the CS725. The CS725 measures over a 24-h window, which is reported every 6 h. Increases and decreases of SWE within the 24-h interval may balance out. However, these sources of uncertainty are virtually impossible to quantify.

4.6 Conclusions

In this study, based on unique high-altitude snow and meteorological observations, the link between the observed energy balance and snowmelt, refreezing and cold content of the snowpack was systematically addressed and the following key conclusions can be drawn:

In a Himalayan setting with its high altitude, relatively low latitude and limited cloud cover during the melt season, the net energy for snow processes is primarily driven by the net shortwave radiation. This makes melt models and estimates highly sensitive to the snow albedo and potential measurement errors in shortwave radiation. Subtle spatial differences in net energy are likely linked to different wind and humidity patterns and the associated magnitude of turbulent fluxes.

The amount of net positive energy during February until May in 2018 is approximately two

times larger than what is required to melt the snowpack at both sites considered. This illustrates the importance of accounting for the cold content of the snowpack and the refreezing process.

The experimental results show that refreezing plays a critical role in both the energy and mass balance of the snowpack. In case of unlimited liquid water in the snowpack, 49% and 59% of the melt refreezes again for Ganja La and Yala, respectively. In the case when water is limited this amount reduces to 32% and 34%, respectively.

A considerable amount of positive net energy (21%) is used to overcome the nightly increase in cold content and achieve the 0 °C isotherm conditions to initiate melt during the day at one of the locations, which is based on observed snow temperature profiles. Analysis of surface energy balance residuals showed that, with the exception of May, when the snowpack is largely isothermal, this amounts up to 50% at both considered locations.

The mass and energy balance is not entirely closed. Even considering the cold content and refreezing, there is still more energy available than what is required to melt the snowpack. Possible explanations, which require further study, are uncertainties in the measurements of shortwave radiation, the observed albedo and possible sinks of energy which are not considered such as refreezing of a ponded water/ice layer at the soil-snow interface, an increase in cold content by fresh snowfall and the ground heat flux.

4.7 Acknowledgements

We acknowledge Mark Eijkelboom for designing and constructing the vertical snow temperature profile set-up. We would also like to acknowledge Tom Matthews for helpful discussions on the snowpack energy balance closure at high altitude in the Himalaya. We thank members of ICIMODs Cryosphere Initiative, all porters and guides from Thamserku and Glacier Safari Trekking for their support in the field. The views and interpretations in this publication are those of the authors and are not necessarily attributable to ICIMOD. We also gratefully acknowledge the two anonymous reviewers and the editor Jukka Tuhkuri for providing comments that helped improve this manuscript.

Chapter 5

Synthesis

5.1 Main results in this thesis

Cryosphere studies in the Himalaya have predominantly focused on glacier dynamics. In contrast, snow dynamics have remained relatively unstudied. Since the snow covered area in the Himalaya is considerably larger than the glacier area, it is safe to assume that snowmelt plays a key role in the Himalayan water cycle. Yet, we have only little knowledge of the energy and mass balance of the snowpack in the Himalaya. Especially, studies based on in situ snow observations are lacking. Therefore, the aim of this thesis is:

To improve the understanding of snow processes in the Himalaya by combining in situ observations of the seasonal snowpack with remote sensing and modelling.

In this thesis I combined snow observations, remote sensing and modelling to quantify and improve the understanding of a selection of snow processes. I focused specifically on quantifying the snow water equivalent, sublimation, refreezing of snow meltwater and cold content dynamics of the snowpack. Below I recapitulate the research questions and its answers:

How much water is (seasonally) stored as a snowpack in a Himalayan catchment? And what is the sensitivity of the snowpack to changes in precipitation and air temperature?

In Chapter 2, I demonstrate, based on a combination of in situ observations, remote sensing and modelling, that the snow water equivalent in the Langtang catchment has a strong gradient with elevation and increases with increasing elevation. At high altitude, the spatial distribution of the snow water equivalent is dependent on the spatial distribution of precipitation. Perturbations of air temperature and precipitation revealed that at high altitude the increased melt due to increased temperature can be offset by an increase in precipitation. At lower altitude an increase in temperature causes a strong decline in the snow water equivalent due to an increase in snowmelt and decrease of precipitation in the form of snowfall. In Chapter 4, I show that the observed maximum snow water equivalent at two locations at approximately 5000 m a.s.l. ranges between 150 and 600 mm. The three-year data set shows that the annual variability in the snow water equivalent is large.

What is the importance of snow sublimation in the high-altitude water cycle?

In Chapter 3, I show, based on a 32-day record of eddy covariance measurements, that the average daily snow sublimation was 1 mm between October and November in 2016 at an altitude of 5350 m a.s.l. However, strong variations of daily sublimation exist due variations in atmospheric humidity, wind speed and incoming shortwave radiation. Model simulations using the bulk-aerodynamic method reveals that cumulative sublimation at the station's location is 125 mm for the winter season (6 months). Together with modelled evaporation (9 mm), I conclude that 21% of the yearly snowfall is returned to the atmosphere, which is

substantial. Furthermore, I show with spatially distributed simulations on Yala glacier, that the sublimation increases with increasing wind speed. At the ridge of Yala glacier, where the wind speed is significantly higher, the sublimation is a factor 1.7 higher. In contrast, the sublimation was a factor 0.8 less at the lower part of the glacier. In summary, sublimation is substantial, returning a significant amount of snow back into the atmosphere in form of water vapour. This indicates the importance of sublimation and the need to account for sublimation in future hydrological and snow studies.

What is the role of meltwater refreezing and cold content dynamics in the energy and mass balance of a seasonal snowpack at high altitude?

In Chapter 4, I quantify the refreezing of snow meltwater at two high-altitude locations based on energy balance and mass balance simulations and in situ observations of the meteorological conditions. Refreezing is substantial as 32-34% of the snow meltwater refreezes again. At the same time, 16-19% of the positive net energy is on average used to melt refrozen meltwater. Also, cold content dynamics have a significant influence on the energy balance of the snowpack. At one of the sites, where both snow temperature and the snow water equivalent were measured, daily warming of the snowpack (after nightly cooling) consumed 21% of the positive net energy. This is important too as it indicates that simple melt models that do not account for cold content dynamics might simulate too much melt as in such simple models the cold content of the snowpack does not have to be overcome before melt initiates.

5.2 Future research and recommendations

In the future, it will remain challenging and expensive to perform field observations in the Himalaya. We should aim for increasing the number of field observations to be able to quantify snow processes and to calibrate, validate and force hydrological and snow models. However, I fully realise this is easier said than done, also based on my own experiences in the field. Fieldwork in the Himalaya comes with large logistical and cultural challenges, as well as high physical demands. To overcome a part of these challenges I suggest to develop a limited number of super sites by a consortium of international and regional partners. At these super sites long term systematic, standardized measurements need to be conducted that can form a benchmark for a broad range of studies. However, attracting donors to fund such initiatives, fostering collaborations and data sharing mechanisms remain a large challenge for the future.

Besides in situ snow observations, remote sensing techniques are advancing and provide us with an increasing amount of information. Active radar remote sensing has the possibility to provide information about more snowpack properties than optical remote sensing as the signal penetrates into the snowpack. For example, Marin et al. (2020) demonstrate that active radar observations (Sentinel-1) can be used to detect the different phases of snowmelt. This provides very valuable data to validate or calibrate more sophisticated snow model simulations that take into account the sequence of snowmelt phases. The use of active radar in extreme topography comes with challenges regarding correcting/processing the imagery. Nevertheless, Lievens et al. (2019) and Lievens et al. (2022) demonstrate it is feasible to retrieve useful information about for example snow depth in alpine terrain using active radar remote sensing.

Wind-induced snow transport is another snow process that has not yet been quantified in the Himalaya based on observations and modelling. Quantifying this, will help to understand how substantial snow redistribution in Himalayan catchments is. A first step in quantifying this process, would be to quantify the extent of snow redistribution and locate areas with erosion and accumulation in Himalayan catchments. This could be done by using the approach

of Wayand et al. (2018). In their study they make use of high-resolution remotely sensed snow cover (Sentinel-2 and Landsat-8) to calculate a snow persistence index and snow absence index to identify accumulation and erosion zones, respectively. This approach might be valuable for a first order approximation of the extent of snow redistribution in the Himalaya. Also, in a later stage this approach can be used to validate simulations of redistribution of snow.

In Chapter 3, I showed that sublimation is an important component of the high-altitude water balance. This is supported by findings of Mandal et al. (2022). They showed that 16-42% of the seasonal snowfall is returned to the atmosphere due to sublimation using the bulk-aerodynamic method driven by in situ meteorological data at a point location (4863 m a.s.l.) in the western Himalaya. The challenge is to quantify sublimation also spatially distributed. My initial hypothesis was that sublimation would increase with increasing elevation as the sites are generally more exposed and high wind speeds prevail, as also shown in Chapter 3 on Yala glacier. However, unpublished eddy covariance measurements on Mera glacier (Khumbu region) at an altitude of 5770 m a.s.l, revealed that even though wind speeds were significantly higher compared to Yala glacier, the snow sublimation rate in November was 0.7 mm on average. This is lower than the measured sublimation rate on Yala. Atmospheric moisture conditions were similar, but the difference between both sites was the surface temperature of the snowpack. The surface temperature of the snowpack on Mera glacier was lower. Consequently, the saturation vapour pressure at the surface is lower, reducing the near-surface vapour pressure gradient and, hence, the sublimation rate. These findings are supported by findings of Mandal et al. (2022). Their meteorological data and model simulation also reveal that sublimation rates are reduced during cold surface conditions. This shows the importance of performing spatially distributed simulations of snow sublimation including explicitly taking account of snow surface temperature to further quantify the role of snow sublimation in the high-altitude water balance.

In general, I believe it is time to take the next step and finally start simulating the snowpack spatially distributed in Himalayan catchments using more sophisticated snow models, such as ALPINE-3D, CROCUS or SnowModel. These models simulate the snowpack by simulating the full energy and mass balance of the snowpack. Obtaining the required meteorological fields is a challenge, but not impossible as long as a proper uncertainty analysis is included. For example, the existing monitoring network in the Langtang catchment (Steiner et al., 2021) could potentially be used to obtain the required fields using interpolation techniques. To conclude, simulating the spatially distributed energy and mass balance, allows to estimate the spatial distribution of key snow processes that have been quantified at a point scale in this thesis, i.e. sublimation, refreezing of snow meltwater and cold content dynamics of the snowpack. This will provide essential knowledge about the importance of these snow processes in the high-altitude water cycle in Himalayan catchments.

I strongly advocate that we take a process-based approach in understanding snow dynamics. Temperature index models do not justify and cannot capture the processes I have focused on in this thesis. It is true that the data availability in the Himalaya is small compared to for example the Alps, however, by making smart combinations between field-based observations at super sites, remote sensing and downscaled re-analysis and climate model outputs we will be able to much better quantify the role of the snowpack in the high-altitude water cycle. Similar to the recent great leaps in glaciological knowledge in the Himalaya, evolving snow science further in the Himalaya is the next logical jump in knowledge and I hope I have taken the first small steps in data-driven process based understanding of snow processes in the Himalaya.

Appendix A

WRF

WRF configuration

WRF was run for a characteristic humid and non-humid day, i.e. 1 January 2017 and 12 November 2016 respectively, from 5h45 to 17h45 local time. The WRF-runs have 6 nested domains with grid spacings of 12.15, 4.05, 1.35, 0.27, 0.09, 0.03 km. The grid dimensions (XY) are 166x166, 166x166, 166x166, 201x201, 166x166, 166x166 grid points. Each nest has 140 vertical levels. One-way nesting was used, and the largest domain was forced with 6-hourly ERA-INTERIM data ($0.75^{\circ} \times 0.75^{\circ}$) (Dee et al., 2011). Table A.1 gives an overview of the configuration of WRF. In the WRF-runs the glacier is covered by snow with a snow depth of 10 cm. The albedo is preset to a value of 0.70. The surface temperature is solved iteratively through energy balance equations in WRF. A detailed description can be found in Niu et al. (2011). The landuse in WRF is based on the FAO landuse (<http://ref.data.fao.org/web/guest/map?entryId=46d3c2ef-72c3-4f96-8e32-40723cd1847b&tab=metadata>), which is derived from Landsat imagery. The spatial resolution of the landuse product is 0.5 arc seconds and is resampled to the grid size of each domain, taking the dominant landuse in each grid cell. A variety of topography inputs were used for the different spatial resolutions of the domains. The topography input for D1–6 is 2m, 30s, 3s, 3s, 1s and 1s, respectively. The following three products were used for the topography in the WRF domains:

1. GMTED2010 (30s)
2. NASA Shuttle Radar Topography Mission Global 3 arc second SRTMGL3S (3s)
3. Shuttle Radar Topography Mission (SRTM) data at 30-meter at equator (1s)

Validation of WRF with meteorological observations

WRF simulations were validated with on-glacier observations of wind speed, specific humidity and surface temperature (Figure A.1). WRF captures the higher wind speeds at the ridge compared to the other two station locations on both the humid day and non-humid day. On the non-humid day erroneous high wind speeds are simulated at 17-18h, which may be a result of instability in WRF. As a result, the diurnal cycle is not captured by WRF. On the humid day low wind speeds are simulated, which coincide with observations of low wind speed. WRF outputs 10 m wind fields as the lowest level. Deviations in wind speed between the simulations and observations may be partly explained by the difference in observation height and 10m level wind speed in WRF. The daily patterns in specific humidity are similar for WRF and the observations. On the humid day the observed and simulated specific humidity are the same order of magnitude for all stations, whereas the non-humid day shows more deviation between observed and simulated specific humidity. Both the observations and WRF

simulations show a diurnal cycle in surface temperature. During midday the bias between the observations and WRF is small, whereas it is larger in the morning and late afternoon.

Table A.1: Overview of WRF configuration.

Domain configuration		
Horizontal grid spacing	12.15, 4.05, 1.35, 0.27, 0.09 and 0.03 km	
Grid dimensions	D1-3, 5-6: 166x166 D4: 201x201	
Vertical levels	140	
Time step	15, 5, 5/3, 1/6, 1/12, 1/24s	
Nesting approach	One way	
Model physics		
Microphysics	Morrison	Morrison et al. (2009)
Radiation	RRTMG	Iacono et al. (2008)
Surface layer	MM5 Similarity	Paulson (1970)
Land surface	NoahMP	Niu et al. (2011)
Planetary boundary layer	D1-3: YSU (topo_wind=1) D4-6: Full diffusion	Hong et al. (2006)
Cumulus	D1: Kain-Fritsch	Kain (2004)
Dynamics		
Top boundary condition	Rayleigh damping	
Lateral boundary forcing	6-hourly ERA-INTERIM data (0.75°x0.75°) Dee et al. (2011)	

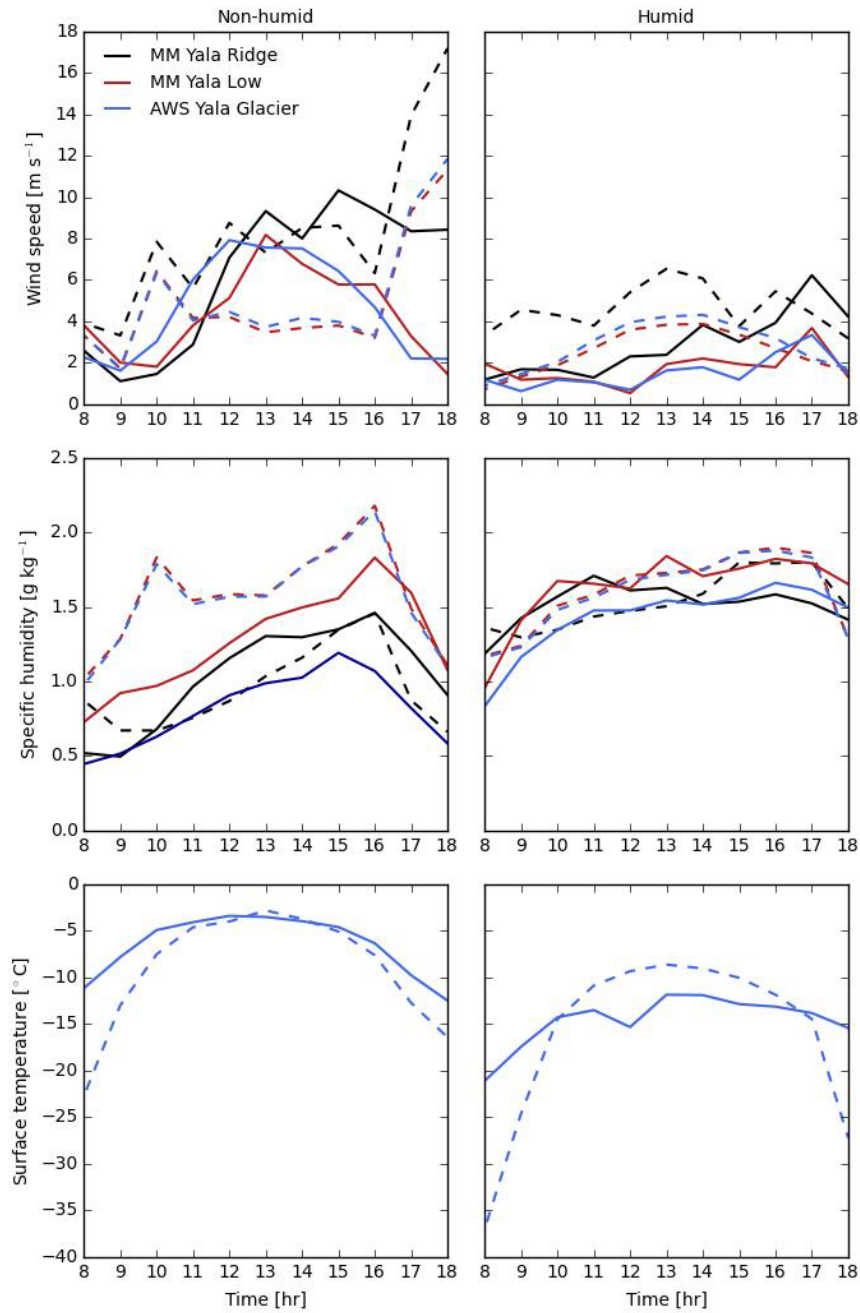


Figure A.1: Validation of wind speed, specific humidity and surface temperature simulated by WRF (dashed lines) with observations from three meteorological stations positioned on the glacier (solid lines) for a humid (1 January 2017) and non-humid day (12 November 2016). Each colour refers to observations/simulations at one of the locations of the on-glacier meteorological stations.

References

- Andreadis, K. M. and D. P. Lettenmaier (2006). Assimilating remotely sensed snow observations into a macroscale hydrology model. *Advances in Water Resources* 29, pp. 872–886. DOI:10.1016/J.ADVWATRES.2005.08.004.
- Armstrong, R. L. et al. (2019). Runoff from glacier ice and seasonal snow in High Asia: separating melt water sources in river flow. *Regional Environmental Change* 19.5, pp. 1249–1261. DOI:10.1007/s10113-018-1429-0.
- Avanzi, F., C. D. Michele, S. Morin, C. M. Carmagnola, A. Ghezzi, and Y. Lejeune (2016). Model complexity and data requirements in snow hydrology: seeking a balance in practical applications. *Hydrological Processes* 30, pp. 2106–2118. DOI:10.1002/HYP.10782.
- Ayala, A., F. Pellicciotti, S. MacDonell, J. McPhee, and P. Burlando (2017a). Patterns of glacier ablation across North-Central Chile: Identifying the limits of empirical melt models under sublimation-favorable conditions. *Water Resources Research* 53, pp. 5601–5625. DOI:10.1002/2016WR020126.
- Ayala, A., F. Pellicciotti, N. Peleg, and P. Burlando (2017b). Melt and surface sublimation across a glacier in a dry environment: distributed energy-balance modelling of Juncal Norte Glacier, Chile. *Journal of Glaciology* 63.241, pp. 803–822. DOI:10.1017/JOG.2017.46.
- Azam, M. F., P. Wagon, C. Vincent, A. L. Ramanathan, V. Favier, A. Mandal, and J. G. Pottakkal (2014). Processes governing the mass balance of Chhota Shigri Glacier (western Himalaya, India) assessed by point-scale surface energy balance measurements. *The Cryosphere* 8.6, pp. 2195–2217. DOI:10.5194/TC-8-2195-2014.
- Baral, P. et al. (2014). Preliminary results of mass-balance observations of Yala Glacier and analysis of temperature and precipitation gradients in Langtang Valley, Nepal. *Annals of Glaciology* 55.66, pp. 9–14. DOI:10.3189/2014AOG66A106.
- Barnett, T. P., J. C. Adam, and D. P. Lettenmaier (2005). Potential impacts of a warming climate on water availability in snow-dominated regions. *Nature* 438.7066, pp. 303–309. DOI:10.1038/NATURE04141.
- Barros, A. P., G. Kim, E. Williams, and S. W. Nesbitt (2004). Probing orographic controls in the Himalayas during the monsoon using satellite imagery. *Natural Hazards and Earth System Sciences* 4.1, pp. 29–51. DOI:10.5194/NHESS-4-29-2004.
- Bartelt, P. and M. Lehning (2002). A physical SNOWPACK model for the Swiss avalanche warning Part I : numerical model. *Cold Regions Science and Technology* 35, pp. 123–145. DOI:10.1016/S0165-232X(02)00074-5.
- Bavay, M., T. Grünewald, and M. Lehning (2013). Response of snow cover and runoff to climate change in high Alpine catchments of Eastern Switzerland. *Advances in Water Resources* 55, pp. 4–16. DOI:10.1016/J.ADVWATRES.2012.12.009.
- Bavay, M., M. Lehning, T. Jonas, and H. Loewe (2009). Simulations of future snow cover and discharge in Alpine headwater catchments. *Hydrological Processes* 23, pp. 95–108. DOI:10.1002/HYP.7195.
- Bayard, D., M. Stähli, A. Parriaux, and H. Flüeler (2005). The influence of seasonally frozen soil on the snowmelt runoff at two Alpine sites in southern Switzerland. *Journal of Hydrology* 309.1-4, pp. 66–84. DOI:10.1016/J.JHYDROL.2004.11.012.
- Bengtsson, L. (1982a). The importance of refreezing on the diurnal snowmelt cycle with application to a northern Swedish catchment. *Nordic Hydrology* 13.1, pp. 1–12. DOI:10.2166/NH.1982.0001.
- Bengtsson, L. (1982b). Percolation of meltwater through a snowpack. *Cold Regions Science and Technology* 6, pp. 73–81. DOI:10.1016/0165-232X(82)90046-5.
- Bernhardt, M. and K. Schulz (2010). SnowSlide: A simple routine for calculating gravitational snow transport. *Geophysical Research Letters* 37.11, pp. 1–6. DOI:10.1029/2010GL043086.
- Bernhardt, M., K. Schulz, G. E. Liston, and G. Zängl (2012). The influence of lateral snow redistribution processes on snow melt and sublimation in alpine regions. *Journal of Hydrology* 424-425, pp. 196–206. DOI:10.1016/J.JHYDROL.2012.01.001.
- Bintanja, R., H. Lilienthal, and H. Tüg (2001). Observations of snowdrift over Antarctic snow and blue-ice surfaces. *Annals of Glaciology* 32, pp. 168–174. DOI:10.3189/172756401781819076.

- Bolch, T. et al. (2019). Status and Change of the Cryosphere in the Extended Hindu Kush Himalaya region. In: *The Hindu Kush Himalaya Assessment*. Springer International Publishing, pp. 209–255. DOI:10.1007/978-3-319-92288-1_7.
- Bookhagen, B. and D. W. Burbank (2010). Toward a complete Himalayan hydrological budget: Spatiotemporal distribution of snowmelt and rainfall and their impact on river discharge. *Journal of Geophysical Research: Earth Surface* 115.3, pp. 1–25. DOI:10.1029/2009JF001426.
- Bowling, L. C., J. W. Pomeroy, and D. P. Lettenmaier (2004). Parameterization of Blowing-Snow Sublimation in a Macroscale Hydrology Model. *Journal of Hydrometeorology* 5, pp. 745–762. DOI:10.1175/1525-7541(2004)005<0745:POBSIA>2.0.CO;2.
- Box, J. E. and K. Steffen (2001). Sublimation on the Greenland ice sheet from automated station observations. *Journal of Geophysical Research* 106.D24, pp. 33965–33981. DOI:10.1029/2001JD900219.
- Brock, B. W., I. C. Willis, and M. J. Sharp (2000). Measurement and parameterisation of albedo variations at Haut Glacier d' Arolla , Switzerland. *Journal of Glaciology* 46.155, pp. 675–688. DOI:10.3189/172756506781828746.
- Brock, B. W., I. C. Willis, and M. J. Sharp (2006). Measurement and parameterization of aerodynamic roughness length variations at Haut Glacier d'Arolla, Switzerland. *Journal of Glaciology* 52.177, pp. 281–297. DOI:10.3189/172756506781828746.
- Brown, M. E. et al. (2014). An integrated modeling system for estimating glacier and snow melt driven streamflow from remote sensing and earth system data products in the Himalayas. *Journal of Hydrology* 519.PB, pp. 1859–1869. DOI:10.1016/J.JHYDROL.2014.09.050.
- Brown, R. D. and P. W. Mote (2009). The response of Northern Hemisphere snow cover to a changing climate. *Journal of Climate* 22.8, pp. 2124–2145. DOI:10.1175/2008JCLI2665.1.
- Brun, E., P. David, M. Sudul, and G. Brunot (1992). A numerical model to simulate snow-cover stratigraphy for operational avalanche forecasting. *Journal of Glaciology* 38.128, pp. 13–22. DOI:10.3189/S0022143000009552.
- Brun, E., E. Martin, V. Simon, C. Gendre, and C. Coleou (1989). An energy and mass model of snow cover suitable for operational avalanche forecasting. *Journal of Glaciology* 35.121, pp. 333–342. DOI:10.3189/S0022143000009254.
- Brun, E., V. Vionnet, A. Boone, B. Decharme, Y. Peings, R. Valette, F. Karbou, and S. Morin (2013). Simulation of Northern Eurasian Local Snow Depth, Mass, and Density Using a Detailed Snowpack Model and Meteorological Reanalyses. *Journal of Hydrometeorology* 14.1, pp. 203–219. DOI:10.1175/JHM-D-12-012.1.
- Brun, F. et al. (2022). Brief communication : Everest South Col Glacier did not thin during the last three decades. *The Cryosphere Discussions* 2018, pp. 1–27. DOI:10.5194/TC-2022-166.
- Charrois, L., E. Cosme, M. Dumont, M. Lafaysse, S. Morin, Q. Libois, and G. Picard (2016). On the assimilation of optical reflectances and snow depth observations into a detailed snowpack model. *The Cryosphere* 10.3, pp. 1021–1038. DOI:10.5194/TC-10-1021-2016.
- Cierco, F. X., F. Naaim-Bouvet, and H. Bellot (2007). Acoustic sensors for snowdrift measurements: How should they be used for research purposes? *Cold Regions Science and Technology* 49.1, pp. 74–87. DOI:10.1016/J.COLDREGIONS.2007.01.002.
- Clark, M. P., A. G. Slater, A. P. Barrett, L. E. Hay, G. J. McCabe, B. Rajagopalan, and G. H. Leavesley (2006). Assimilation of snow covered area information into hydrologic and land-surface models. *Advances in Water Resources* 29, pp. 1209–1221. DOI:10.1016/J.ADVWATRES.2005.10.001.
- Collier, E., T. Mölg, F. Maussion, D. Scherer, C. Mayer, and A. B. G. Bush (2013). High-resolution interactive modelling of the mountain glacier-atmosphere interface: An application over the Karakoram. *The Cryosphere* 7.3, pp. 779–795. DOI:10.5194/TC-7-779-2013.
- Collier, E. and W. W. Immerzeel (2015). High-resolution modeling of atmospheric dynamics in the Nepalese Himalaya. *Journal of Geophysical Research: Atmospheres* 120.19, pp. 9882–9896. DOI:10.1002/2015JD023266.RECEIVED.
- Crawford, C. J., S. M. Manson, M. E. Bauer, and D. K. Hall (2013). Multitemporal snow cover mapping in mountainous terrain for Landsat climate data record development. *Remote Sensing of Environment* 135, pp. 224–233. DOI:10.1016/J.RSE.2013.04.004.
- Cullen, N. J., T. Mölg, G. Kaser, K. Steffen, and D. R. Hardy (2007). Energy-balance model validation on the top of Kilimanjaro, Tanzania, using eddy covariance data. *Annals of Glaciology* 46, pp. 227–233. DOI:10.3189/172756407782871224.
- Dankers, R. and S. De Jong (2004). Monitoring snow-cover dynamics in Northern Fennoscandia with SPOT VEGETATION images. *International Journal of Remote Sensing* 25.15, pp. 2933–2949. DOI:10.1080/01431160310001618374.

- Datt, P., P. K. Srivastava, P. S. Negi, and P. K. Satyawali (2008). Surface energy balance of seasonal snow cover for snow-melt estimation in N-W Himalaya. *Journal of earth system science* 117.5, pp. 567–573.
- Dee, D. P. et al. (2011). The ERA-Interim reanalysis: Configuration and performance of the data assimilation system. *Quarterly Journal of the Royal Meteorological Society* 137.656, pp. 553–597. DOI:10.102/QJ.828.
- Dingman, S. L. (2008). *Physical Hydrology*. 2nd ed. Waveland Press Inc.
- Dong, J., J. P. Walker, and P. R. Houser (2005). Factors affecting remotely sensed snow water equivalent uncertainty. *Remote Sensing of Environment* 97.1, pp. 68–82. DOI:10.1016/J.RSE.2005.04.010.
- Doorschot, J. J. J., M. Lehning, and A. Vrouwe (2004). Field measurements of snow-drift threshold and mass fluxes, and related model simulations. *Boundary-Layer Meteorology* 113.3, pp. 347–368.
- Dozier, J. (1989). Spectral signature of alpine snow cover from the landsat thematic mapper. *Remote Sensing of Environment* 28, pp. 9–22. DOI:10.1016/0034-4257(89)90101-6.
- Dozier, J., T. H. Painter, K. Rittger, and J. E. Frew (2008). Time space continuity of daily maps of fractional snow cover and albedo from MODIS. *Advances in Water Resources* 31.11, pp. 1515–1526. DOI:10.1016/J.ADVWATRES.2008.08.011.
- Durand, M., N. P. Molotch, and S. A. Margulis (2008). Merging complementary remote sensing datasets in the context of snow water equivalent reconstruction. *Remote Sensing of Environment* 112.3, pp. 1212–1225. DOI:10.1016/J.RSE.2007.08.010.
- Etchevers, P., E. Martin, R. Brown, C. Fierz, and Y. Lejeune (2004). Validation of the surface energy budget simulated by several snow models (SnowMIP project). *Annals of Glaciology* 38, pp. 150–158. DOI:10.3189/172756404781814825.
- Evensen, G. (1994). Sequential data assimilation with a nonlinear quasi-geostrophic model using Monte Carlo methods to forecast error statistics. *Journal of Geophysical Research: Oceans* 99.C5, pp. 143–162. DOI:10.1029/94JC00572.
- Feiken, H (2014). Dealing with biases: three archaeological approaches to the hidden landscapes of Italy. PhD thesis, p. 344.
- Fitzpatrick, N., V. Radić, and B. Menounos (2017). Surface Energy Balance Closure and Turbulent Flux Parameterization on a Mid-Latitude Mountain Glacier, Purcell Mountains, Canada. *Frontiers in Earth Science* 5.67, pp. 1–20. DOI:10.3389/FEART.2017.00067.
- Foken, T (2008). The energy balance closure problem : an overview. *Ecological Applications* 18.6, pp. 1351–1367. DOI:10.1890/06-0922.1.
- Förster, K, G Meon, T Marke, and U Strasser (2014). Effect of meteorological forcing and snow model complexity on hydrological simulations in the Sieber catchment (Harz Mountains , Germany). *Hydrology and Earth System Sciences* 18.11, pp. 4703–4720. DOI:10.5194/HESS-18-4703-2014.
- Fujita, K. and Y. Ageta (2000). Effect of summer accumulation on glacier mass balance on the Tibetan Plateau revealed by mass-balance model. *Journal of Glaciology* 46.153, pp. 244–252. DOI:10.3189/172756500781832945.
- Fujita, K. and T. Nuimura (2011). Spatially heterogeneous wastage of Himalayan glaciers. *Proceedings of the National Academy of Sciences of the United States of America* 108.34, pp. 14011–14014. DOI:10.1073/PNAS.1106242108.
- Gascoin, S., M. Grizonnet, M. Bouchet, G. Salgues, and O. Hagolle (2019). Theia Snow collection: High-resolution operational snow cover maps from Sentinel-2 and Landsat-8 data. *Earth System Science Data* 11.2, pp. 493–514. DOI:10.5194/ESSD-11-493-2019.
- Gascoin, S., S. Lhermitte, C. Kinnard, K. Bortels, and G. E. Liston (2013). Wind effects on snow cover in Pascua-Lama, Dry Andes of Chile. *Advances in Water Resources* 55, pp. 25–39. DOI:10.1016/J.ADVWATRES.2012.11.013.
- Girona-Mata, M., E. S. Miles, S. Ragettli, and F. Pellicciotti (2019). High-Resolution Snowline Delineation From Landsat Imagery to Infer Snow Cover Controls in a Himalayan Catchment. *Water Resources Research* 55.8, pp. 6754–6772. DOI:10.1029/2019WR024935.
- Gordon, M., K. Simon, and P. a. Taylor (2006). On snow depth predictions with the Canadian land surface scheme including a parametrization of blowing snow sublimation. *Atmosphere-Ocean* 44.3, pp. 239–255. DOI:10.3137/AO.440303.
- Granger, R. J. and D. H. Male (1978). Melting of a prairie snowpack (Canada). *Journal of Applied Meteorology* 17.2, pp. 1833–1842. DOI:10.1175/1520-0450(1978)017<1833:MOAPS>2.0.CO;2.
- Griessinger, N., M. Schirmer, N. Helbig, A. Winstral, A. Michel, and T. Jonas (2019). Implications of observation-enhanced energy-balance snowmelt simulations for runoff modeling of Alpine catchments. *Advances in Water Resources* 133, p. 103410. DOI:10.1016/J.ADVWATRES.2019.103410

- Groot Zwaaftink, C. D., H. Löwe, R. Mott, M. Bavay, and M. Lehning (2011). Drifting snow sublimation: A high-resolution 3-D model with temperature and moisture feedbacks. *Journal of Geophysical Research Atmospheres* 116.16, pp. 1–14. DOI:10.1029/2011JD015754.
- Groot Zwaaftink, C. D., R. Mott, and M. Lehning (2013). Seasonal simulation of drifting snow sublimation in Alpine terrain. *Water Resources Research* 49.3, pp. 1581–1590. DOI:10.1002/WRCR.20137.
- Grünewald, T. and M. Lehning (2015). Are flat-field snow depth measurements representative? A comparison of selected index sites with areal snow depth measurements at the small catchment scale. *Hydrological Processes* 29.7, pp. 1717–1728. DOI:10.1002/HYP.10295.
- Günther, D., T. Marke, R. Essery, and U. Strasser (2019). Uncertainties in Snowpack Simulations-Assessing the Impact of Model Structure, Parameter Choice, and Forcing Data Error on Point-Scale Energy Balance Snow Model Performance. *Water Resources Research* 55.4, pp. 2779–2800. DOI:10.1029/2018WR023403.
- Gurung, D. R., A. V. Kulkarni, A. Giriraj, K. S. Aung, B. Shrestha, and J. Srinivasan (2011). Changes in seasonal snow cover in Hindu Kush-Himalayan region. *The Cryosphere Discussions* 5.2, pp. 755–777. DOI:10.5194/TCD-5-755-2011.
- Gurung, D. R., B. Maharjan, B. Shrestha, and S. Shrestha (2017). Climate and topographic controls on snow cover dynamics in the Hindu Kush Himalaya. *International journal of climatology* 37.10. DOI:10.1002/JOC.4961.
- Hall, D. K., G. a. Riggs, and V. V. Salomonson (1995). Development of methods for mapping global snow cover using moderate resolution imaging spectroradiometer data. *Remote Sensing of Environment* 54.2, pp. 127–140. DOI:10.1016/0034-4257(95)00137-P.
- Hall, D. K. and G. A. Riggs (2007). Accuracy assessment of the MODIS snow products. *Hydrological Processes* 21.12, pp. 1534–1547. DOI:10.1002/HYP.6715.
- Hall, D. K., G. A. Riggs, V. V. Salomonson, N. E. DiGirolamo, and K. J. Bayr (2002). MODIS snow-cover products. *Remote Sensing of Environment* 83.1-2, pp. 181–194. DOI:10.1016/S0034-4257(02)00095-0.
- Hegdahl, T. J., L. M. Tallaksen, K. Engeland, J. F. Burkhart, and C. Y. Xu (2016). Discharge sensitivity to snowmelt parameterization: A case study for Upper Beas basin in Himachal Pradesh, India. *Hydrology Research* 47.4, pp. 683–700. DOI:10.2166/NH.2016.047.
- Heilig, A., C. Mitterer, L. Schmid, N. Wever, J. Schweizer, H. Marshall, and O. Eisen (2015). Seasonal and diurnal cycles of liquid water in snow - Measurements and modeling. *Journal of Geophysical Research : Earth Surface* 120, pp. 2139–2154. DOI:10.1002/2015JF003593.
- Helgason, W. and J. Pomeroy (2012a). Problems closing the energy balance over a homogeneous snow cover during midwinter. *Journal of Hydrometeorology* 13.2, pp. 557–572. DOI:10.1175/JHM-D-11-0135.1.
- Helgason, W. and J. W. Pomeroy (2012b). Characteristics of the near-surface boundary layer within a mountain valley during winter. *Journal of Applied Meteorology and Climatology* 51.3, pp. 583–597. DOI:10.1175/JAMC-D-11-058.1.
- Herrero, J. and M. J. Polo (2016). Evapotranspiration from the snow in the Mediterranean mountains of Sierra Nevada (Spain). *The Cryosphere* 10, pp. 2981–2998. DOI:10.5194/TC-10-2981-2016.
- Hock, R. (2003). Temperature index melt modelling in mountain areas. *Journal of Hydrology* 282.1-4, pp. 104–115. DOI:10.1016/S0022-1694(03)00257-9.
- Hong, S.-Y., Y. Noh, and J. Dudhia (2006). A New Vertical Diffusion Package with an Explicit Treatment of Entrainment Processes. *Monthly Weather Review* 134.9, pp. 2318–2341. DOI:10.1175/MWR3199.1.
- Hopfinger, E. J. (1983). Snow Avalanche Motion and Related Phenomena. *Annual Review of Fluid Mechanics* 15, pp. 47–76. DOI:10.1146/ANNUREV.FL.15.010183.000403.
- Hüsler, F., T. Jonas, S. Wunderle, and S. Albrecht (2012). Validation of a modified snow cover retrieval algorithm from historical 1-km AVHRR data over the European Alps. *Remote Sensing of Environment* 121, pp. 497–515. DOI:10.1016/J.RSE.2012.02.018.
- Iacono, M. J., J. S. Delamere, E. J. Mlawer, M. W. Shephard, S. A. Clough, and W. D. Collins (2008). Radiative forcing by long-lived greenhouse gases: Calculations with the AER radiative transfer models. *Journal of Geophysical Research Atmospheres* 113.13, pp. 2–9. DOI:10.1029/2008JD009944.
- Immerzeel, W. W., P. Droogers, S. M. de Jong, and M. F. P. Bierkens (2009). Large-scale monitoring of snow cover and runoff simulation in Himalayan river basins using remote sensing. *Remote Sensing of Environment* 113.1, pp. 40–49. DOI:10.1016/J.RSE.2008.08.010.
- Immerzeel, W. W., F. Pellicciotti, and M. F. P. Bierkens (2013). Rising river flows throughout the twenty-first century in two Himalayan glacierized watersheds. *Nature Geoscience* 6.9, pp. 742–745. DOI:10.1038/NNGEO1896.

- Immerzeel, W. W., L. P. H. van Beek, M. Konz, A. B. Shrestha, and M. F. P. Bierkens (2012). Hydrological response to climate change in a glacierized catchment in the Himalayas. *Climatic Change* 110.3-4, pp. 721–736. DOI:10.1007/s10584-011-0143-4.
- Immerzeel, W. W., L. P. H. van Beek, and M. F. P. Bierkens (2010). Climate change will affect the Asian water towers. *Science* 328.5984, pp. 1382–5. DOI:10.1126/SCIENCE.1183188.
- Immerzeel, W., L. Petersen, S. Ragetti, and F. Pellicciotti (2014). The importance of observed gradients of air temperature and precipitation for modeling runoff from a glacierized watershed in the Nepalese Himalayas. *Water Resources Research* 50.3, pp. 2212–2226. DOI:10.1002/2013WR014506.
- Jeelani, G., J. J. Feddema, C. J. Van Der Veen, and L. Stearns (2012). Role of snow and glacier melt in controlling river hydrology in Liddar watershed (western Himalaya) under current and future climate. *Water Resources Research* 48.12, pp. 1–16. DOI:10.1029/2011WR011590.
- Jennings, K. S., T. G. F. Kittel, and N. P. Molotch (2018). Observations and simulations of the seasonal evolution of snowpack cold content and its relation to snowmelt and the snowpack energy budget. *The Cryosphere* 12, pp. 1595–1614. DOI:10.5194/TC-12-1595-2018.
- Kain, J. S. (2004). The KainFritsch Convective Parameterization: An Update. *Journal of Applied Meteorology* 43.1, pp. 170–181. DOI:10.1175/1520-0450(2004)043<0170:TKCPAU>2.0.CO;2.
- Karssenber, D., O. Schmitz, P. Salamon, K. de Jong, and M. F. P. Bierkens (2010). A software framework for construction of process-based stochastic spatio-temporal models and data assimilation. *Environmental Modelling and Software* 25.4, pp. 489–502. DOI:10.1016/J.ENVSFT.2009.10.004.
- Kaspari, S., R. L. B. Hooke, P. A. Mayewski, S. Kang, S. Hou, and D. Qin (2008). Snow accumulation rate on Qomolangma (Mount Everest), Himalaya: Synchronicity with sites across the Tibetan Plateau on 50-100 year timescales. *Journal of Glaciology* 54.185, pp. 343–352. DOI:10.3189/002214308784886126.
- Kaspari, S. et al. (2007). Reduction in northward incursions of the South Asian monsoon since 1400 AD inferred from a Mt. Everest ice core. *Geophysical Research Letters* 34.16. DOI:10.1029/2007GL030440.
- Kayastha, R. B., T. Ohata, and Y. Ageta (1999). Application of a mass-balance model to a Himalayan glacier. *Journal of Glaciology* 45.151, pp. 559–567. DOI:10.3189/S002214300000143X.
- Kinar, N. J. and J. W. Pomeroy (2015). SAS2 : the system for acoustic sensing of snow. *Hydrological Processes* 29.18, pp. 4032–4050. DOI:10.1002/HYP.10535.
- Kirkham, J. D., I. Koch, T. M. Saloranta, M. Litt, E. E. Stigter, K. Møen, A. Thapa, K. Melvold, and W. W. Immerzeel (2019). Near Real-Time Measurement of Snow Water Equivalent in the Nepal Himalayas. *Frontiers in Earth Science* 7, July, pp. 1–18. DOI:10.3389/FEART.2019.00177.
- Klein, A. G. and A. C. Barnett (2003). Validation of daily MODIS snow cover maps of the Upper Rio Grande River Basin for the 2000-2001 snow year. *Remote Sensing of Environment* 86.2, pp. 162–176. DOI:10.1016/S0034-4257(03)00097-X.
- Knowles, J. F., P. D. Blanken, M. W. Williams, and K. M. Chowanski (2012). Energy and surface moisture seasonally limit evaporation and sublimation from snow-free alpine tundra. *Agricultural and Forest Meteorology* 157, pp. 106–115. DOI:10.1016/J.AGRFORMET.2012.01.017.
- Kobierska, F., T. Jonas, M. Zappa, M. Bavay, J. Magnusson, and S. M. Bernasconi (2013). Future runoff from a partly glacierized watershed in Central Switzerland : A two-model approach. *Advances in Water Resources* 55, pp. 204–214. DOI:10.1016/J.ADVWATRES.2012.07.024.
- Koch, F., P. Henkel, F. Appel, L. Schmid, H. Bach, M. Lamm, M. Prasch, J. Schweizer, and W. Mauser (2019). Retrieval of Snow Water Equivalent, Liquid Water Content, and Snow Height of Dry and Wet Snow by Combining GPS Signal Attenuation and Time Delay. *Water Resources Research* 55.5, pp. 4465–4487. DOI:10.1029/2018WR024431.
- Kok, R. J., J. F. Steiner, M. Litt, P. Wagnon, I. Koch, M. F. Azam, and W. W. Immerzeel (2019). Measurements, models and drivers of incoming longwave radiation in the Himalaya. *International Journal of Climatology* 40.2, pp. 942–956. DOI:10.1002/JOC.6249.
- Kraaijenbrink, P. D., E. E. Stigter, T. Yao, and W. W. Immerzeel (2021). Climate change decisive for Asia's snow meltwater supply. *Nature Climate Change* 11.7, pp. 591–597. DOI:10.1038/s41558-021-01074-x.
- Krinner, G. et al. (2018). ESM-SnowMIP: Assessing snow models and quantifying snow-related climate feedbacks. *Geoscientific Model Development* 11.12, pp. 5027–5049. DOI:10.5194/GMD-11-5027-2018.
- Kuchment, L. and A. Gelfan (1996). The determination of the snowmelt rate and the meltwater outflow from a snowpack for modelling river runoff generation. *Journal of Hydrology* 179.1-4, pp. 23–36. DOI:10.1016/0022-1694(95)02878-1.

- Lalande, M., M. Ménégoz, G. Krinner, K. Naegeli, and S. Wunderle (2021). Climate change in the High Mountain Asia in CMIP6. *Earth System Dynamics* 12.4, pp. 1061–1098. DOI:10.5194/ESD-12-1061-2021.
- Lehning, M. and C. Fierz (2008). Assessment of snow transport in avalanche terrain. *Cold Regions Science and Technology* 51.2, pp. 240–252. DOI:10.1016/J.COLDREGIONS.2007.05.012.
- Lehning, M., I Völksch, D Gustafsson, T. A. Nquyen, M Stähli, and M Zappa (2006). ALPINE3D: a detailed model of mountain surface processes and its application to snow hydrology. *Hydrological Processes* 20.10, pp. 2111–2128. DOI:10.1002/HYP.6204.
- Leisenring, M. and H. Moradkhani (2011). Snow water equivalent prediction using Bayesian data assimilation methods. *Stochastic Environmental Research and Risk Assessment* 25.2, pp. 253–270. DOI:10.1007/s00477-010-0445-5.
- Lievens, H., I. Brangers, H. P. Marshall, T. Jonas, M. Olefs, and G. de Lannoy (2022). Observing Snow Depth At Sub-Kilometer Resolution Over the European Alps From Sentinel-1. *The Cryosphere* 16, pp. 159–177. DOI:10.5194/TC-16-159-2022.
- Lievens, H., M. Demuzere, H.-p. Marshall, R. H. Reichle, I. Brangers, P. D. Rosnay, M. Dumont, M. Giroto, and W. Walter (2019). Snow depth variability in the Northern Hemisphere mountains observed from space. *Nature Communications* 10.4629, pp. 1–33. DOI:10.1038/s41467-019-12566-Y.
- Liston, G. E. and K. Elder (2006). A Distributed Snow-Evolution Modeling System (SnowModel). *Journal of Hydrometeorology* 7.6, pp. 1259–1276. DOI:10.1175/JHM548.1.
- Litt, M., J. E. Sicart, and W. Helgason (2015). A study of turbulent fluxes and their measurement errors for different wind regimes over the tropical Zongo Glacier (16 S) during the dry season. *Atmospheric Measurement Techniques* 8, pp. 3229–3250. DOI:10.5194/AMT-8-3229-2015.
- Litt, M., J. Shea, P. Wagnon, J. Steiner, I. Koch, E. Stigter, and W. Immerzeel (2019). Glacier ablation and temperature indexed melt models in the Nepalese Himalaya. *Scientific Reports* 9.1, pp. 1–13. DOI:10.1038/s41598-019-41657-5.
- Litt, M., J. E. Sicart, W. D. Helgason, and P. Wagnon (2014). Turbulence Characteristics in the Atmospheric Surface Layer for Different Wind Regimes over the Tropical Zongo Glacier (Bolivia, 16 S). *Boundary-Layer Meteorology* 154.3, pp. 471–495. DOI:10.1007/s10546-014-9975-6.
- Liu, Y., C. D. Peters-Lidard, S. Kumar, J. L. Foster, M. Shaw, Y. Tian, and G. M. Fall (2013). Assimilating satellite-based snow depth and snow cover products for improving snow predictions in Alaska. *Advances in Water Resources* 54, pp. 208–227. DOI:10.1016/J.ADVWATRES.2013.02.005.
- Lundquist, J. D. and F. Lott (2008). Using inexpensive temperature sensors to monitor the duration and heterogeneity of snow-covered areas. *Water Resources Research* 44.4. DOI:10.1029/2008WR007035.
- Lutz, A. F., W. W. Immerzeel, A. B. Shrestha, and M. F. P. Bierkens (2014). Consistent increase in High Asia's runoff due to increasing glacier melt and precipitation. *Nature Climate Change* 4.7, pp. 587–592. DOI:10.1038/NCLIMATE2237.
- Lutz, A., W. Immerzeel, M. Litt, S. Bajracharya, and A. Shrestha (2015). *Comprehensive Review of Climate Change and the Impacts on Cryosphere, Hydrological Regimes and Glacier Lakes*. Tech. rep., pp. 1–89.
- Lutz, A. F., W. W. Immerzeel, P. D. Kraaijenbrink, and A. B. Shrestha (2016). Climate change impacts on the upper Indus hydrology: sources, shifts and extremes. *PLOS one* 11.11, pp. 1–33. DOI:10.1371/JOURNAL.PONE.0165630.
- MacDonald, M. K., J. W. Pomeroy, and A. Pietroniro (2009). Parameterizing redistribution and sublimation of blowing snow for hydrological models: tests in a mountainous subarctic catchment. *Hydrological Processes* 23.18, pp. 2570–2583. DOI:10.1002/HYP7356.
- MacDonald, M. K., J. W. Pomeroy, and A. Pietroniro (2010). On the importance of sublimation to an alpine snow mass balance in the Canadian Rocky Mountains. *Hydrology and Earth System Sciences* 14.7, pp. 1401–1415. DOI:10.5194/HESS-14-1401-2010.
- Magnusson, J., D. Farinotti, T. Jonas, and M. Bavay (2011). Quantitative evaluation of different hydrological modelling approaches in a partly glacierized Swiss watershed. *Hydrological Processes* 25.13, pp. 2071–2084. DOI:10.1002/HYP.7958.
- Magnusson, J., N. Wever, R. Essery, N. Helbig, A. Winstral, and T. Jonas (2015). Evaluating snow models with varying process representations for hydrological applications: Snow model evaluation. *Water Resources Research* 51.4, pp. 2707–2723. DOI:10.1002/2014WR016498.
- Magnusson, J., A. Winstral, A. S. Stordal, R. Essery, and T. Jonas (2016). Improving physically based snow simulations by assimilating snow depths using the particle filter. *Water Resources Research* 53.2, pp. 1125–1143. DOI:10.1002/2016WR019092.
- Mahrt, L. and D. Vickers (2005). Moisture fluxes over snow with and without protruding vegetation. *Quarterly Journal of the Royal Meteorological Society* 131.607, pp. 1251–1270. DOI:10.1256/QJ.04.6.6.

- Mandal, A., T. Angchuk, M. F. Azam, A. Ramanathan, P. Wagnon, M. Soheb, and C. Singh (2022). An 11-year record of wintertime snow-surface energy balance and sublimation at 4863 m a.s.l. on the Chhota Shigri Glacier moraine (western Himalaya, India). *The Cryosphere* 16.9, pp. 3775–3799. DOI:10.5194/TC-16-3775-2022.
- Marin, C., G. Bertoldi, V. Premier, M. Callegari, C. Brida, K. Hürkamp, J. Tschiersch, M. Zebisch, and C. Notarnicola (2020). Use of Sentinel-1 radar observations to evaluate snowmelt dynamics in alpine regions. *The Cryosphere* 14.3, pp. 935–956. DOI:10.5194/TC-14-935-2020.
- Marks, D., A. Winstal, M. Reba, J. Pomeroy, and M. Kumar (2013). An evaluation of methods for determining during-storm precipitation phase and the rain / snow transition elevation at the surface in a mountain basin. *Advances in Water Resources* 55, pp. 98–110. DOI:10.1016/J.ADVWATRES.2012.11.012.
- Marks, D., J. Domingo, D. Susong, T. Link, and D. Garen (1999). A spatially distributed energy balance snowmelt model for application in mountain basins. *Hydrological Processes* 13.12-13, pp. 1935–1959. DOI:10.1002/(SICI)1099-1085(199909)13:12/13<1935::AID-HYP868>3.0.CO;2-C.
- Marks, D. and J. Dozier (1992). Climate and energy exchange at the snow surface in the Alpine Region of the Sierra Nevada: 2. Snow cover energy balance. *Water Resources Research* 28.11, pp. 3043–3054. DOI:10.1029/92WR01483.
- Marsh, P. and M. K. Woo (1984). Wetting front advance and freezing of meltwater within a snow cover: 1. Observations in the Canadian Arctic. *Water Resources Research* 20.12, pp. 1853–1864. DOI:10.1029/WR020i012p01853.
- Maskey, S., S. Uhlenbrook, and S. Ojha (2011). An analysis of snow cover changes in the Himalayan region using MODIS snow products and in-situ temperature data. *Climatic Change* 108.1, pp. 391–400. DOI:10.1007/s10584-011-0181-y.
- Massman, W. J. (2000). A simple method for estimating frequency response corrections for eddy covariance systems. *Agricultural and Forest Meteorology* 104.3, pp. 185–198. DOI:10.1016/S0168-1923(00)00164-7.
- Matiu, M. et al. (2021). Observed snow depth trends in the European Alps: 1971 to 2019. *The Cryosphere* 15.3, pp. 1343–1382. DOI:10.5194/TC-15-1343-2021.
- Matthews, T. et al. (2020). Going to Extremes: Installing the World’s Highest Weather Stations on Mount Everest. *Bulletin of the American Meteorological Society* 101.11, E1870–E1890. DOI:10.1175/BAMS-D-19-0198.1.
- Mauder, M. and T. Foken (2004). *Documentation and Instruction Manual of the Eddy Covariance Software Package TK2*. Tech. rep. Bayreuth: University of Bayreuth.
- Ménégoz, M., H. Gallée, and H. W. Jacobi (2013). Precipitation and snow cover in the Himalaya: From reanalysis to regional climate simulations. *Hydrology and Earth System Sciences* 17.10, pp. 3921–3936. DOI:10.5194/HESS-17-3921-2013.
- Mishra, B., M. S. Babel, and N. K. Tripathi (2014). Analysis of climatic variability and snow cover in the Kaligandaki River Basin, Himalaya, Nepal. *Theoretical and Applied Climatology* 116.3-4, pp. 681–694. DOI:10.1007/s00704-013-0966-1.
- Mitterer, C., H. Hirashima, and J. Schweizer (2011). Wet-snow instabilities: Comparison of measured and modelled liquid water content and snow stratigraphy. *Annals of Glaciology* 52.58, pp. 201–208. DOI:10.3189/172756411797252077.
- Mölg, T., F. Maussion, W. Yang, and D. Scherer (2012). The footprint of Asian monsoon dynamics in the mass and energy balance of a Tibetan glacier. *The Cryosphere* 6.6, pp. 1445–1461. DOI:10.5194/TC-6-1445-2012.
- Molotch, N. P. (2009). Reconstructing snow water equivalent in the Rio Grande headwaters using remotely sensed snow cover data and a spatially distributed snowmelt model. *Hydrological Processes* 23.7, pp. 1076–1089. DOI:10.1002/HYP.7206.
- Molotch, N. P., P. D. Blanken, M. W. Williams, A. A. Turnipseed, R. K. Monson, and S. A. Margulis (2007). Estimating sublimation of intercepted and sub-canopy snow using eddy covariance systems. *Hydrological Processes* 21.12, pp. 1567–1575. DOI:10.1002/HYP.6719.
- Molotch, N. P. and S. A. Margulis (2008). Estimating the distribution of snow water equivalent using remotely sensed snow cover data and a spatially distributed snowmelt model: A multi-resolution, multi-sensor comparison. *Advances in Water Resources* 31.11, pp. 1503–1514. DOI:10.1016/J.ADVWATRES.2008.07.017.
- Morrison, H., G. Thompson, and V. Tatarskii (2009). Impact of Cloud Microphysics on the Development of Trailing Stratiform Precipitation in a Simulated Squall Line: Comparison of One- and Two-Moment Schemes. *Monthly Weather Review* 137.3, pp. 991–1007. DOI:10.1175/2008MWR2556.1.

- Mott, R., L. Egli, T. Grünewald, N. Dawes, C. Manes, M. Bavay, and M. Lehning (2011). Micrometeorological processes driving snow ablation in an Alpine catchment. *The Cryosphere* 5.4, pp. 1083–1098. DOI:10.5194/TC-5-1083-2011.
- Mott, R., M. Daniels, and M. Lehning (2015). Atmospheric flow development and associated changes in turbulent sensible heat flux over a patchy mountain snow cover. *Journal of Hydrometeorology* 16.3, pp. 1315–1340. DOI:10.1175/JHM-D-14-0036.1.
- Mott, R. and M. Lehning (2010). Meteorological modeling of very high-resolution wind fields and snow deposition for mountains. *Journal of Hydrometeorology* 11.4, pp. 934–949. DOI:10.1175/2010JHM1216.1.
- Nagler, T., H. Rott, P. Malcher, and F. Müller (2008). Assimilation of meteorological and remote sensing data for snowmelt runoff forecasting. *Remote Sensing of Environment* 112.4, pp. 1408–1420. DOI:10.1016/j.rse.2007.07.006.
- Nakai, Y., T. Sakamoto, T. Terajima, H. Kitahara, and T. Saito (1994). Snow interception by forest canopies: weighing a conifer tree, meteorological observation and analysis by the Penman-Monteith formula. In: *Snow and Ice Covers: Interactions with the Atmosphere Ecosystems*. 223. Yokohama, pp. 227–236.
- Niu, G. Y. et al. (2011). The community Noah land surface model with multiparameterization options (Noah-MP): 1. Model description and evaluation with local-scale measurements. *Journal of Geophysical Research Atmospheres* 116.12, pp. 1–19. DOI:10.1029/2010JD015139.
- Noh, M.-j. and I. M. Howat (2015). Automated stereo-photogrammetric DEM generation at high latitudes : Surface Extraction with TIN-based Search-space Minimization (SETSM) validation and demonstration over glaciated regions. *GIScience & Remote Sensing* 52.2, pp. 198–217. DOI:10.1080/15481603.2015.1008621.
- Ohata, T., K. Higuchi, K. Ikegami, B. T. Ohata, K. Higuchi, and K. Ikegami (1981). Mountain-Valley Wind System in the Khumbu Himal, East Nepal. *Journal of the Meteorological Society of Japan. Ser. II* 59.5, pp. 753–762. DOI:10.2151/JMSJ1965.59.5_753.
- Palazzi, E., J. Von Hardenberg, and A. Provenzale (2013). Precipitation in the hindu-kush karakoram himalaya: Observations and future scenarios. *Journal of Geophysical Research Atmospheres* 118.1, pp. 85–100. DOI:10.1029/2012JD018697.
- Pan, X., W. Helgason, A. Ireson, and H. Wheeler (2017). Field-scale water balance closure in seasonally frozen conditions. *Hydrology and Earth System Sciences* 21.11, pp. 5401–5413. DOI:10.5194/hess-21-5401-2017.
- Panday, P. K., K. E. Frey, and B. Ghimire (2011). Detection of the timing and duration of snowmelt in the Hindu Kush-Himalaya using QuikSCAT, 2000-2008. *Environmental Research Letters* 6.2, pp. 2000–2008. DOI:10.1088/1748-9326/6/2/024007.
- Parajka, J. and G. Blöschl (2006). Validation of MODIS snow cover images over Austria. *Hydrology and Earth System Sciences* 10.5, pp. 679–689. DOI:10.5194/hess-10-679-2006.
- Paulson, C. A. (1970). The mathematical representation of wind speed and temperature profiles in the unstable atmospheric surface layer. *Journal of Applied Meteorology* 9.6, pp. 857–861. DOI:10.1175/1520-0450(1970)009<0857:TMROWS>2.0.CO;2.
- Pellicciotti, F., B. Broock, U. Strasser, P. Burlando, M. Funk, and J. Corripio (2005). An enhanced temperature-index glacier melt model including the shortwave radiation balance: Development and testing for Haut Glacier d’Arolla, Switzerland. *Journal of Glaciology* 51.175, pp. 573–587. DOI:10.3189/172756505781829124.
- Pellicciotti, F., C. Buergi, W. W. Immerzeel, M. Konz, and A. B. Shrestha (2012). Challenges and Uncertainties in Hydrological Modeling of Remote Hindu KushKarakoramHimalayan (HKH) Basins: Suggestions for Calibration Strategies. *Mountain Research and Development* 32.1, pp. 39–50. DOI:10.1659/MRD-JOURNAL-D-11-00092.1.
- Pellicciotti, F., J. Helbing, A. Rivera, V. Favier, J. Corripio, J. Araos, J. E. Sicart, and M. Carenzo (2008). A study of the energy balance and melt regime on Juncal Norte Glacier, semi-arid Andes of central Chile, using melt models of different complexity. *Hydrological Processes* 22.19, pp. 3980–3997. DOI:10.1002/HYP.7085.
- Pfeffer, W. T. and N. F. Humphrey (1998). Formation of ice layers by infiltration and refreezing of melt-water. *Annals of Glaciology* 26, pp. 83–91. DOI:10.3189/1998AOG26-1-83-91.
- Pfeffer, W. T., M. F. Meier, and T. H. Illangasekare (1991). Retention of Greenland runoff by refreezing: implications for projected future sea level change. *Journal of Geophysical Research* 96.C12, pp. 0148–0227. DOI:10.1029/91Jc02502.
- Pohl, S., P. Marsh, and G. E. Liston (2006). Spatial-Temporal Variability in Turbulent Fluxes during Spring Snowmelt. *Arctic, Antarctic, and Alpine Research* 38.1, pp. 136–146. DOI:10.1657/1523-0430(2006)038[0136:SVITFD]2.0.CO;2.

- Pomeroy, J. W. and L Li (2000). Prairie and arctic areal snow cover mass balance using a blowing snow model. *Journal of Geophysical Research* 105.D21, pp. 26619–26634. DOI:10.1029/2000JD900149.
- Potocki, M. et al. (2022). Mt. Everest's highest glacier is a sentinel for accelerating ice loss. *npj Climate and Atmospheric Science* 5.1, pp. 1–8. DOI:10.1038/s41612-022-00230-0.
- Potter, E. R., A. Orr, I. C. Willis, D. Bannister, and F. Salerno (2018). Dynamical Drivers of the Local Wind Regime in a Himalayan Valley. *Journal of Geophysical Research: Atmospheres* 123.23, pp. 13186–13202. DOI:10.1029/2018JD029427.
- Pritchard, D. M., N. Forsythe, G. O'Donnell, H. J. Fowler, and N. Rutter (2020). Multi-physics ensemble snow modelling in the western Himalaya. *The Cryosphere* 14.4, pp. 1225–1244. DOI:10.5194/TC-14-1225-2020.
- Putkonen, J. K. (2004). Continuous snow and rain data at 500 to 4400 m altitude near Annapurna, Nepal, 1999–2001. *Arctic, Antarctic, and Alpine Research* 36.2, pp. 244–248. DOI:10.1657/1523-0430(2004)036[0244:CSARDA]2.0.CO;2.
- Radic, V., B. Menounos, J. Shea, N. Fitzpatrick, M. A. Tessema, and S. J. Déry (2017). Evaluation of different methods to model near-surface turbulent fluxes for a mountain glacier in the Cariboo Mountains, BC, Canada. *The Cryosphere* 11.6, pp. 2897–2918. DOI:10.5194/TC-11-2897-2017.
- Ragetti, S., F. Pellicciotti, R. Bordoy, and W. W. Immerzeel (2013). Sources of uncertainty in modeling the glaciohydrological response of a Karakoram watershed to climate change. *Water Resources Research* 49.9, pp. 6048–6066. DOI:10.1002/WRCR.20450. arXiv: Ragetti2013.
- Ragetti, S. et al. (2015). Unraveling the hydrology of a Himalayan catchment through integration of high resolution in situ data and remote sensing with an advanced simulation model. *Advances in Water Resources* 78, pp. 94–111. DOI:10.1016/J.ADVWATRES.2015.01.013.
- Rai, R. K., L. K. Berg, B. Kosovic, J. D. Mirocha, M. S. Pekour, and W. J. Shaw (2017). Comparison of Measured and Numerically Simulated Turbulence Statistics in a Convective Boundary Layer Over Complex Terrain. *Boundary-Layer Meteorology* 163.1, pp. 69–89. DOI:10.1007/s10546-016-0217-Y.
- Reba, M. L., T. E. Link, D. Marks, and J. Pomeroy (2009). An assessment of corrections for eddy covariance measured turbulent fluxes over snow in mountain environments. *Water Resources Research* 45.4, pp. 1–15. DOI:10.1029/2008WR007045.
- Reba, M. L., J. Pomeroy, D. Marks, and T. E. Link (2012). Estimating surface sublimation losses from snowpacks in a mountain catchment using eddy covariance and turbulent transfer calculations. *Hydrological Processes* 26.24, pp. 3699–3711. DOI:10.1002/HYP.8372.
- Reijmer, C. H., M. R. Van Den Broeke, X. Fettweis, J. Ettema, and L. B. Stap (2012). Refreezing on the Greenland ice sheet: A comparison of parameterizations. *The Cryosphere* 6.4, pp. 743–762. DOI:10.5194/TC-6-743-2012.
- Rohrer, M., N. Salzmann, M. Stoffel, and A. V. Kulkarni (2013). Missing (in-situ) snow cover data hampers climate change and runoff studies in the Greater Himalayas. *Science of the Total Environment* 468-469, S60–S70. DOI:10.1016/J.SCITOTENV.2013.09.056.
- Saloranta, T. M. (2012). Simulating snow maps for Norway: Description and statistical evaluation of the seNorge snow model. *The Cryosphere* 6.6, pp. 1323–1337. DOI:10.5194/TC-6-1323-2012.
- Saloranta, T. M. (2014). Simulating more accurate snow maps for Norway with MCMC parameter estimation method. *The Cryosphere Discussions* 8.2, pp. 1973–2003. DOI:10.5194/TC-D-8-1973-2014.
- Saloranta, T., A. Thapa, J. D. Kirkham, I. Koch, K. Melvold, E. E. Stigter, M. Litt, and K. Møen (2019). A Model Setup for Mapping Snow Conditions in High-Mountain Himalaya. *Frontiers in Earth Science* 7, p. 129. DOI:10.3389/FEART.2019.00129.
- Saloranta, T. M. (2016). Operational snow mapping with simplified data assimilation using the seNorge snow model. *Journal of Hydrology* 538, pp. 314–325. DOI:10.1016/J.JHYDROL.2016.03.061.
- Samimi, S. and S. J. Marshall (2017). Diurnal Cycles of Meltwater Percolation, Refreezing, and Drainage in the Supraglacial Snowpack of Haig Glacier, Canadian Rocky Mountains. *Frontiers in Earth Science* 5, pp. 1–15. DOI:10.3389/FEART.2017.00006.
- Sauter, T., A. Arndt, and C. Schneider (2020). COSIPY v1.3 - an open-source coupled snowpack and ice surface energy and mass balance model. *Geoscientific Model Development* 13.11, pp. 5645–5662. DOI:10.5194/GMD-13-5645-2020.
- Schlögl, S., M. Lehning, and R. Mott (2018). How are turbulent sensible heat fluxes and snow melt rates affected by a changing snow cover fraction? *Frontiers in Earth Science* 6, pp. 1–13. DOI:10.3389/FEART.2018.00154.
- Schlögl, S., M. Lehning, K. Nishimura, H. Huwald, N. J. Cullen, and R. Mott (2017). How do Stability Corrections Perform in the Stable Boundary Layer Over Snow? *Boundary-Layer Meteorology* 165.1, pp. 161–180. DOI:10.1007/s10546-017-0262-1.

- Schmucki, E., C. Marty, C. Fierz, and M. Lehning (2015). Simulations of 21st century snow response to climate change in Switzerland from a set of RCMs. *International Journal of Climatology* 35.11, pp. 3262–3273. DOI:10.1002/JOC.4205.
- Serreze, M. C., M. P. Clark, R. L. Armstrong, D. A. McGinnis, and R. S. Pulwarty (1999). Characteristics of the western United States snowpack from snowpack telemetry (SNOTEL) data. *Water Resources Research* 35.7, pp. 2145–2160. DOI:10.1029/1999WR900090.
- Sexstone, G. A., D. W. Clow, S. R. Fassnacht, G. E. Liston, C. A. Hiemstra, J. F. Knowles, and C. A. Penn (2018). Snow Sublimation in Mountain Environments and Its Sensitivity to Forest Disturbance and Climate Warming. *Water Resources Research* 54.2, pp. 1191–1211. DOI:10.1002/2017WR021172.
- Sexstone, G. A., D. W. Clow, D. I. Stannard, and S. R. Fassnacht (2016). Comparison of methods for quantifying surface sublimation over seasonally snow-covered terrain. *Hydrological Processes* 30.19, pp. 3373–3389. DOI:10.1002/HYP.10864.
- Shea, J. M., W. W. Immerzeel, P. Wagnon, C. Vincent, and S. Bajracharya (2015a). Modelling glacier change in the Everest region, Nepal Himalaya. *The Cryosphere* 9.3, pp. 1105–1128. DOI:10.5194/TC-9-1105-2015.
- Shea, J. M., P. Wagnon, W. W. Immerzeel, R. Biron, F. Brun, and F. Pellicciotti (2015b). A comparative high-altitude meteorological analysis from three catchments in the Nepalese Himalaya. *International Journal of Water Resources Development* 31.2, pp. 174–200. DOI:10.1080/07900627.2015.1020417.
- Shook, K. and D. M. Gray (1997). Snowmelt resulting from advection. *Hydrological Processes* 11.13, pp. 1725–1736. DOI:10.1002/(SICI)1099-1085(19971030)11:13<1725::AID-HYP601>3.0.CO;2-P.
- Simpson, J. J., J. R. Stitt, and M. Sienko (1998). Improved estimates of the areal extent of snow cover from AVHRR data. *Journal of Hydrology* 204.1-4, pp. 1–23. DOI:10.1016/S0022-1694(97)00087-5.
- Singh, P. and L. Bengtsson (2004). Hydrological sensitivity of a large Himalayan basin to climate change. *Hydrological Processes* 18.13, pp. 2363–2385. DOI:10.1002/HYP.1468.
- Singh, P. and S. K. Jain (2003). Modelling of streamflow and its components for a large Himalayan basin with predominant snowmelt yields. *Hydrological Sciences Journal* 48.2, pp. 257–276. DOI:10.1623/HYSJ.48.2.257.44693.
- Skamarock, W. C. and J. B. Klemp (2008). A time-split nonhydrostatic atmospheric model for weather research and forecasting applications. *Journal of Computational Physics* 227.7, pp. 3465–3485. DOI:10.1016/J.JCP.2007.01.037.
- Smeets, C., P. Duynkerke, and H. Vugts (1998). Turbulence characteristics of the stable boundary layer over a mid-latitude glacier. Part I: A combination of katabatic and large scale forcing conditions. *Boundary-Layer Meteorology* 87.1, pp. 117–145. DOI:10.1023/A:1002738407295.
- Smith, T. and B. Bookhagen (2018). Changes in seasonal snow water equivalent distribution in high mountain Asia (1987 to 2009). *Science Advances* 4.1. DOI:10.1126/SCIADV.1701550.
- Smith, T. and B. Bookhagen (2020). Assessing Multi-Temporal Snow-Volume Trends in High Mountain Asia From 1987 to 2016 Using High-Resolution Passive Microwave Data. *Frontiers in Earth Science* 8, pp. 1–13. DOI:10.3389/FEART.2020.559175.
- Smith, T., B. Bookhagen, and A. Rheinwalt (2017). Spatiotemporal patterns of High Mountain Asia's snowmelt season identified with an automated snowmelt detection algorithm, 1987-2016. *The Cryosphere* 11.5, pp. 2329–2343. DOI:10.5194/TC-11-2329-2017.
- Soheb, M., A. Ramanathan, A. Mandal, T. Angchuk, N. Pandey, and S. D. Mishra (2018). Wintertime surface energy balance of a high-altitude seasonal snow surface in Chhota Shigri glacier basin, Western Himalaya. *Geological Society, London, Special Publications* 462.1, pp. 155–168. DOI:10.1144/SP462.10.
- Sorteberg, H. K., R. V. Engeset, and H. C. Udnæs (2001). A national network for snow monitoring in Norway: Snow pillow verification using observations and models. *Physics and Chemistry of the Earth, Part C: Solar, Terrestrial and Planetary Science* 26.10-12, pp. 723–729. DOI:10.1016/S1464-1917(01)95016-0.
- Steger, C. R. et al. (2017). Firn Meltwater Retention on the Greenland Ice Sheet: A Model Comparison. *Frontiers in Earth Science* 5.3, pp. 1–16. DOI:10.3389/FEART.2017.00003.
- Steiner, J. F., T. R. Gurung, S. P. Joshi, I. Koch, T. Saloranta, J. Shea, A. B. Shrestha, E. Stigter, and W. W. Immerzeel (2021). Multi-year observations of the high mountain water cycle in the Langtang catchment, Central Himalaya. *Hydrological Processes* 35.5, pp. 1–7. DOI:10.1002/HYP.14189.
- Stigter, E. E., N. Wanders, T. M. Saloranta, J. M. Shea, M. F. P. Bierkens, and W. W. Immerzeel (2017). Assimilation of snow cover and snow depth into a snow model to estimate snow water equivalent and

- snowmelt runoff in a Himalayan catchment. *The Cryosphere* 11.4, pp. 1647–1664. DOI:10.5194/TC-11-1647-2017.
- Stigter, E. E., M. Litt, J. F. Steiner, P. N. J. Bonekamp, J. M. Shea, M. F. P. Bierkens, and W. W. Immerzeel (2018). The importance of snow sublimation on a Himalayan glacier. *Frontiers in Earth Science* 6.108, pp. 1–16. DOI:10.3389/FEART.2018.00108.
- Stössel, F., M. Guala, C. Fierz, C. Manes, and M. Lehning (2010). Micrometeorological and morphological observations of surface hoar dynamics on a mountain snow cover. *Water Resources Research* 46.4, pp. 1–11. DOI:10.1029/2009WR008198.
- Strasser, U., M. Bernhardt, M. Weber, G. E. Liston, and W. Mauser (2008). Is snow sublimation important in the alpine water balance? *The Cryosphere* 2.1, pp. 53–66. DOI:10.5194/TC-2-53-2008.
- Sun, N., H. Yan, M. S. Wigmosta, L. R. Leung, R. Skaggs, and Z. Hou (2019). Regional Snow Parameters Estimation for Large-Domain Hydrological Applications in the Western United States. *Journal of Geophysical Research: Atmospheres* 124.10, pp. 5296–5313. DOI:10.1029/2018JD030140.
- Tahir, A. A., P. Chevallier, Y. Arnaud, and B. Ahmad (2011). Snow cover dynamics and hydrological regime of the Hunza River basin, Karakoram Range, Northern Pakistan. *Hydrology and Earth System Sciences* 15.7, pp. 2275–2290. DOI:10.5194/HESS-15-2275-2011.
- Tetens, V. (1930). Über einige meteorologische Begriffe. *Zeitschrift für Geophysik* 6, pp. 297–309.
- Van Dam, O. (2001). Forest filled with gaps: effects of gap size on water and nutrient cycling in tropical rain forest: a study in Guyana. PhD thesis. Utrecht University, pp. 8–15.
- Van Pelt, W. J. J., V. A. Pohjola, and C. H. Reijmer (2016). The Changing Impact of Snow Conditions and Refreezing on the Mass Balance of an Idealized Svalbard Glacier. *Frontiers in Earth Science* 4.102, pp. 1–15. DOI:10.3389/FEART.2016.00102.
- Van Den Broeke, M. R. (1997). Spatial and temporal variation of sublimation on Antarctica: Results of a high-resolution general circulation model. *Journal of Geophysical Research* 102.D25, pp. 29,765–29,777. DOI:10.1029/97JD01862.
- Van Pelt, W. J. J., J. Oerlemans, C. H. Reijmer, V. A. Pohjola, R. Pettersson, and J. H. Van Angelen (2012). Simulating melt, runoff and refreezing on Nordenskiöldbreen, Svalbard, using a coupled snow and energy balance model. *The Cryosphere* 6.3, pp. 641–659. DOI:10.5194/TC-6-641-2012.
- Veldhuijsen, S. B., R. J. De Kok, E. E. Stigter, J. F. Steiner, T. M. Saloranta, and W. W. Immerzeel (2022). Spatial and temporal patterns of snowmelt refreezing in a Himalayan catchment. *Journal of Glaciology* 68.268, pp. 369–389. DOI:10.1017/JOG.2021.101.
- Vickers, D. and L. Mahrt (1997). Quality Control and Flux Sampling Problems for Tower and Aircraft Data. *Journal of atmospheric and oceanic technology* 14.3, pp. 512–526. DOI:10.1175/1520-0426(1997)014<0512:QCAFSP>2.0.CO;2.
- Vionnet, V., E. Brun, S. Morin, A. Boone, S. Faroux, P. Le Moigne, E. Martin, and J. M. Willemet (2012). The detailed snowpack scheme Crocus and its implementation in SURFEX v7.2. *Geoscientific Model Development* 5.3, pp. 773–791. DOI:10.5194/GMD-5-773-2012.
- Vionnet, V., E. Martin, V. Masson, G. Guyomarc'h, F. Naaim-Bouvet, A. Prokop, Y. Durand, and C. Lac (2014). Simulation of wind-induced snow transport and sublimation in alpine terrain using a fully coupled snowpack/atmosphere model. *The Cryosphere* 8.2, pp. 395–415. DOI:10.5194/TC-8-395-2014.
- Vionnet, V., E. Martin, V. Masson, C. Lac, F. Naaim-Bouvet, and G. Guyomarc'h (2017). High-Resolution Large Eddy Simulation of Snow Accumulation in Alpine Terrain. *Journal of Geophysical Research: Atmospheres* 122.20, pp. 11,005–11,021. DOI:10.1002/2017JD026947.
- Wagnon, P. et al. (2013). Seasonal and annual mass balances of Mera and Pokalde glaciers (Nepal Himalaya) since 2007. *The Cryosphere* 7.6, pp. 1769–1786. DOI:10.5194/TC-7-1769-2013.
- Wagnon, P., J. E. Sicart, E. Berthier, and J.-P. Chazarin (2003). Wintertime high-altitude surface energy balance of a Bolivian glacier, Illimani, 6340 m above sea level. *Journal of Geophysical Research* 108.D6, p. 4177. DOI:10.1029/2002JD002088.
- Wanders, N., S. M. De Jong, A. Roo, M. F. P. Bierkens, and D. Karssenbergh (2013). The benefits of using remotely sensed soil moisture in parameter identification of large-scale hydrological models. *Water Resources Research* 50.8, pp. 6874–6891. DOI:10.1002/2013WR014639.
- Warscher, M., U. Strasser, G. Kraller, T. Marke, H. Franz, and H. Kunstmann (2013). Performance of complex snow cover descriptions in a distributed hydrological model system: A case study for the high Alpine terrain of the Berchtesgaden Alps. *Water Resources Research* 49.5, pp. 2619–2637. DOI:10.1002/WRCR.20219.
- Wayand, N. E., C. B. Marsh, J. M. Shea, and J. W. Pomeroy (2018). Globally scalable alpine snow metrics. *Remote Sensing of Environment* 213, pp. 61–72. DOI:10.1016/J.RSE.2018.05.012.

- Webb, E. (1970). Profile relationships: The log-linear range, and extension to strong stability. *Quarterly Journal of the Royal Meteorological Society* 96.407, pp. 67–90. DOI:10.1002/QJ.49709640708.
- Webb, E., G. Pearman, and R. Leuning (1980). Correction of flux measurements for density effects due to heat and water vapour transfer. *Quarterly Journal of the Royal Meteorological Society* 106.447, pp. 85–100. DOI:10.1002/QJ.49710644707.
- Wever, N, C Fierz, C Mitterer, H Hirashima, and M Lehning (2014). Solving Richards Equation for snow improves snowpack meltwater runoff estimations in detailed multi-layer snowpack model. *The Cryosphere* 8.1, pp. 257–274. DOI:10.5194/TC-8-257-2014.
- Wever, N., L. Schmid, A. Heilig, O. Eisen, C. Fierz, and M. Lehning (2015). Verification of the multi-layer SNOWPACK model with different water transport schemes. *The Cryosphere* 9.6, pp. 2271–2293. DOI:10.5194/TC-9-2271-2015.
- Wilczak, J, S Oncley, and S Stage (2001). Sonic Anemometer Tilt Correction Algorithms. *Boundary-Layer Meteorology* 99.1, pp. 127–150. DOI:10.1023/A:1018966204465.
- Wimmer, F., S. Schlaffer, T. aus der Beek, and L. Menzel (2009). Distributed modelling of climate change impacts on snow sublimation in Northern Mongolia. *Advances in Geosciences* 21, pp. 117–124. DOI:10.5194/ADGEO-21-117-2009.
- Wolff, M. A., K. Isaksen, A. Petersen-Øverleir, K. Ødemark, T. Reitan, and R. Brækkan (2015). Derivation of a new continuous adjustment function for correcting wind-induced loss of solid precipitation: results of a Norwegian field study. *Hydrology and Earth System Sciences* 19.2, pp. 951–967. DOI:10.5194/HESS-19-951-2015.
- Wulf, H., B. Bookhagen, and D. Scherler (2016). Differentiating between rain, snow, and glacier contributions to river discharge in the western Himalaya using remote-sensing data and distributed hydrological modeling. *Advances in Water Resources* 88, pp. 152–169. DOI:10.1016/J.ADVWATRES.2015.12.004.
- Xiong, C., J. Shi, Y. Cui, and B. Peng (2017). Snowmelt pattern over high-mountain Asia detected from active and passive microwave remote sensing. *IEEE Geoscience and Remote Sensing Letters* 14.7, pp. 1096–1100. DOI:10.1109/LGRS.2017.2698448.
- Zhou, J., J. W. Pomeroy, W. Zhang, G. Cheng, G. Wang, and C. Chen (2014). Simulating cold regions hydrological processes using a modular model in the west of China. *Journal of Hydrology* 509, pp. 13–24. DOI:10.1016/J.JHYDROL.2013.11.013.

Acknowledgements

Dear Walter, what a journey it has been. Thank you for guiding me through the steep learning curve of my PhD and fieldwork in Nepal. Whenever I was overwhelmed by it, you were there to help and support. You helped me building my confidence and made me aware what my strengths are. Thank you for stimulating and encouraging me to develop my own research ideas and for giving me the freedom to explore these ideas. Also, thank you for giving me the opportunity to choose and explore the type of snow measurements that I wanted to work with. Some of my ideas were successful, others were unfortunately less successful. However, you taught me that this is the way it goes in the field. I have experienced you as a caring, smart and to-the-point supervisor. Thank you so much for all your help and support, also on a personal level.

Dear Marc, the first memory that pops up in my mind, is of you joining the Langtang field trip in 2017. This field trip showed me your enthusiasm for science even more. It still makes me smile when those memories come back. I think you were quite unlucky being responsible for the crucial generator during that field trip. Three of them broke down and I remember all the pieces of it laying on a table in Kyangjin. You were still determined to fix it, while others would probably already have given up. But you managed with some help! Thank you for your guidance, enthusiasm and smart input and ideas regarding my research. The brainstorm sessions with you were always fruitful.

Furthermore, I am thankful to the Mountain Hydrology team for all the helpful discussions and many lunch walks together.

Also, I am grateful to all the porters that brought all equipment at the right locations in the field. Without you my research would not have been possible. Phonindra, I will always be very grateful for your help, especially at the two most critical moments during my fieldwork in Nepal. In the field you have always been kind to me, supportive and caring. Thank you so much.

My PhD buddies Jakob and Pleun; we started our PhD journeys together. I am grateful that we shared this. You both supported me so much and I learnt a lot from you. Pleun, I enjoyed our many tea breaks, occasional running, and good conversations. Thank you for your friendship. Jakob, thank you for all your care, in the office, in the field, as well as in private life. I have always enjoyed all the cynicism, sarcasm and seriousness in all conversations we had. I feel I am now closing our chapter that we started together, being the third to finish my PhD.

Muriel, you make me smile every time that we meet. It was nice to be the PhD representatives of the department together for two years and to become friends. I learnt a lot from you and I could always laugh with you. Thanks!

Inka, you made every stay in Kathmandu so much nicer. Thank you for welcoming me at your place whenever I was in Kathmandu. I loved all the time we spent together on your roof top. It is great having you as a friend.

Anna and Sergi, thank you for taking care of me when I was in Nepal. I felt so much warmth during my stay at your home. Anna, you always made me feel welcome at ICIMOD. I really appreciate that.

Niko, thank you for frequently inviting me for a tea break. It was great laughing together.

Thanks a lot for trying to boost my self-confidence and giving me some lectures about impostor syndrome. What do you think? Did it work?

Thank you Steven, Laura and Elisabeth for caring about how I was doing whenever I was in the department. I have definitely felt your warmth at those times.

Dear Marjolein, how could I ever thank you enough? You were there when I needed a friend most. Thank you for welcoming me together with Ivo in Casa Culemborg. There are no words that can express how thankful I am for your friendship and the support you have offered.

Martijn en Liesbeth, I believe I do not need a lot of words to express how grateful I am for us being friends. Thank you for being there for me. I feel blessed with our friendship.

Thank you Sandra for becoming such a good friend during the final stage of my PhD. I still love our early-morning pre-work-breakfasts with good coffee and good conversations. Thank you for laughing, complaining, being frustrated, being excited and being enthusiastic together. And of course I am grateful that you and Maarten were also there for Kiki and Beertje when needed (or not).

Sanita and Emil, even though we were sometimes spread out over three countries, I was still able to feel your support. I am so happy that we have met and I hope to visit you soon in either Nepal or Denmark to also reunite all birdies.

Dear Johannes, I am so happy that we have met in Svalbard when we both took the same PhD course. I enjoyed our time together so much, but please no frostbite next time, promised? Also, our daily contact after we both headed home, kept me motivated and more positive. Let's keep sharing our gardening stories, dinner ideas and weekend trips!

Other friends that I would like to thank here, as our contact supported me and helped me to stay positive: Alex, Astrid, Eva, Feiko, Joeri, Laura, Leon and Wim.

Many thanks to the very dedicated persons, who have offered me very personal help, in special, Martijn, Gwen, Shanta and the lovely team in Doorn. You have helped me to keep going and finish my thesis.

Dad and Mum, thank you for stimulating me to get most out of myself regarding my studies. I appreciate it so much that you have always supported me in my studies. Look what it brought me!

Dear Grandma, thank you for your everlasting curiosity and for offering me a spot on your couch so many times. Your (sometimes critical) questions about my research helped me to keep my story straight and simple.

And of course, my dear little fluffy guinea pigs; Kiki and Beertje. Thank you for sitting and chilling next to me and your distraction while I was writing the introduction and synthesis of my thesis. You have made me smile so many times because of your funny actions and fluffiness. You have made me aware what is most important in the world; to have fresh veggies in the fridge. Thank you for keeping me healthy.

List of Scientific Publications

Journal articles, as first author

- Stigter, E. E., Wanders, N., Saloranta, T. M., Shea, J. M., Bierkens, M. F. P., Immerzeel, W. W. (2017), Assimilation of snow cover and snow depth into a snow model to estimate snow water equivalent and snowmelt runoff in a Himalayan catchment, *The Cryosphere*, 11.4, 1647–1664, doi:10.5194/tc-11-1647-2017
- Stigter, E. E., Litt, M., Steiner, J. F., Bonekamp, P. N. J., Shea, J. M., Bierkens, M. F. P., Immerzeel, W. W. (2018), The importance of snow Sublimation on a Himalayan glacier, *Frontiers in Earth Science*, 6, doi:10.3389/feart.2018.00108
- Stigter, E. E., Steiner, J. F., Koch, I., Saloranta, T., Kirkham, J. D., Immerzeel, W. W. (2021), Energy and mass balance dynamics of the seasonal snowpack at two high-altitude sites in the Himalaya, *Cold Regions Science and Technology*, doi:10.1016/j.coldregions.2021.103233

Journal articles, as co-author

- Steiner, J. F., Litt, M., Stigter, E. E., Shea, J., Bierkens, M. F. P., Immerzeel, W. W. (2018), The importance of turbulent fluxes in the surface energy balance of a debris-covered glacier in the Himalayas, *Frontiers in Earth Science - Cryospheric Sciences*, 7, doi:10.3389/feart.2018.00144
- Kirkham, J. D., Koch, I., Saloranta, T. M., Litt, M., Stigter, E. E., Møen, K., Thapa, M., Melvold, K., Immerzeel, W. W. (2019), Near real-time measurement of snow water equivalent in the Nepal Himalayas, *Frontiers in Earth Science - Cryospheric Sciences*, 7, doi:10.3389/feart.2019.00177
- Litt, M., Shea, J. M., Wagnon, P., Steiner, J. F., Koch, I., Stigter, E. E., Immerzeel, W. W. (2019), Glacier ablation and temperature indexed melt models in the Nepalese Himalaya, *Scientific Reports*, 9.1, 411-427, doi:10.1038/s41598-019-41657-5
- Saloranta, T. M., Thapa, M., Kirkham, J. D., Koch, I., Melvold, K., Stigter, E. E., Litt, M., Møen, K. (2019), A model setup for mapping snow conditions in High-Mountain Himalaya, *Frontiers in Earth Science - Cryospheric Sciences*, 7, doi:10.3389/feart.2019.00129
- Valkonen, T., Stoll, P., Batrak, Y., Køltzow, M., Schneider, T. M., Stigter, E. E., Aashamar, O. B., Støylen, E., Jonassen, M. O. (2020), Evaluation of a sub-kilometre NWP system in an Arctic fjord-valley system in winter, *Tellus A: Dynamic Meteorology and Oceanography*, 72.1, 1–21, doi:10.1080/16000870.2020.1838181
- Kraaijenbrink, P. D. A., Stigter, E. E., Tandong, Y., Immerzeel, W. W. (2021), Climate change decisive for Asia's snow meltwater supply, *Nature Climate Change*, 11, 591–597, doi:10.1038/s41558-021-01074-x
- Steiner, J. F., Gurung, T. R., Sharad, J. P., Koch, I., Saloranta, T. M., Shea, J. M., Shrestha, A. B., Stigter, E. E., Immerzeel, W. W. (2021), Multi-year observations of the high mountain water cycle in the Langtang catchment, Central Himalaya, *Hydrological Processes*, 35.5, doi:10.1002/hyp.14189

Veldhuijsen, S. B. M., de Kok, R. J., Stigter, E. E., Steiner, J. F., Saloranta, T. M., Immerzeel, W. W. (2021), Spatial and temporal patterns of snowmelt refreezing in a Himalayan catchment, *Journal of Glaciology*, 1–21, doi: 10.1017/jog.2021.101

Teaching and supervision

Teaching assistance

- Terrestrial systems and their spatial patterns (GEO2-4204)
- Earth observation and data analysis (GEO2-4208)
- Physical hydrology (GEO2-4203)
- Remote sensing (GEO4-4408)
- Hydrology, climate change and the cryosphere (GEO4-4423)

Guest lecture

- Guest lecture on snow hydrology in the MSc course Hydrology, climate change and the cryosphere

Student supervision

- Coen Sprong (BSc thesis, 2017) Snow cover analysis in the Langtang catchment using Sentinel-2 and Landsat-8 imagery
- Lukas Rolf (Tailor made MSc course, 2017) PCRaster-based modelling of snow pack development on the Himalayan Yala Glacier
- Jip Zinsmeister (MSc thesis, 2018) Understanding drivers of snow cover patterns in the central Himalayas using high resolution remote sensing imagery
- Sanne Veldhuijsen (MSc thesis, 2020) The importance, patterns and effects of snowmelt re-freezing in a Himalayan catchment
- Luuk van der Valk (MSc research internship, 2020) Determination of precipitation phase in Langtang valley, Nepal

About the author

Emmy Stigter has been passionate about snow, cold regions, mountains and climate (change) since she was a teenager. With geography being one of her favourite courses in high school, she chose to study earth sciences at Utrecht University. She wrote a bachelor's thesis on determining the snow water equivalent with remote sensing techniques. The combination of solid and liquid water still fascinated her after doing her bachelor. Therefore, she decided to continue a master in hydrology at Utrecht University and specialise in cryosphere by taking courses at both the Institute for Marine and Atmospheric research Utrecht (IMAU) and the University Centre in Svalbard (UNIS). She spent the summer 2015 in Svalbard after the first year of her master. She studied Arctic glaciers and melt season dynamics at UNIS. As she enjoyed this very much, she returned five more times to Svalbard for several courses at UNIS in boundary layer meteorology, remote sensing of the cryosphere, glaciology, and snow and avalanche dynamics during both her master and PhD. She wrote a master's thesis with a focus on snow and mountains, and assimilated snow observations into a snow model to estimate the snow water equivalent in the Langtang catchment in Nepal. Hereafter, she started as a PhD student in the Mountain hydrology group at the department of physical geography at Utrecht University, focussing on snow dynamics in the Himalaya. During her PhD she performed fieldwork on a regular basis at high altitude in Nepal. She got skilled in independently setting up and maintaining automatic weather stations, an eddy covariance system, snow stations, performing snow pit and ablation stake measurements and flying unmanned aerial vehicles. She enjoys working with a combination of field data, remote sensing and modelling to better understand the environment.